Measurement of the Inclusive and Differential Cross-Sections for Semileptonic $t\bar{t}b\bar{b}$ Production with the CMS Detector at CERN and Studies of the Readout Chip for the Phase 2 Upgrade of the CMS Pixel Detector

---

Dissertation

zur

Erlangung der naturwissenschaftlichen Doktorwürde
(Dr. sc. nat.)

vorgelegt der

Mathematisch-naturwissenschaftlichen Fakultät

der

Universität Zürich

von

Umberto Molinatti

aus

Italien

Promotionskommission

Prof. Dr. Florencia Canelli (Vorsitz)

Prof. Dr. Cristina Botta

Prof. Dr. Stefano Pozzorini

Zürich, 2023

Acknowledgments

I want to express my gratitude to the following people for their support and contributions to this work:

First, I want to thank my advisor, Prof. Florencia Canelli, for her guidance, encouragement, and support throughout my research.

I also want to thank the previous and current members of my committee, Prof. Cristina Botta, Prof. Aurelio Juste, and Prof. Stefano Pozzorini, for their valuable feedback and suggestions. Their insights and critiques helped refine my work and improve my research.

My sincerest thanks to the people whose patience and dedication drove me in my work and education. Specifically, I would like to acknowledge Sebastien Wertz, who took on the challenge of supervising a novice student and helped introduce topics that were once foreign to me. I also deeply appreciate the unwavering support of Kyle Cormier, whose contribution to this work cannot be emphasized enough, and who demonstrated exceptional knowledge and patience in guiding me through the latter part of my doctorate. Stella Orfanelli was a constant source of encouragement and assistance in a field I came to be intrigued and fascinated by. Finally, I extend my thanks to Anna Macchiolo for her kind help with this thesis, as well as for supporting me in the search for new horizons.

To the members of the CERN UZH group whose company and support were invaluable during this journey, making every day pleasant and every challenge surmountable both at work and outside it. Jaana Heikkilae, Peter Meiring, and Sergio Sanchez Cruz.

To all the PhD students that have come and gone during these past four years, making office life enjoyable no matter the place. Pascal Baertschi, Tiziano Bevilacqua, Daniel Brzhechko, Marc Huwiler, Weijie Jin, Arash Jofrehei, Sascha Liechti, Vinicius Mikuni, Lars Noehte, Izaak Neutelings, Korbinian Schweiger, and Fabian Stager.

Finally, I want to thank my family and friends for their unwavering support and encouragement. Their love and support kept me going through the ups and downs of the research process.

Thank you all for your contributions to this work.

Contents

List of Figures

List of Tables

1 Introduction

The study of particle physics has allowed humanity to probe the building blocks that matter is made of. The "indivisible" atoms of the late 19th century gave way to smaller particles, some of which were themselves found to be composite. This study allowed for the discovery of quantum physics, where these new particles were shown to behave in a manner greatly unlike that of macroscopic matter. The efforts to study these processes further were undertaken with a combination of theoretical and experimental work involving the tandem development of new theories to explain and predict phenomena on the one hand with accelerators and detectors to reach ever higher energies for study on the other.

The discovery of the Higgs boson in 2012 [1, 2] marked a key moment in particle physics research with the completion of all components of the Standard Model (SM) of particle physics. This theoretical framework has been guiding experimental research since its formulation in the 1970s with huge success.

However, this is not to say that all the work is done. Several observations both in and out of particle physics fall outside of what the SM would expect and, in so doing, suggest the existence of some further physics beyond the SM. The search for this new physics is currently the driving force of particle physics research where it is either pursued directly by searching for new particles or behaviors or indirectly by scrutinizing the SM to find discrepancies that might hint towards something beyond.

This thesis takes the latter approach and presents the measurement of the differential cross-section of the top-antitop quark production in association with b-quarks ($t\bar{t}b\bar{b}$) process at the CMS experiment [3] at the Large Hadron Collider (LHC) [4]. This research aims to study $t\bar{t}b\bar{b}$ and provide a more precise measurement before comparing it to the theoretical calculations. The main objective of this research is to examine $t\bar{t}b\bar{b}$ by measuring its inclusive and differential cross-sections and to provide more information and to provide more information that can aid the theoretical calculations. The data used in this study was collected by the CMS experiment at the LHC between 2016 and 2018.

In the next years, the CMS detector will be upgraded to cope with higher data rates and challenging radiation levels of the High Luminosity LHC. A second part of this thesis studies many necessary aspects of the readout chip that will be used in the CMS pixel tracker.

I contributed to the data analysis part of this work by developing code to identify the $t\bar{t}b\bar{b}$ process such as event selection, binning studies, analysis of selection performance, and studies of the observable fittingfor cross-section estimation. My hardware work instead consisted in the running of tabletop experiments for the serial powering, writing routines to test the readout chips, and using those routines for radiation testing of the chips.

The thesis is organized as follows:

Chapter 2 describes the experimental setup of the Large Hadron Collider and the CMS detector whose data were used for the analysis.

Chapter 3 presents an overview of the Standard Model of particle physics and the components most relevant to the $t\bar{t}b\bar{b}$ process.

Chapter 4 is an introduction to $t\bar{t}b\bar{b}$ including the motivation for research, previous investigations and the overall analysis strategy.

Chapters 5-9 detail the analysis process with a look at the objects and spaces used, unfolding and signal extraction, and the systematic uncertainties considered.

Chapter 10 is an overview of the main results of the analysis.

Chapter 11 summarizes the results and methods of the analysis.

Chapter 12 describes the recent upgrades developed for the CMS inner tracker.

Chapters 13&14 present a series of studies conducted in the course of studying and testing the new inner tracker pixel chips.

Chapter 15 presents the final summary of the thesis.

2 Experimental Setup

2.1 The Large Hadron Collider

The Large Hadron Collider (LHC) [4] is a circular proton-proton collider located around Geneva (Switzerland). The experiment is part of CERN and began operation in 2009. It started with an initial center-of-mass energy of 7 TeV which was then increased to 8 TeV in 2012 and later to 13 TeV in 2015. The center-of-mass energy of the accelerator is sum of the energies of the involved particles which is then available for the production of new particles after collision.

It was designed to investigate the properties of the Standard Model (SM) of Particle Physics, in particular the Higgs boson, and to investigate the physics Beyond the Standard Model (BSM) by studying discrepancies in the SM or via direct searches of particles.

The LHC accelerates bunches of protons and heavy ions where a bunch is a collection of particles (10^{11} protons or $7 \cdot 10^7$ Pb ions) with a 25 ns interval between them. These are accelerated by making use of previous CERN accelerators as boosters to accelerate the protons to speeds close to the speed of light resulting in a final center-of-mass energy of 13.6 TeV for p-p collisions and 2.76 TeV for *Pb*-*Pb* collisions. It is a circular collider where the protons are kept rotating in the ring through the use of superconducting niobium-titanium dipole magnets kept at a temperature of 2 K with liquid helium. The protons produced by hydrogen ionization are first accelerated to 50 MeV by the LINAC2 [5] accelerator (or LINAC4 [6] after 2020). After this initial push, they are further accelerated by a series of three synchrotrons (BOOSTER [7], Proton Synchrotron [8], and Super Proton Synchrotron [9]) which bring the proton energy to 450 GeV, at which point they are injected into LHC proper to reach their final 13.6 TeV. A diagram of the accelerator system is shown in Figure 1 One of the main advantages of LHC being a proton-proton collider rather than electron-positron like its predecessor LEP [10] is that it suffers much less from the effects of synchrotron radiation. This is an effect whereby the accelerated particles lose energy in a manner inversely proportional to the fourth power of the particle mass which results in proton-proton collisions being more energy efficient for a 13.6 TeV regime.

In different areas of the 27 km ring of the LHC there are a number of experiments present with their own areas of operation. ATLAS [12] and CMS [13] are two high luminosity experiments aiming for a peak luminosity of $L = 10^{34}$ cm^{2}s for proton collisions. There are also two low luminosity proton experiments LHCb [14] focusing on B-physics with a target luminosity of $L = 10^{32}$ cm^{2}s and TOTEM [15] focusing on proton scattering at small angles with a target luminosity of $L = 2 \cdot 10^{29}$ cm^{2}s. Finally ALICE [16] focuses on ion-ion collisions and has a target luminosity of $L = 10^{27}$ cm^{2}s for *Pb*-*Pb* collisions.

2.1.1 Luminosity and Cross-Section

In particle physics, luminosity is a measure of the number of particles that can be passed through a certain space in a given time, this gives an idea of the number of collisions happening within the accelerator.

The instantaneous luminosity obtained by this collider can be calculated from the following equation:

$$L = \frac{N_b^2 n_b f_{rev} \gamma_r}{4\pi \epsilon_n \beta^*} F \tag{1}$$

Where N_b is the number of particles in each bunch, n_b is the number of bunches in each beam, f_{rev} the revolution frequency, γ_r the relativistic gamma factor, ϵ_n the normalized transverse beam emittance, β^* the beta function at the collision point, and F the geometric luminosity reduction factor due to the crossing angle at the interaction point (IP). This last factor is defined as:

$$F = \left(1 + \left(\frac{\theta_c \sigma_z}{2\sigma^*}\right)^2\right)^{-1/2} \tag{2}$$

With θ_c being the crossing angle at the IP, σ_z the root-mean-squared (RMS) bunch length, and σ^* the transverse RMS beam size at the IP.

This information then allows us to calculate the expected number of events per second for a process with a defined cross section $N_{event} = L\sigma_{event}$. Within the context of the experiment, it is also possible to

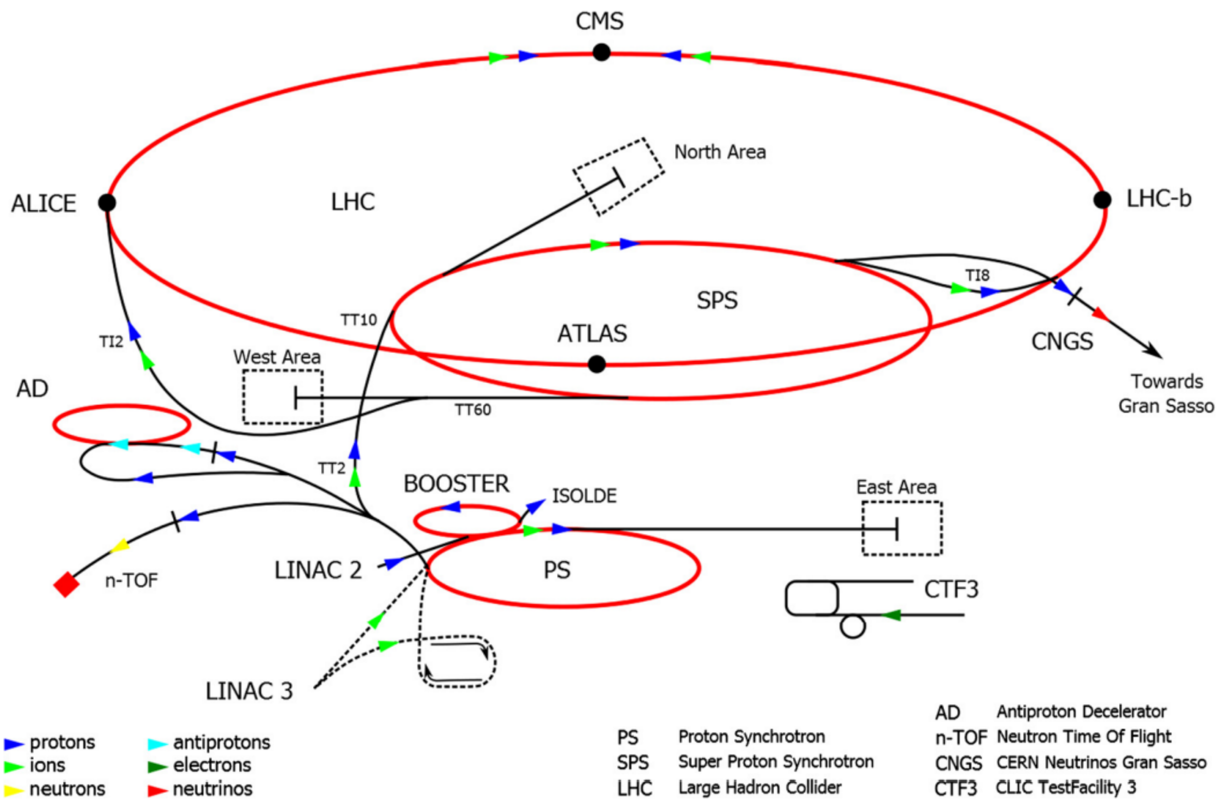

Figure 1: The CERN accelerator complex including the LHC and its injectors. Figure originally from [11].

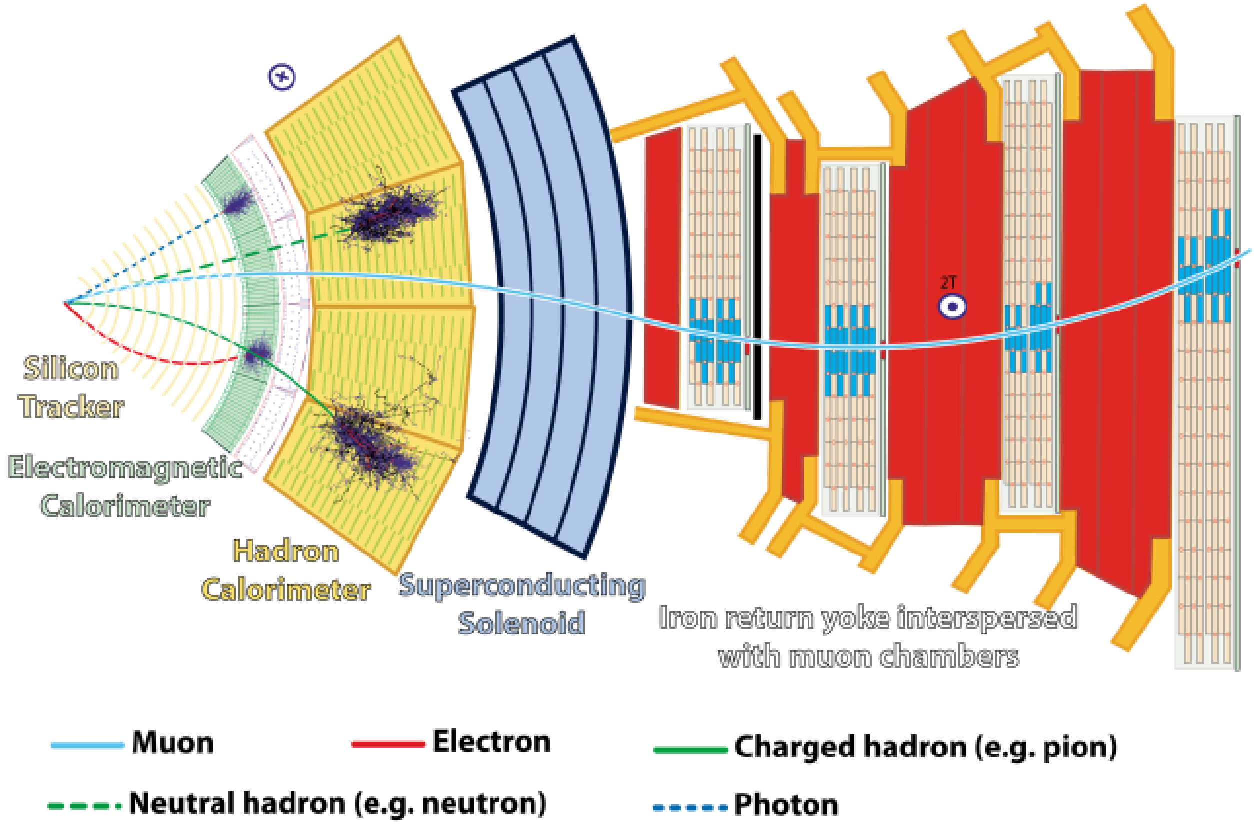

Figure 2: A slice of the CMS detector with an illustration of the behavior of different particles. Figure originally from [17]

obtain a differential cross section where the behavior of the studied process is investigated in more detail. By examining particular observables (e.g. momentum, energy, angle of emission) a comparison with the expected theoretical calculations allows for a better understanding of the process in question and can hint towards new research.

2.2 The CMS Detector

The Compact Muon Solenoid (CMS) [13][3] detector is one of the two high-luminosity detectors of LHC and it was designed with a focus on optimizing the muon detection system in proton-proton collisions.

To combine muon optimization with the space constraints, the design was based around a superconducting solenoid 14 m in length and 3 m in radius that is able to provide a magnetic field of 4 T which allows for good momentum resolution for muons.

The detector itself is structured as a series of different layers with a focus on different particles and particle properties. The innermost layer is a tracker system that measures the trajectory of charged particles just past the interaction point, this is followed by an electromagnetic (ECAL) and a hadronic (HCAL) calorimeter that capture and measure the energy of certain particles, and the outermost layer is the muon system that identifies and measures the momentum of muons. The structure of CMS can be seen in Figure 2.

The CMS detector works in tandem with ATLAS to provide two different methods of investigating the same phenomena and ensure a higher overall sensitivity. These are the collaborations that allowed for the discovery of the Higgs boson in 2012 [1, 2].

The detector has been upgraded since its installation to account for the increase in luminosity of LHC and is scheduled for a major upgrade in view of the High Luminosity LHC (HL-LHC) [18] which will reach an integrated luminosity of 3000 fb^{-1}.

To provide an improved trigger together with more up-to-date trackers and calorimeters that should

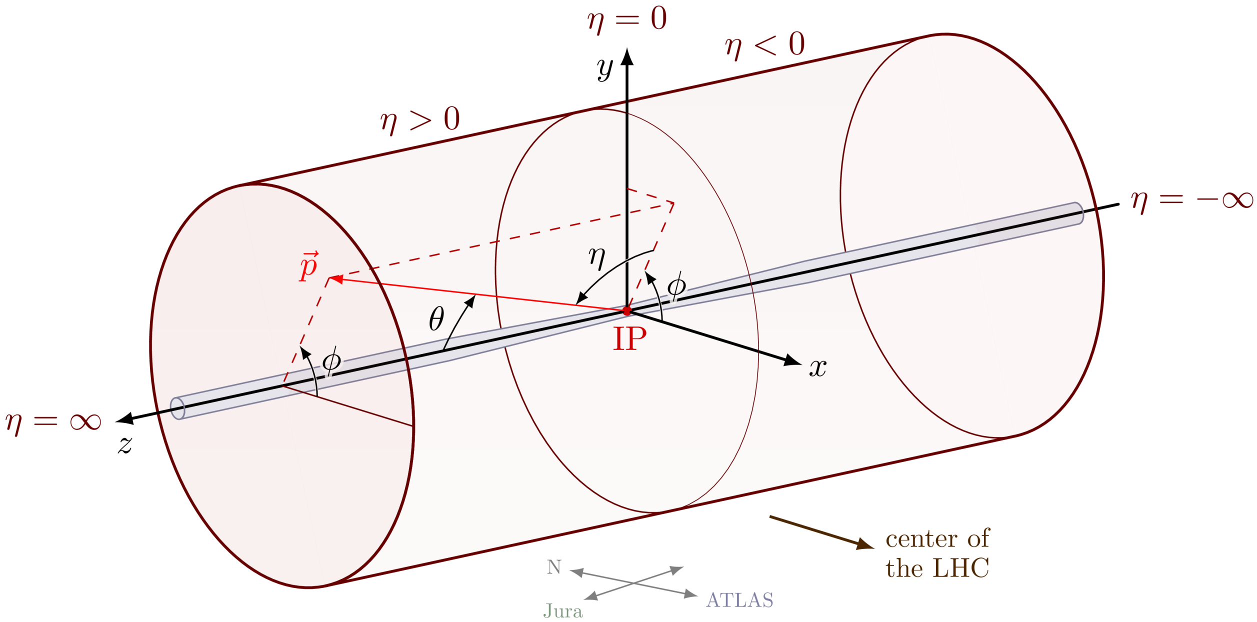

Figure 3: Schematic of the coordinate system of the CMS detector. Figure originally from [19]

be able to handle the much greater data rate and simultaneous proton-proton collisions (pile-up) while withstanding the increased radiation levels.

2.2.1 Coordinate System

It is important at this point to define the coordinate system used in CMS. Its origin is centered in the nominal collision point inside the detector, the y-axis is pointing vertically upward, and the x-axis is pointing radially inward toward the center of the LHC ring. The azimuthal angle ϕ is measured from the x-axis in the x-y plane, the radial coordinate in this plane is denoted by r, and the polar angle θ is measured from the z axis. However, θ is not often used because it is not Lorentz invariant for boosts along the direction of the beam. To this end, the pseudorapidity is defined as $\eta = -\ln(tan(\frac{\theta}{2}))$ and has the desired Lorentz invariance in the case of massless particles, which is a suitable approximation with the LHC energies. From this, it is possible to define the momentum transverse to the beam direction, indicated as p_T. A diagram with this information can be seen in Figure 3.

2.2.2 Tracker

The central tracking system [20, 21] is the closest part of the detector to the interaction point and aims to measure the trajectory of charged particles through this first region. It was designed with the goal of reconstructing high p_T tracks with an efficiency above 95% for isolated tracks while ensuring an efficiency of at least 90% in the $|\eta| < 2.6$ range for tracks contained within jets.

To ensure the necessary level of accuracy, the tracking system is divided into two sections (inner and outer tracker) consisting of respectively silicon pixel detectors and silicon strip detectors.

The inner tracker silicon pixel detectors are placed closest to the beamline and are arrayed in a series of layers varying in quantity between barrel and endcap. These detectors provide precise track points close to the interaction point and allow for good discrimination between tracks in a space with a very high track density while ensuring high precision for secondary vertex identification. This capability is also an important factor in the proper flavor tagging of the produced jets.

Before 2016, these pixel detectors were arranged in three barrel layers and two endcap layers. However, an upgrade at the end of the 2016 data taking period restructured this area of the detector to improve tracking resolution and efficiency, this is displayed in Figure 4.

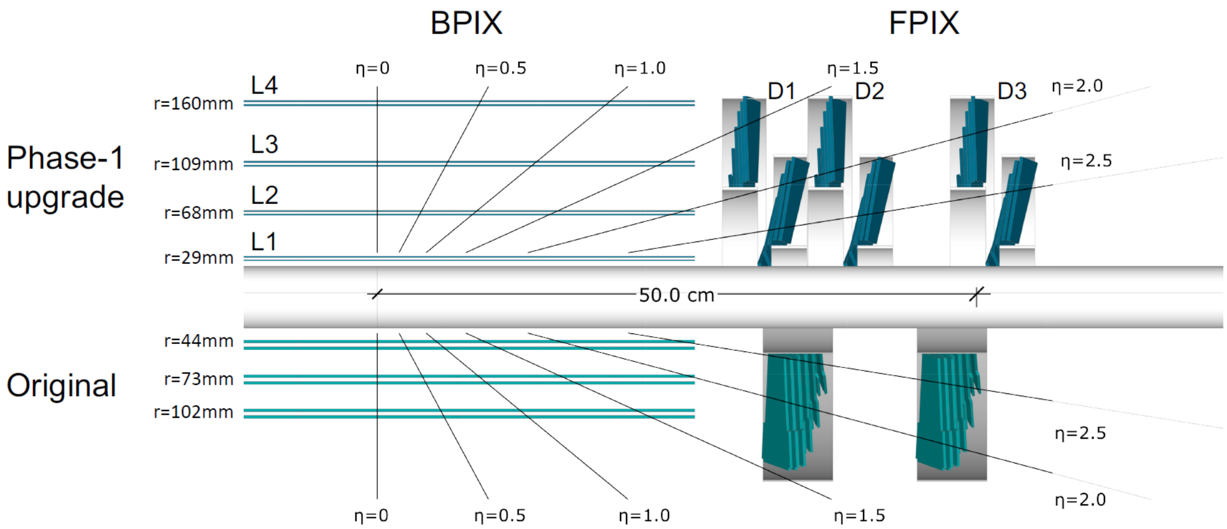

Figure 4: Layout of the inner tracker with a comparison between the original configuration and the configuration present since 2016. Figure originally from [17]

Beyond this first layer there is the outer tracker array of microstrip detectors shown in Figure 5. These detectors provide a good combination between bunch identification and spatial resolution while also being sufficiently radiation hard. They have a coarser pitch compared to the silicon pixels which is enough to provide accurate hit detection in this outer region that displays a reduced particle occupancy. They also have the advantage of being cheaper than the pixels and requiring fewer readout channels which in turn reduce the cabling and power requirements.

These detectors have two distinct layout regions. The barrel silicon detector covers the central region up to $|\eta| \leq 1.8$ while the endcap detector has coverage between $1.8 \leq |\eta| \leq 2.5$ and displays a different orientation to facilitate tracking.

All these properties allow for the tracker to obtain a series of hits in its various layers which can be combined into tracks of the charged particles that passed through such as muons, electrons, and hadrons. Given that the magnetic field curves the tracks of these particles, it is also possible to determine the momentum of each of these particles by studying the curvature of the track obtained.

2.2.3 Calorimeters

Beyond the tracking system there are the electromagnetic calorimeter (ECAL) and the hadronic calorimeter (HCAL). These detectors serve to capture the energy of the charged particles that emerge from the trackers. While the ECAL measures the energy of electrons, positrons, and photons. Charged hadrons instead deposit a small proportion of their energy in the ECAL while the majority is deposited in the HCAL.

The ECAL is composed of lead tungstate ($PbWO_4$) crystals which were determined to be especially suited for the CMS design. Their short radiation length allows for a compact ECAL which is combined with both radiation hardness and the relative ease with which they can be produced. Their main drawback was a low light yield but it has been addressed by the development of dedicated photodiodes.

The ECAL as shown in Figure 6 is divided in two sections, barrel and endcap, which cover respectively the intervals $|\eta| \leq 1.56$ and $1.65 \leq |\eta| \leq 2.61$ where the endcap has a reduced granularity compared to the barrel. To account for the reduced endcap granularity, preshower detectors are installed before the lead tungstate crystals. With their finer granularity, these further detectors provide enough information to distinguish between certain classes of events that would otherwise be misattributed, such as neutral pion decays which mimic high energy photons.

The HCAL is found outside of the ECAL and sketched in Figure 7. The two calorimeters are used to determine the energies and directions of particle jets and provide hermetic coverage of the outgoing particles

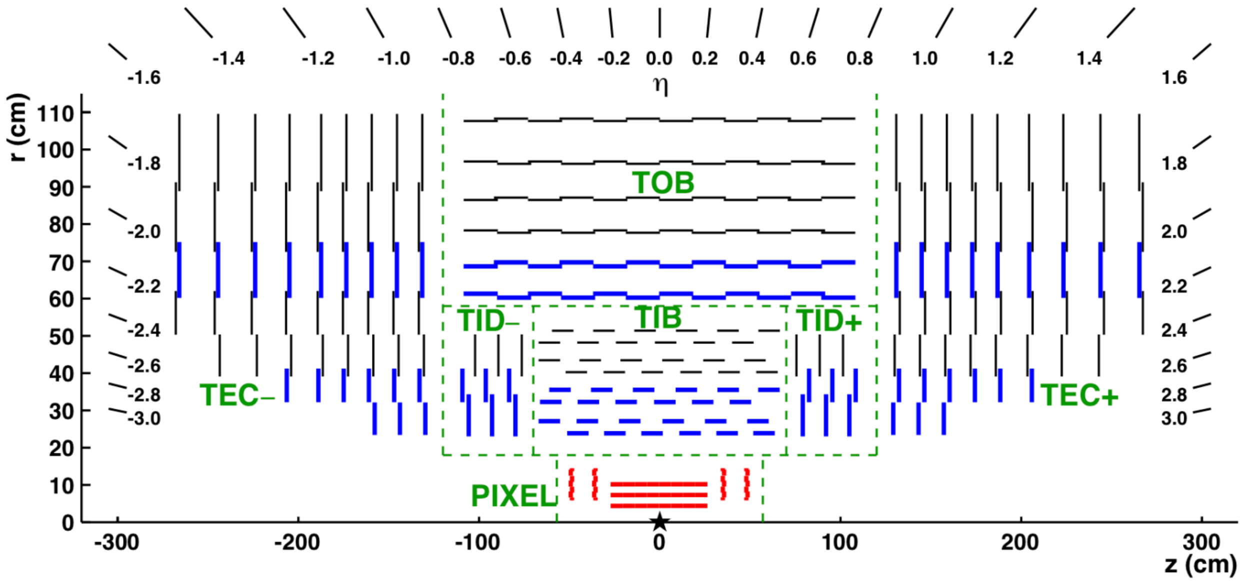

Figure 5: Schematic view of the CMS outer tracker. Figure modified from [22]

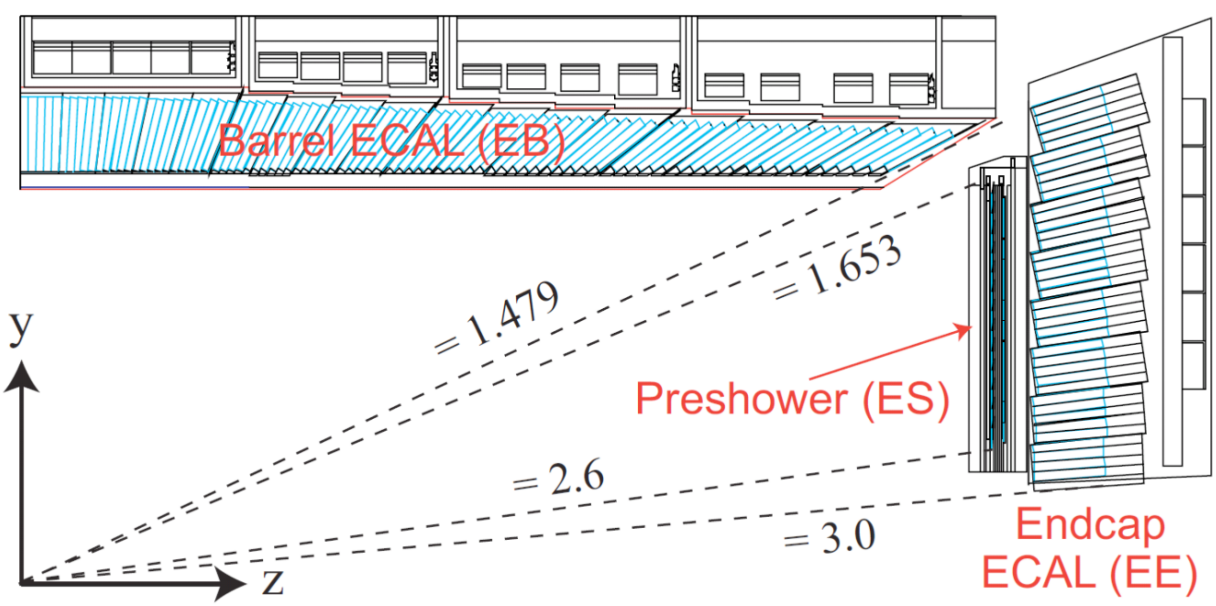

Figure 6: Arrangement of modules for the CMS ECAL. Figure modified from [23]

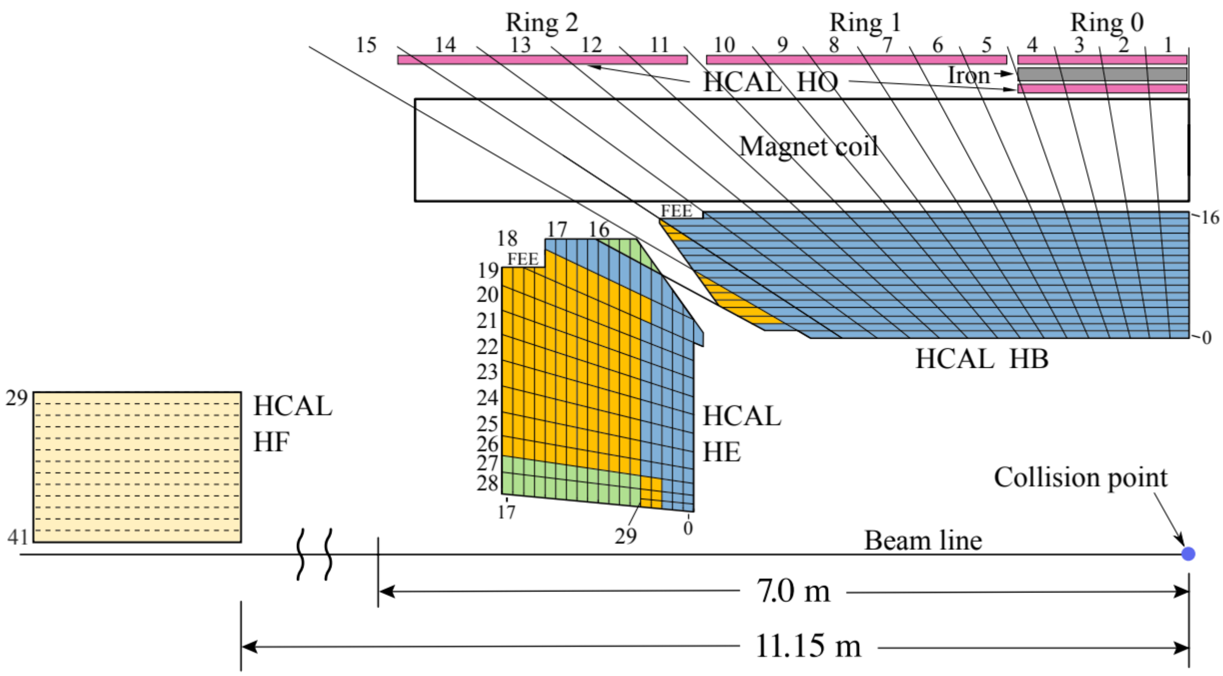

Figure 7: Arrangement of the CMS HCAL showing the positions of its four primary components: the hadron barrel (HB), the hadron endcap (HE), the hadron outer (HO), and the hadron forward (HF) calorimeters. Figure from [24]

to measure the missing transverse energy.

The HCAL is constructed with an alternation of detector layers with a passive absorber for which copper was chosen as a material because of its short interaction length that allows for a more compact machine. The active detector layers are divided into segments that provide a good granularity matching that of the ECAL and muon system.

To ensure the best efficiency in different pseudorapidity ranges, the barrel and endcap HCAL cover the range up to $|\eta| \leq 3$ while the $3 \leq |\eta| \leq 5$ range is covered by a dedicated very forward calorimeter.

The very forward calorimeter is distinguished from the other HCAL sections because it is built with steel and quartz fibers leading to shorter hadronic showers for better absorption of the very forward hadron showers.

The ECAL so constructed is able to fully stop the electrons and photons emerging from the tracker and thus measure their energy in full. The ECAL also manages to absorb a fraction of the energy of the hadrons but the HCAL's design allows it to fully stop the hadrons and measure any remaining energy they have. For the electrons, this information can also be combined with the trajectory and momentum information of the tracker to obtain a fuller picture of the hadron behavior.

2.2.4 Magnet and Muon System

Muon identification was chosen as a focus for CMS because muons produced from proton-proton collisions provide clear lepton signatures for a wide range of physics processes and helps with their identification, especially at high luminosities.

Starting from the outermost section of the detector, we find the four muon chambers interspersed with sections of the saturated iron yoke of the magnet system [25]. This is shown in Figure 8. The CMS magnet is a superconducting solenoid which produces a uniform magnetic field of 4 T. The use of a single magnet greatly simplifies the detector design and allows the magnet to be used as a structural basis for the rest of the detector. This allows for an independent momentum measurement while the multiple muon detectors provide greater reliability.

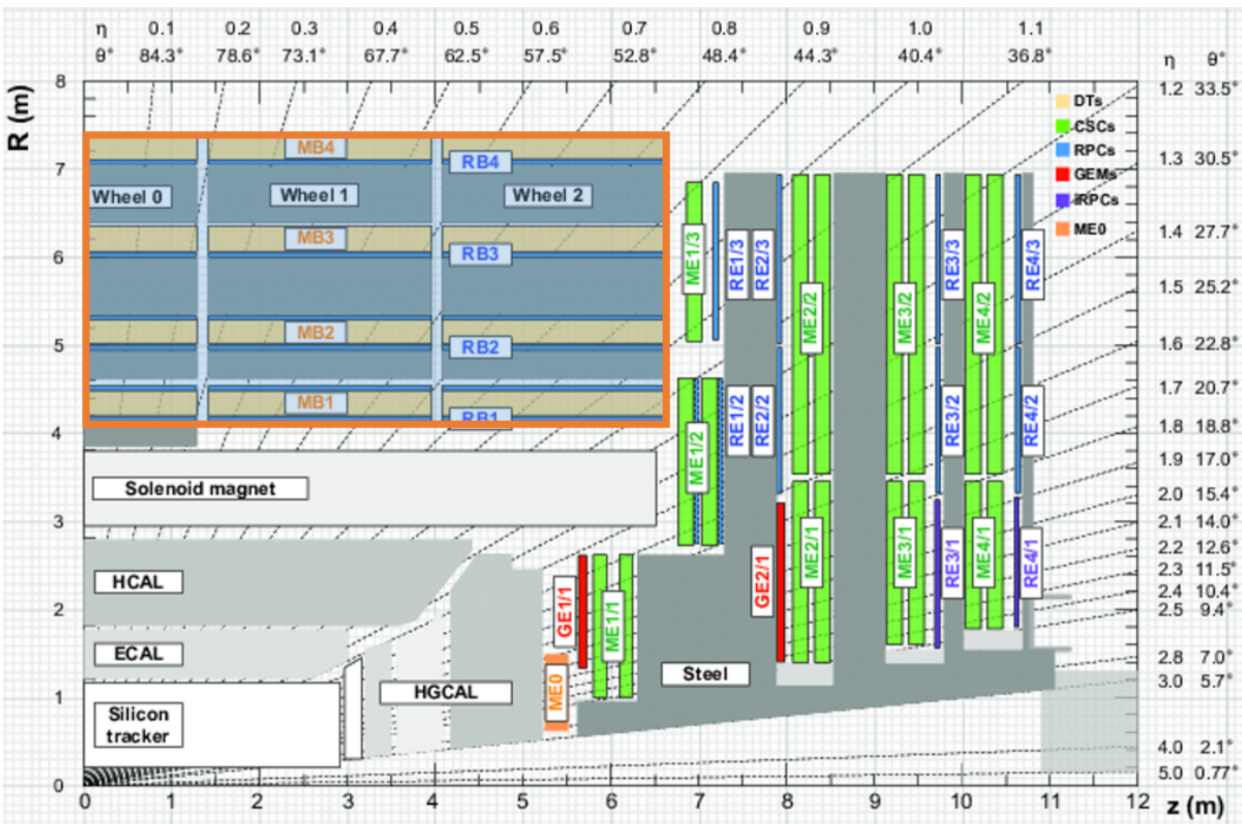

Figure 8: Cross section of the CMS muon system displaying the layout of the muon detectors interleaved with the iron yoke. Figure from [26]

To identify these muons as accurately as possible, the muon detectors were designed to have a high pseudorapidity coverage (up to $\eta = 2.4$), accurate transverse momentum resolution with a combination of material considerations, and a precise muon trigger with specific p_T thresholds.

Within the barrel of the CMS detector, the muon drift tubes are arranged in four concentric layers interleaved with five layers of the iron magnet yoke and five layers of Resistive Plate Chambers (RPC), this covers the detector acceptance up to $\eta = 2.1$. On the other hand, the endcap region reaches the full $\eta = 2.4$ coverage with three RPC layers and several layers of Cathode Strip Chambers, chosen in this region for their ability to resist high non-uniform magnetic fields.

Muons do not deposit much energy in matter, they pass through both calorimeters with most of their momentum. The muon chambers then provide further information on the trajectory of the muons which are the only particles with a clear signal in this section. These trajectories, combined with those of the trackers, allow for better identification of the muons as particles and provide further data on the muons' momentum.

3 The Standard Model

3.1 Overview

The Standard Model (SM) of particle physics [27, 28, 29, 30] is the current theoretical framework which describes the behavior of elementary particles and their interactions by means of the strong, weak, and electromagnetic forces.

The SM has been enormously successful since its inception at both at explaining the behavior of known particles and at predicting the existence of particles unknown at the time. Using SM predictions, it was possible to conduct targeted searches for new particles, leading to their discovery and experimental determination of their precise properties. The full set of SM particles is displayed in Figure 9.

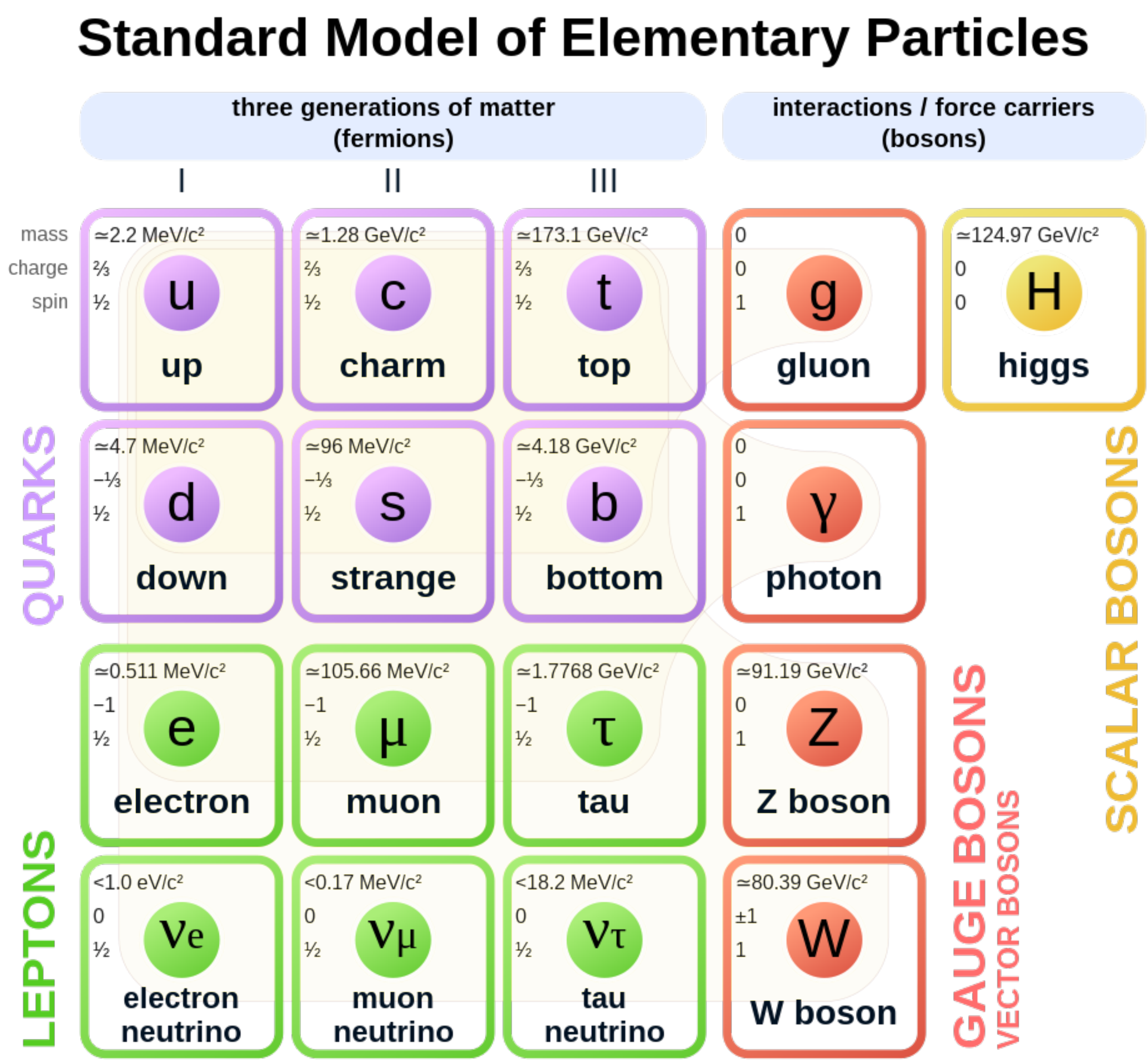

Figure 9: Diagram displaying the particles in the SM and their subdivisions

The discovery of the Higgs boson in 2012 provided the last piece of the SM. As the last predicted particle of the model, its measurement was a further confirmation of the validity of the model. At the same time the

Higgs boson's special connection to other SM particles and role in mass determination opened new avenues with which to study the SM

However, despite these successes, the SM is still not a complete explanation of our universe. This is in part because it cannot describe the existence of dark matter, the matter-antimatter asymmetry, or the gravitational behavior of fundamental particles. Furthermore, there are some discrepancies between what the SM predicts and observation of SM processes. This is the case, for example, for the mass of neutrinos which do not fit in the SM but have been extensively measured.

Because of this, it is important to continue experimental studies of SM processes in order to provide valuable information for the development of new theories Beyond the Standard Model (BSM). These studies can take the form of direct searches for new particles based on new BSM theories such as supersymmetry. Alternatively, one can conduct indirect searches which rely on measuring discrepancies between SM prediction and observation and later use them to search for BSM physics in a model agnostic manner.

3.2 Quantum Electrodynamics

Quantum Electrodynamics (QED) [31] is the theory that describes interactions mediated by the electromagnetic force and it can be described through the Lagrangian:

$$\mathcal{L}_{QCD} = \bar{q}(x)[i\gamma^{\mu}D_{\mu} - m]q(x) - \frac{1}{4}F^{a}_{\mu\nu}F^{a\mu\nu} \tag{3}$$

where $q(x)$ and $\bar{q}(x)$ describe the particle and antiparticle spin-1/2 Dirac fields for particles of mass m where $\bar{q} = q^{\dagger}\gamma^{0}$. The last term is the electromagnetic field tensor $F_{\mu\nu} = \partial_{\mu}A_{\nu} - \partial_{\nu}A_{\mu}$ where $A_{\mu/\nu}$ is the electromagnetic four-potential.

This force acts on any particle with an electric charge and is mediated by photons which, as charge-neutral particles, do not experience self interaction.

It is interesting to note that in QED, any charged particle will thus be surrounded by a cloud of photons which constantly create and annihilate electron-positron pairs. It then follows that the produced electrons and positrons will arrange themselves in such a way as to shield the charge of the central particle in a process called vacuum polarization.

This means that the effective charge of the central particle will decrease with distance (and correspondingly increase with energy). If we consider an electron, its charge will be screened according to the function:

$$\beta = \frac{\partial \log(\alpha(\mu))}{\partial \log(\mu^2)} = \frac{\partial \log(e(\mu))}{\partial \log(\mu)} \tag{4}$$

where μ is the scale at which the system is being studied, $\alpha = \frac{e^2}{4\pi\epsilon_0\hbar c}$ is the fine structure constant, and e the charge of the electron.

As such, the QED screening leads to a running coupling of α dependant on the energy scale Q being considered:

$$\alpha(Q^2) = \alpha(0)\left[1 + \frac{\alpha(0)}{3\pi}f\left(\frac{Q^2}{m_e^2}\right) + O(\alpha^2)\right] \tag{5}$$

3.3 Electroweak Interactions

Through the work of Glashow, Weinberg, and Salam [27, 29, 32] between 1960 and 1970 it was possible to derive the theory of electroweak interactions which combines QED with the effects of the weak interaction.

The weak interaction acts upon all fermions and is the only microscopic force that can interact with neutrinos.

The force carriers for the electroweak interactions are the photon for the electromagnetic interactions while the $W^{\pm}$ and Z bosons mediate the weak interaction.

The weak interaction is notable for a number of reasons.

Firstly it is the only force which is mediated by massive particles. This has the consequence that, despite the weak coupling constant being larger than the electromagnetic one ($\alpha_{em} \approx \frac{1}{137} < \alpha_W \approx \frac{1}{30}$), the weak interaction will have a similar strength to the electromagnetic force at high energies due to the suppression in weak decay rates derived from the boson masses.

Another peculiarity of the weak interaction is that it is the only case in which quark or lepton flavor can be altered from one to the other, for example in the $t \rightarrow b + W^+$ process.

Finally, this interaction is the only one known to violate CP symmetry. That is to say, if the particles involved are mirrored and switched with their antiparticles, the physical process in question does not necessarily remain equal as is the case for other interactions.

This can be observed through the lens of weak isospin (T_3) which is a quantum number that determines the weak interactions that are allowed to occur. All left-handed fermions have $T3 = \pm\frac{1}{2}$ while all right handed fermions have $T_3 = 0$. This quantity determines the possible weak interactions because T_3 must be conserved under these processes and quarks are not allowed to decay into a quark with the same weak isospin.

3.4 Quantum Chromodynamics

Quantum Chromodynamics (QCD) [33, 34] is the theory that describes interactions mediated by the strong force and it can be described through the Lagrangian:

$$\mathcal{L}_{QCD} = \sum_{flavors} \bar{q}_i^f(x)[i\gamma^\mu D_\mu - m_f]_{ij} q_j^f(x) - \frac{1}{4} G^a_{\mu\nu} G^{a\mu\nu} \tag{6}$$

Where we sum over the flavors of the quarks involved, that is to say the species of elementary particles and antiparticles.

The QCD Lagrangian structurally similar to QED in its expression but differs in a number of key aspects.

Firstly, QED interactions are mediated by photons while QCD is mediated by eight different gluons that differ among each other based on the color charge that they carry.

Only particles that present a color charge interact through the strong force, this includes all the quarks and the eight gluons. There are three forms of color charge are labelled as red, blue, and green with their respective anticolors. One of these colors can be assigned to any quark while gluons have a combination of one color and one anticolor. However, if these particles are joined in a combination that renders them color neutral, as is the case with hadrons or mesons, they will no longer interact via the strong force.

It's worth noting that, since gluons have a net color and they are the carriers of the strong force, they will be able to interact with each other. This will result in a process of anti-screening for the strong force as each gluon carrying the force ends up changing the color charge of the particle being observed. In practical terms, this means that the α_s coupling will change with the energy scale of the interaction Q. This scaling is of the form:

$$\frac{d\alpha_s}{dQ^2} = -\frac{\alpha_s^2}{12\pi Q^2}(33 - 2n_f) \tag{7}$$

where n_f is the number of flavors accessible. This leads to some interesting consequences as particles will interact more weakly over short distances (a property called asymptotic freedom) and more strongly over longer distances, leading to quarks and gluons not being able to exist as independent particles in nature but being forced into bound states such as baryons and mesons.

This behavior of the strong force means that, at high energies, it is possible to perform a perturbation series expansion for QCD. However, if a low energy system is being studied, it becomes necessary to use non-perturbative QCD to describe interactions.

A notable consequence of color confinement is the production of jets during high-energy QCD interactions as shown in Figure 10. These jets are cones of particles generated from the fragmentation of an object containing color charge. This occurs when a colored object moves away from any other particle that would allow it to form a color-neutral state. To preserve color confinement, the object creates a new colored counterpart to enforce color neutrality but it is possible that this pair is separated itself, leading to a repeated object creation process which makes up the jet.

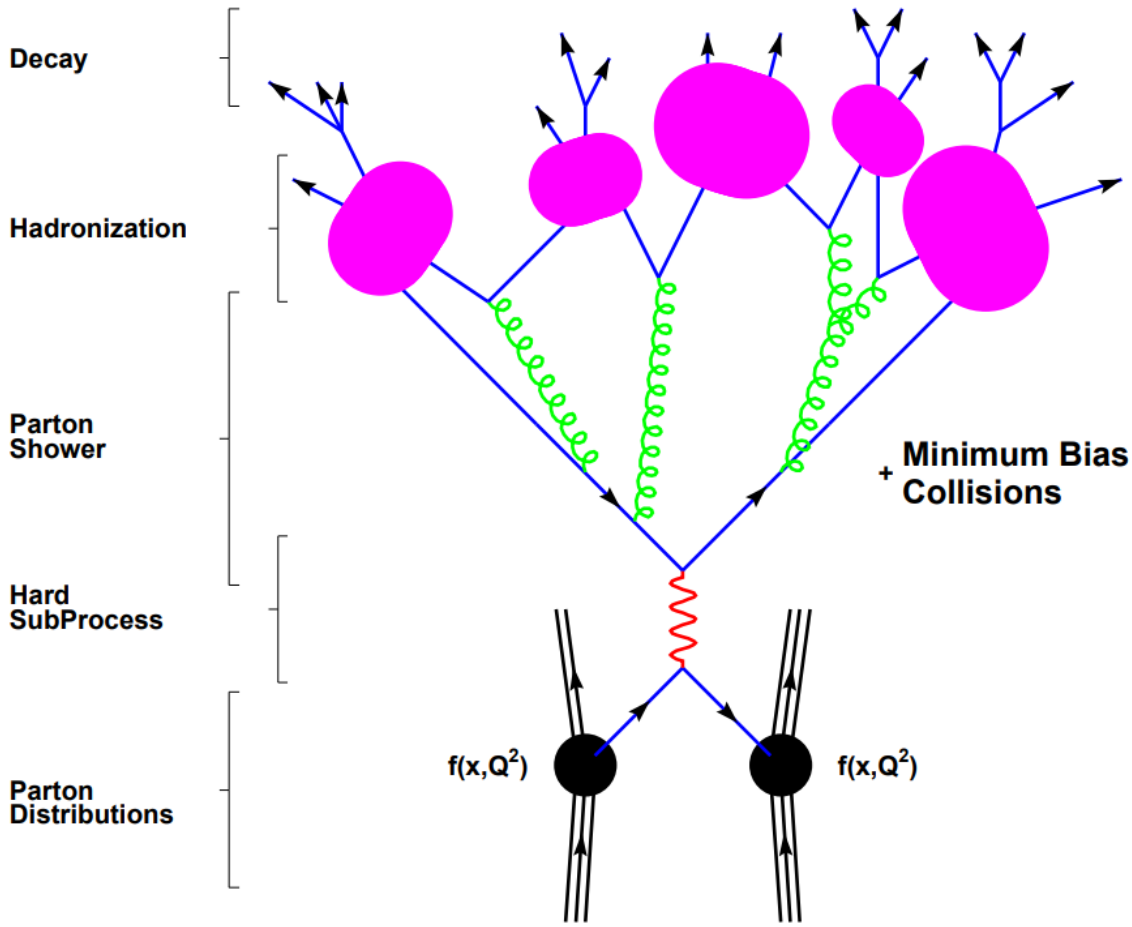

Figure 10: The basic structure of a QCD shower and hadronization. Figure originally from [35]

3.5 Full Standard Model Lagrangian

By combining the force descriptions in the previous sections with the field symmetries of the SM, it is possible to write the Lagrangian equation that describes the SM:

$$\mathcal{L}_{SM} = -\frac{1}{4}F^a_{\mu\nu}F^{\mu\nu}_a + i\bar{\psi}\not{D}\psi + |D_\mu\phi|^2 + \bar{\psi}_i y_{ij}\psi_j\phi + \mu^2\phi^\dagger\phi - \lambda(\phi^\dagger\phi)^2 + c.c. \tag{8}$$

Here the first term describes the gauge boson kinematics and any self couplings they might have where $F^a_{\mu\nu} = \partial_\mu A^a_\nu - \partial_\nu A^a_\mu + g\epsilon^{abc}A^b_\mu A^c_\nu$ with A being a gauge field, g its coupling and ϵ^{abc} the structure constant.

The second term is a term describing the fermion kinematics and their connection to the gauge bosons. In these terms, the covariant derivative $D_\mu = \partial_\mu - igT_a A^a_\mu$ and the respective $\not{D} = \gamma^\mu D_\mu$ are used with T_a being a matrix representing the symmetries of the field.

The third term describes the kinematics of the Higgs boson and its couplings to gauge bosons.

The last three terms describe the interaction of the Higgs boson with itself and fermions and will be treated in the following section.

3.6 The Higgs Boson

The Higgs boson was the last particle in the SM to be discovered and was first identified at CERN in 2012 [1, 2]. It is an unusual boson in that it does not mediate a force like the others but has a different role entirely in the SM.

The Higgs boson interacts with the fermions in the SM through the Yukawa interaction which adds a Lagrangian term:

$$\mathcal{L}_{fermion}(\phi, \psi) = \bar{\psi}_i y_{ij} \psi_j \phi \tag{9}$$

Where ψ is the fermion field, y_{ij} is the Yukawa coupling, and ϕ is the Higgs field whose minimum is chosen as:

$$\phi = \frac{1}{\sqrt{2}} \begin{pmatrix} \phi_0 \\ 0 \end{pmatrix} \tag{10}$$

where $\phi_0 = \sqrt{\frac{\mu^2}{\lambda}}$ is one of the minima of the potential.

It is then from this interaction that the mass of the fermions is derived through:

$$\mathcal{L}_{fermion}(\phi, \psi) = \bar{\psi}_i y_{ij} \psi_j \phi = m\bar{\psi}\phi\psi \tag{11}$$

resulting in a fermion mass prediction of $m = -\frac{\phi_0 y}{\sqrt{2}}$.

Within the SM, the interaction with the Higgs boson is the only difference between different generations of leptons and quarks so the Higgs mechanism should be the one that explains their differences.

At the LHC, the Higgs boson is primarily produced through the process of gluon fusion, where two gluons within the colliding protons interact with each other and most frequently form a loop of virtual quarks. These loops usually involve the heaviest quarks (in particular the top quark) due to their stronger interaction with the Higgs boson.

The other modes of production are all at least one order of magnitude smaller compared to the gluon fusion, the first of these is the vector boson fusion. Here, an interaction between two fermions is mediated by two Z bosons or a $W^+ W^-$ pair which fuse and thus produce the Higgs boson. The third mode of production is that of Higgs-Strahlung where a fermion collides with an anti-fermion which fuse into a Z or $W^{\pm}$ that in turn emits a Higgs boson. The final major decay process is the production of a Higgs boson in association with a top-antitop pair. These Feynman diagrams for these processes are presented in Figure 11.

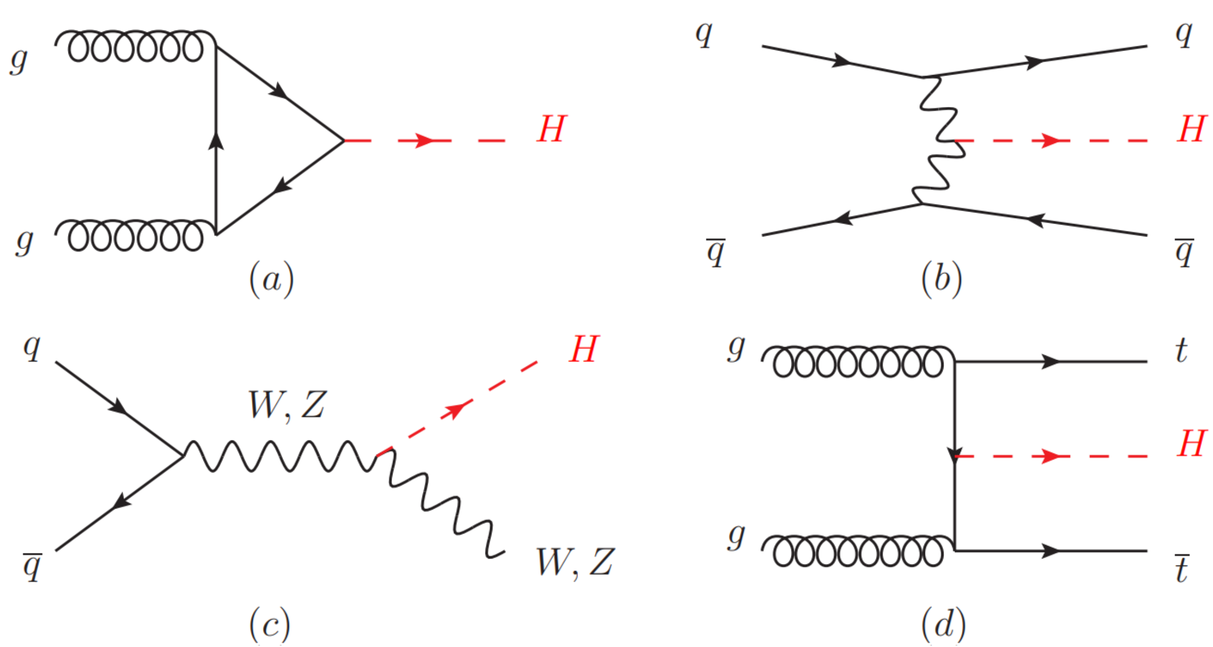

Figure 11: Feynman diagrams for the main modes of Higgs boson production at LHC. (a) gluon fusion, (b) Z/W fusion, (c) Higgs Strahlung and (d) Higgs production in association with a top-antitop pair. Figure originally from [36]

The Higgs boson's main mode of decay is into a bottom-antibottom pair (57% branching ratio(BR)), followed by a WW pair (21% BR), gluon-gluon pair (9% BR), tau-antitau pair (6% BR), charm-anticharm pair (3% BR), ZZ pair (3% BR), and other minor contributions [37]. the Feynman diagrams for these processes are shown in Figure 12.

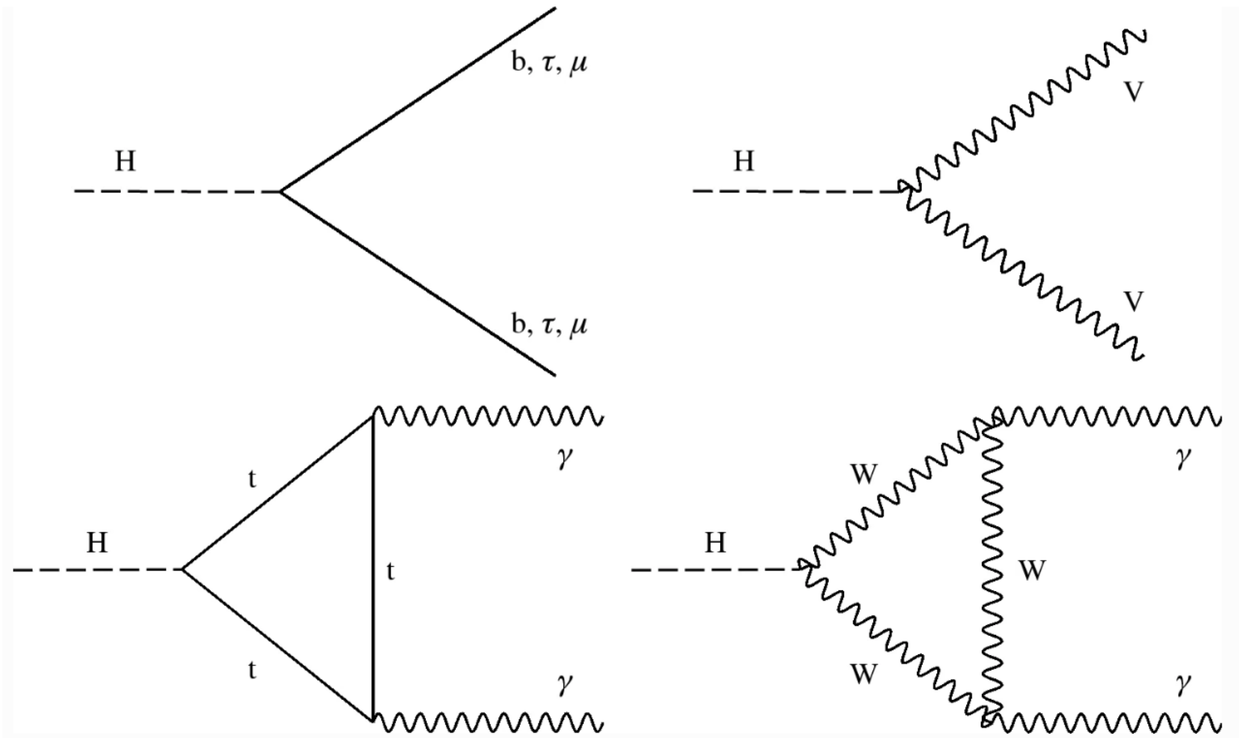

Figure 12: Feynman diagrams for the main modes of Higgs boson decay at LHC. Top-left Higgs to two fermions, top-right Higgs to Z/W, bottom row Higgs to two photons. Figure originally from [38]

3.7 Top and Bottom Quarks

This thesis studies a process involving the top and bottom quarks: the associated production of top quarks with bottom quarks. This will be explained in detail in Chapter 4

The top quark is the most massive particle in the SM and has an interesting relation to the Higgs boson due to its Yukawa coupling being close to one.

It was discovered at Tevatron in 1995 [39, 40] and, since then, a series of detailed studies have been carried out to better determine its properties and its place in the SM.

As previously mentioned, the top quark is the most massive particle in the SM which makes it interesting for searches of BSM physics in the case of heavier undiscovered particles having the top quark as a decay product. This is because particles tend to decay most frequently to the higher mass particles that can be produced and, for higher mass BSM particles, this would have the top quark as a significant decay product.

Furthermore, its strong coupling with the Higgs boson provides an interesting avenue into the study of the fermion mass hierarchy.

Recent measurements of the mass of the top quark and their combination can be seen in Figure 13.

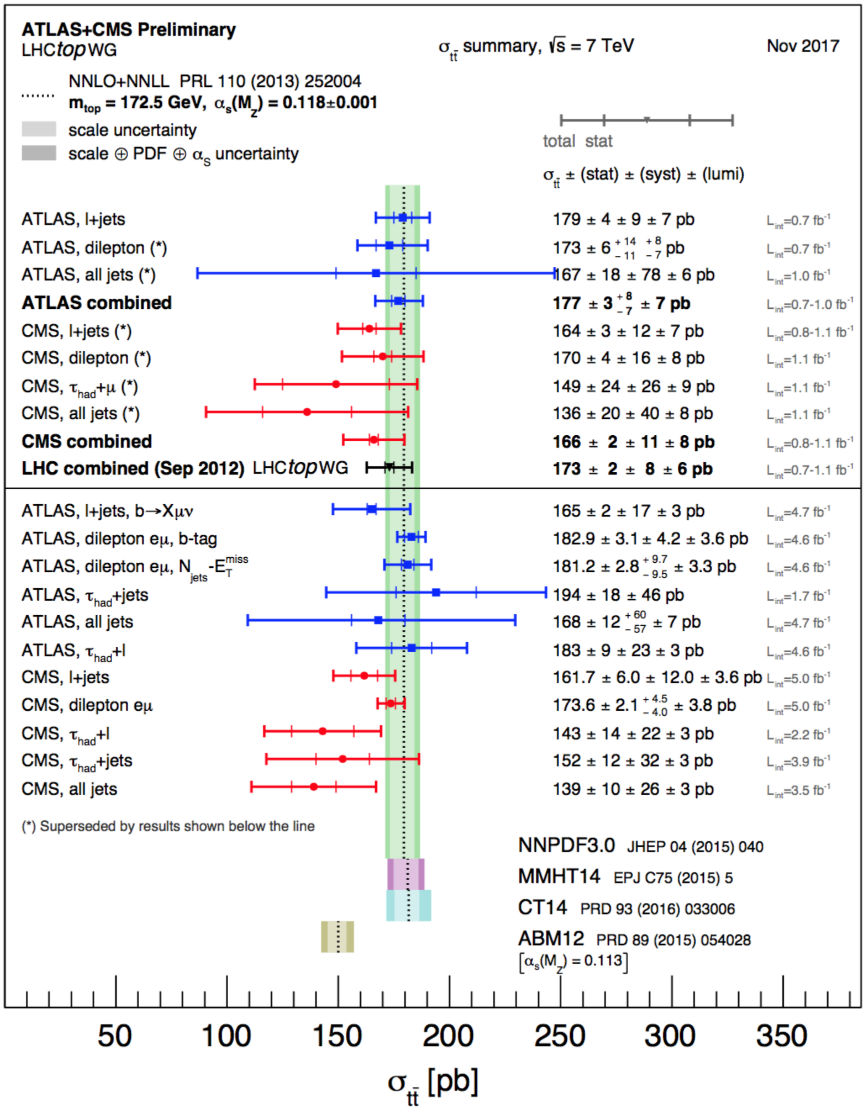

Figure 13: Summary of top mass measurements from the CMS and ATLAS experiments at CERN. Figure originally from [41]

Due to its very high mass, the top quark is only found naturally as a product of cosmic ray interactions (a proposal for their measurement can be found in [42]).

At LHC, it is most frequently produced as a top-antitop pair as a result of gluon fusion (90% BR) but can also be the result of quark-antiquark annihilation (10% BR).

It is also possible to produce single top quarks via the weak interaction where the top quark is produced by the interaction between a bottom quark and a W boson but, due to weak interactions being much weaker and less prevalent than strong interactions, this is a much less frequent process.

The Feynman diagrams of these production methods can be found in Figure 14.

Once produced, a single top quark will rapidly decay in about $5 \cdot 10^{-25}$s and do so as a $W^{\pm}b$ as shown in Figure 15.

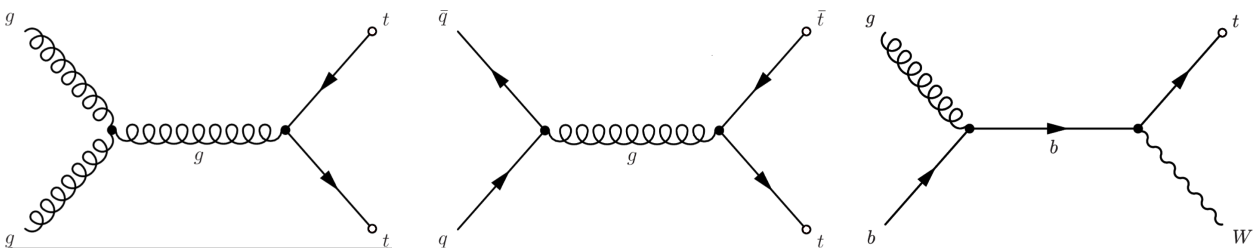

Figure 14: Different modes of production for the top quark. From left to right, in decreasing order of likelihood at LHC: gluon fusion, quark-antiquark annihilation, bW interaction

When a top-antitop pair has been produced, each top quark will decay independently and the further decay of the $W^{\pm}$ will determine the different topologies.

The most frequent decay mode (46% BR) is the fully hadronic mode where both $W^{\pm}$ decay to a pair of quarks and result in a total of 6 jets in the final state.

Next is the semileptonic decay mode (45% BR) where only one $W^{\pm}$ decays to a quark-antiquark pair while the other decays leptonically resulting in an electron, muon or tau with the respective neutrinos, each lepton having the same BR.

Last is the dileptonic mode (9% BR) where both $W^{\pm}$ decay leptonically.

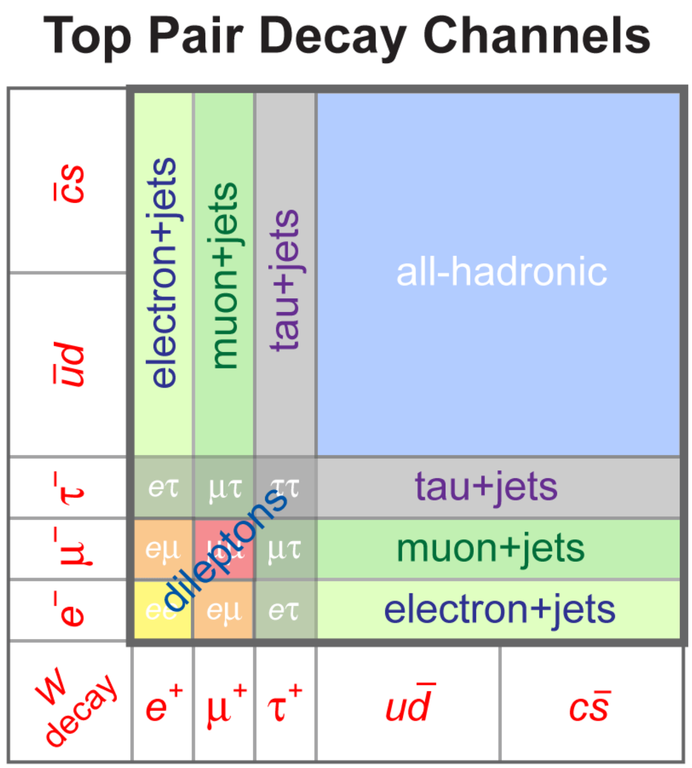

Figure 15: Decay channels for top quark pairs based on the decays of the W bosons. Image originally from [43]

These three modes of decay offer different advantages and difficulties for their study.

The dileptonic mode is the easiest to study at LHC because of a reduced number of background events and the ability to detect and reconstruct leptons with precision. However, it is limited by its low branching ratio which greatly reduces available data and by the presence of two neutrinos which are not reconstructed.

The fully hadronic mode has the advantage of being a much more frequent process and being fully reconstructible due to the absence of neutrinos in the decay. In contrast, it is limited by the large background present and difficulties in the reconstruction and identification of the jets present in the final state.

The semileptonic mode offers a compromise between the two previous ones and can be a useful means of study of the top decay as it combines a high branching ratio with a limited background and reduced final state multiplicity

The bottom (b) quark was discovered in 1977 at Fermilab [44] and is the other third-generation quark in the SM and is the main decay product of the top quark. It is about forty times less massive than the top quark and is notable because mesons containing the b quark are particularly long-lived in spite of their mass. This is because the b quark can only decay to a charm quark or up quark through the weak interaction giving a bottom particle lifetime of the order of 10^{-12}s.

These properties allow for the identification of b quarks using the b-tagging technique.

This technique takes into account the hadronization process for b quarks where a b quark will produce hadrons to ensure color neutralization via the strong force. The hadron containing the b quark is then called a b hadron and will eventually decay itself. However, the hadronization of the b jet will produce many other hadrons in a narrow cone, a feature called a "jet". When it is generated by the hadronization of a b quark, it is then identified as a b jet.

b-tagging takes advantage of the properties of b jets (shown in Figure 16), in particular:

- The b quark's large mass compared to its decay products provides the jet particles with a large transverse momentum. This, in turn, widens the b jet which will contain more particles with a high invariant mass.
- The relatively long lifetime of b hadrons allows them to travel into the detector. The construction of the detector will then allow for the identification of this secondary vertex which, in combination with the previous jet qualities, can be a sign of a b decay.

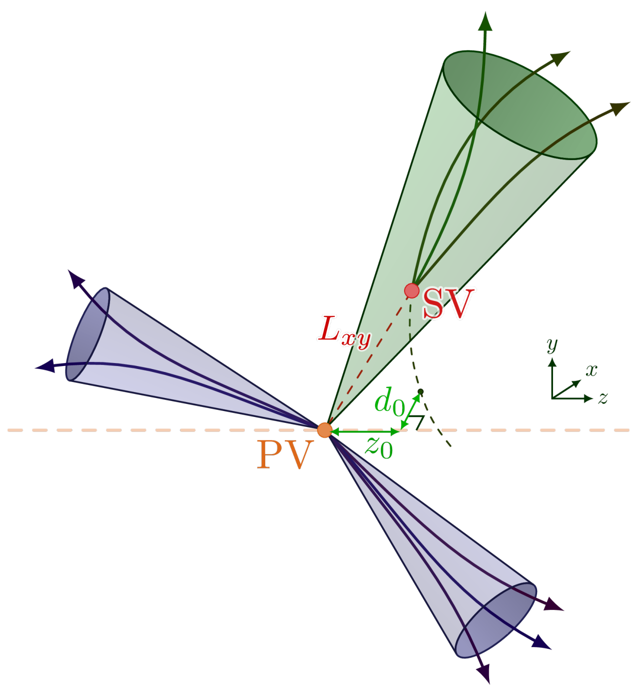

Figure 16: B jet displaying the properties used in b tagging such as the presence of a primary vertex (PV) and secondary vertex (SV). Image originally from [45]

However, it is important to note that the large transverse momentum, high invariant mass, and secondary vertex are only indicators of a b jet and do not convey certainty. Later in this work, the challenges and methods of b tagging will be discussed in more detail.

Part I

Measurement of the Inclusive and Differential Cross-Sections for Semileptonic $t\bar{t}b\bar{b}$ Production with the CMS Detector at CERN

4 Introduction

4.1 Motivation

Since the discovery of the Higgs boson, attention has shifted from its discovery to the measurement of its properties with the Yukawa coupling to the top quark playing an important part in the study. This, together with the fact that the top quark has the highest mass in the SM, points to the top quark and Higgs boson as prime candidates to probe the consistency of the SM Higgs sector. At the same time, these properties also indicate the Higgs boson and the top quark as useful stepping stones toward the study of BSM phenomena, particularly at higher energy scales.

In this line of study, the differential measurement of the top-antitop quark production in association with b-quarks ($t\bar{t}b\bar{b}$) process is of great interest for its dual role in aiding tests of the consistency of the SM and a potential probe for BSM physics.

The Feynman diagram of $t\bar{t}b\bar{b}$ in the semileptonic decay mode can be seen in Figure 17.

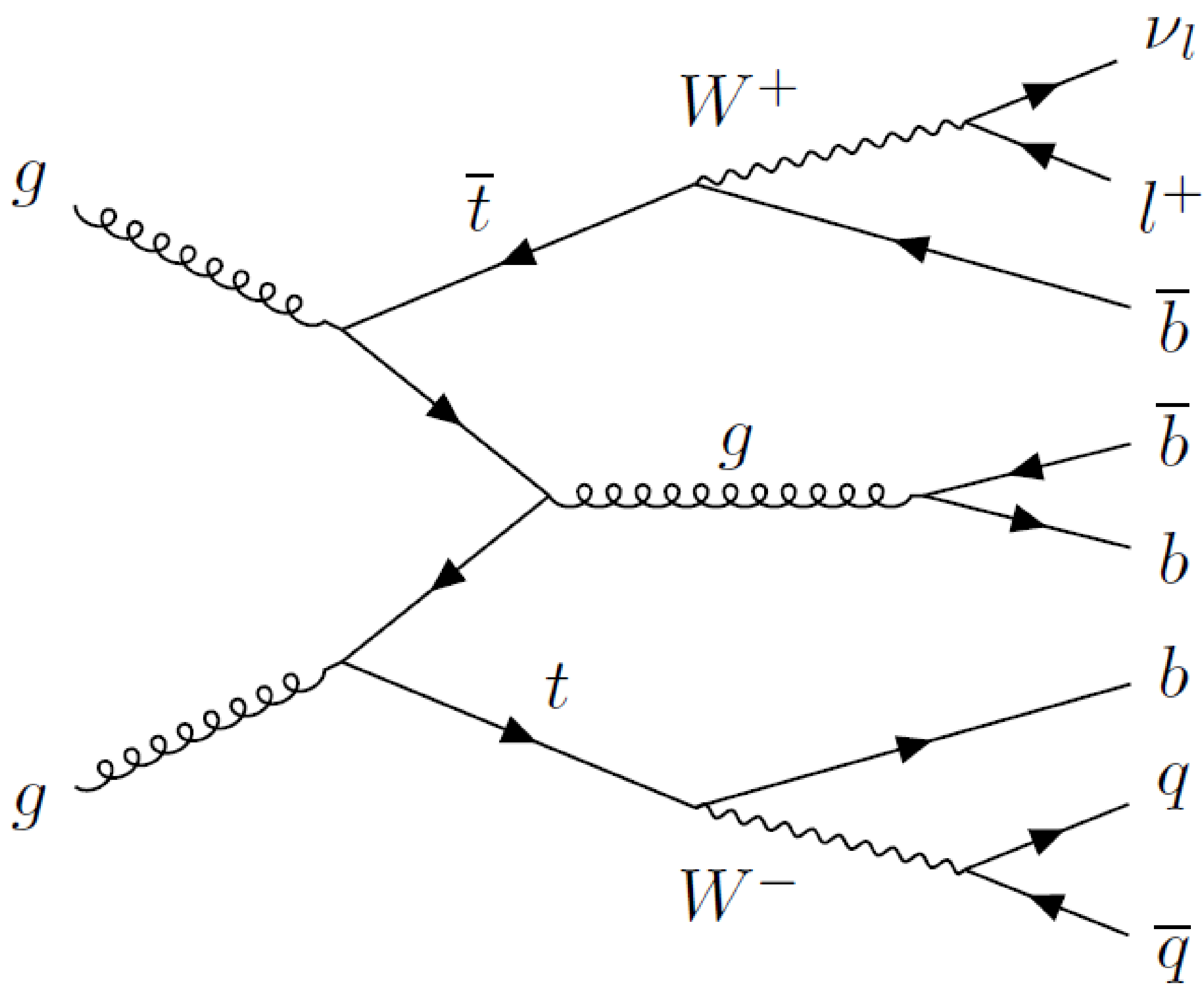

Figure 17: Feynman diagram of the SM $t\bar{t}b\bar{b}$ process.

In SM physics at the LHC, $t\bar{t}b\bar{b}$ has a significant role as a background for $t\bar{t}H$ production with $H \to b\bar{b}$ [46] [47]. The main uncertainty in this process derives from the modeling of $pp \to t\bar{t}b\bar{b}$ [48] and this can be reduced by the combination of improvements in the theoretical description of $t\bar{t}b\bar{b}$ and direct experimental studies.

Experimental studies can point to issues with the theoretical calculations. For instance, recent measurements of the $t\bar{t}b\bar{b}$ cross-section have been observed to surpass predictions by $30-50\%$ [48] [49] [50].

In general, fixed-order calculations of a given process are hard to compare to experimental results due to difficulties with the phase space definition and the necessity of limiting the calculation to the acceptance of the detector. A type of calculation that allows for smoother comparisons to experimental results is the matching of matrix element generators to parton showers. Models with different types of assumptions can be used for this [51, 52, 53, 54, 55, 56] with the most up to date method for $t\bar{t}b\bar{b}$ consisting of simulations at Next to Leading Order (NLO) QCD which considers the mass of the b quark [57, 58, 59].

This can be combined with the importance of experimental measurements of the production cross-sections for $pp \rightarrow t\bar{t}j\bar{j}$ and $pp \rightarrow t\bar{t}b\bar{b}$ to test the validity of the NLO calculations for QCD [60].

The $t\bar{t}b\bar{b}$ process can enters as a background to potential BSM phenomena. This can be either through searches with a $t\bar{t}b\bar{b}$ signature or by comparing with modified SM approaches such as Effective Field Theory. In particular, in studies on third-generation quarks, the $t\bar{t}b\bar{b}$ [61] final state is a good middle ground between $b\bar{b}b\bar{b}$ (difficult to b-tag and distinguish from the QCD background) and $t\bar{t}t\bar{t}$ (strongly suppressed due to its high mass) since it reduces the aforementioned difficulties while maintaining the connection to the potential BSM physics.

The analysis presented in this thesis is an inclusive and differential cross section measurement of the $t\bar{t}b\bar{b}$ final state in the semileptonic decay mode i.e. the mode where only one of the W bosons involved decays to a lepton. The analysis used datasets collected during the so-called Run 2 at CMS between 2016 and 2018. This resulted in the collection of a total integrated luminosity of 138 fb^{-1}, allowing for a higher precision than yet seen while being the first semileptonic $t\bar{t}b\bar{b}$ inclusive and differential cross section measurement performed at CMS with Run 2 data.

4.2 Previous Work

4.2.1 Cross-section Measurements

Theoretical calculations [48] have been made for the $t\bar{t}b\bar{b}$ cross section at Leading Order (LO) and Next to Leading Order (NLO) where the uncertainty is to be found between 20% and 30%. Specifically, at LO, the $t\bar{t}b\bar{b}$ cross-section is calculated to be $0.3738^{+70\%}_{-38\%}$ pb while, at NLO, it is calculated as $0.674^{+27\%}_{-25\%}$ pb [48]. The authors note that the rate of production for an extra light-jet for $t\bar{t}b\bar{b}$ is around 50% and, as such, every second $t\bar{t}b\bar{b}$ event involves a hard light-jet with $p_T > 50$ GeV. In the interest of studying the behavior of $t\bar{t}b\bar{b}$ events with the presence of additional light-jet radiation, which is important for NLO calculations, the behavior of $t\bar{t}b\bar{b}j$ events was studied. These $t\bar{t}b\bar{b}j$ events have a LO cross-section of $0.2316^{+92\%}_{-45\%}$ pb and a NLO cross-section of $0.337^{+15\%}_{-25\%}$ pb [48].

The CMS Collaboration has performed measurements on the relation between the cross-sections of $t\bar{t}b\bar{b}$ and $t\bar{t}j\bar{j}$ for pp collisions at $\sqrt{s} = 13$ TeV with 2016 data. This was undertaken as a useful test of NLO QCD calculations since the ratio between $t\bar{t}b\bar{b}$ and $t\bar{t}j\bar{j}$ cross-sections has a smaller relative systematic uncertainty than measurements of the absolute cross-section, due to the partial cancellation of uncertainties [60]. These measurements were performed separately for the semileptonic and dileptonic (both W bosons decay to leptons) cases. The results of the latter are shown in Figure 18 while the results of the ratio between $\sigma_{t\bar{t}b\bar{b}}$ and $\sigma_{t\bar{t}j\bar{j}}$ can be seen in Figure 19.

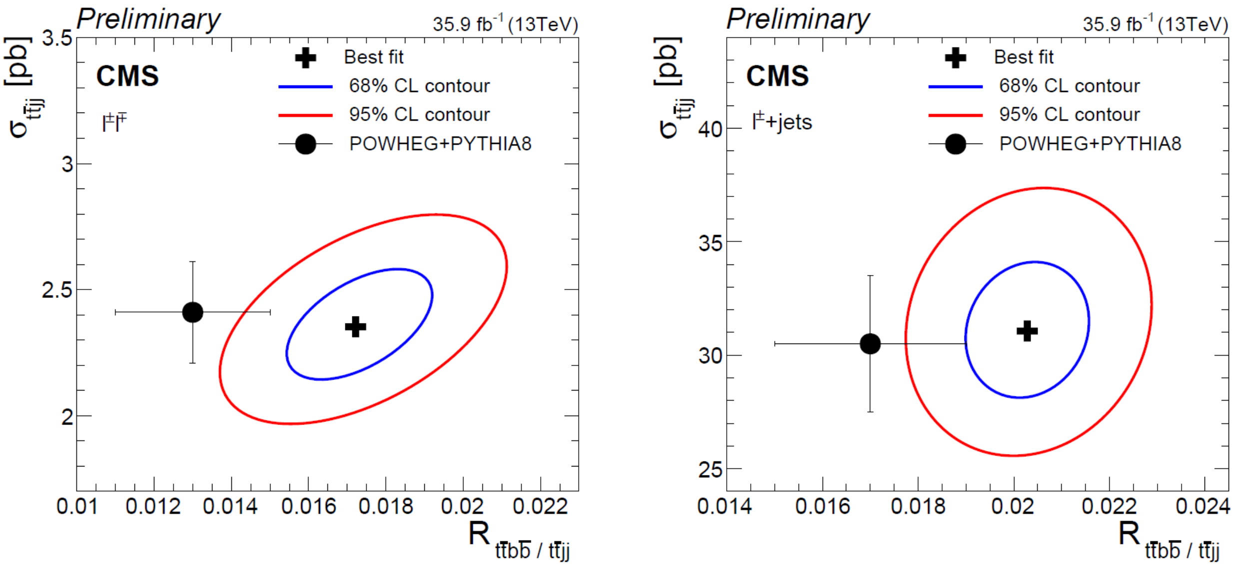

Figure 19: Results of a simultaneous fit for the ratio between $\sigma_{t\bar{t}b\bar{b}}$ and $\sigma_{t\bar{t}j\bar{j}}$ with $\sigma_{t\bar{t}j\bar{j}}$ (denoted as "Best fit"). The 1 σ and 2 σ confidence level intervals are also shown in blue and red respectively and compared with the POWHEG+PYTHIA8 prediction. The left plot displays results for the dileptonic channel and the right plot from the lepton+jets channel. Image from [60].

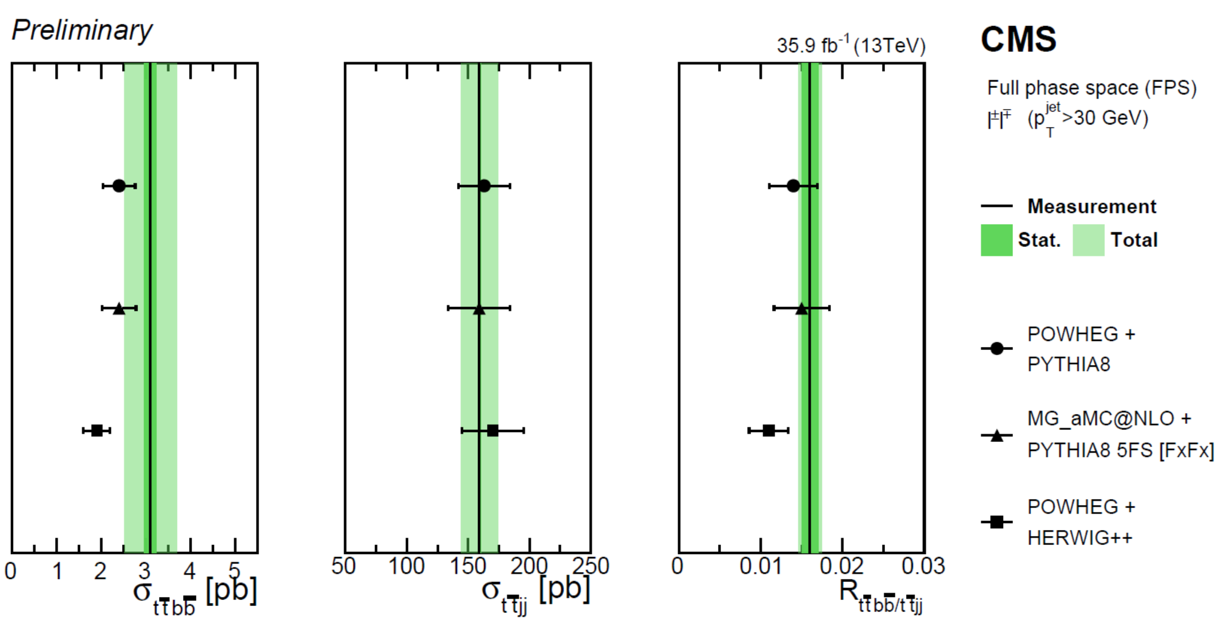

Figure 18: Summary of the $t\bar{t}b\bar{b}$ and $t\bar{t}j\bar{j}$ cross sections and their ratio in the dilepton channel, compared to the theoretical predictions of different generators. Image from [60].

The uncertainty in $\sigma_{t\bar{t}j\bar{j}}$ is mainly dominated by the theoretical uncertainties related to the parton showers which become relevant in this final state containing a large number of jets, and the uncertainties related to the Monte Carlo (MC) simulations used as a comparison to the measurements. However, the main experimental uncertainty is the uncertainty on the b-tagging efficiency calculation.

The cross-section measurements were compared to MC simulation predictions based on the POWHEG

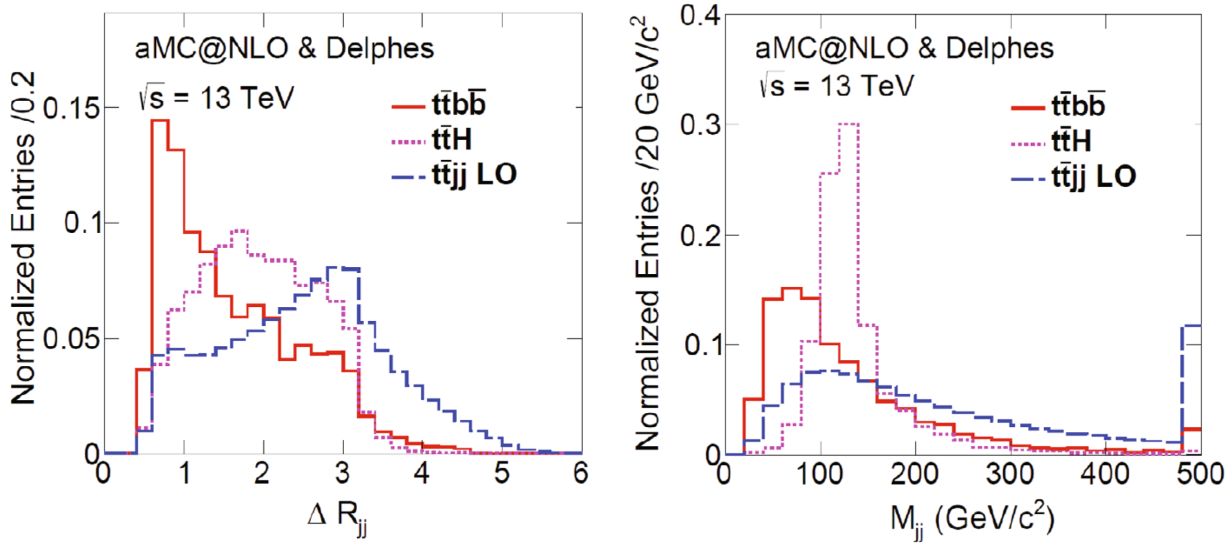

Figure 20: $\Delta R_{j\bar{j}}$ and $M_{j\bar{j}}$ distributions for the first and second additional jets which are not from top quark in the dileptonic mode. Image from [68].

computer framework which implements NLO calculations in shower MC programs [62, 63, 64, 56, 65, 66, 67]. When comparing $\sigma_{t\bar{t}j\bar{j}}$ and $\sigma_{t\bar{t}b\bar{b}}$ to the POWHEG MC predictions, the inclusive cross-sections in the Visible Phase Space (VPS) are in agreement for both decay channels. However, the cross-section ratio measured in the VPS is higher than POWHEG predictions by three standard deviations for the dileptonic channel while being more consistent in the semileptonic channel.

In Ref [68], the differential distribution of $t\bar{t}b\bar{b}$ was compared to $t\bar{t}j\bar{j}$ and $t\bar{t}H$ using data corresponding to an integrated luminosity of 10 fb^{-1} and $\sqrt{s} = 13$ TeV.

Two b-jets were required to select the $t\bar{t}$ events while one more b-jet was required to exclude single top and Drell-Yan events. They then studied the potential difference in the kinematic distributions of the jets that do not derive from top quarks by relying on Monte Carlo information to identify the origin of the jets. The additional b-jets are identified at the reconstruction level as the two b-jets closest to each other in ΔR. The results for the dileptonic decay mode of the $t\bar{t}b\bar{b}$ process can be seen in Figure 20 where it is noted that the additional b-jets in the $t\bar{t}b\bar{b}$ event tend to have a softer p_T and a more central pseudorapidity than the other two events. Furthermore, it can be noted that the $t\bar{t}H$ events have a clear peak at 125 GeV/c^2 in the invariant mass of the extra jets while the ΔR between these jets is smallest for $t\bar{t}b\bar{b}$ events.

The behavior of relevant variables in the semileptonic mode, seen in Figure 21, tends to match the one found in the dileptonic analysis with the extra b-jets in $t\bar{t}b\bar{b}$ and $t\bar{t}H$ tend to have a softer p_T spectrum. ΔR, $t\bar{t}b\bar{b}$ presents a distribution that is peaked lower than the other two, $t\bar{t}j\bar{j}$ displays wider angles while $t\bar{t}H$ is to be found in between the other two. Where the invariant mass is concerned, $t\bar{t}H$ presents a distinctive peak at 125 GeV/c^2 which distinguishes it from the other two events.
The results deviate from those of the dileptonic case when one takes into account the pseudorapidity as the $t\bar{t}j\bar{j}$ events display a more centered distribution than previously observed.

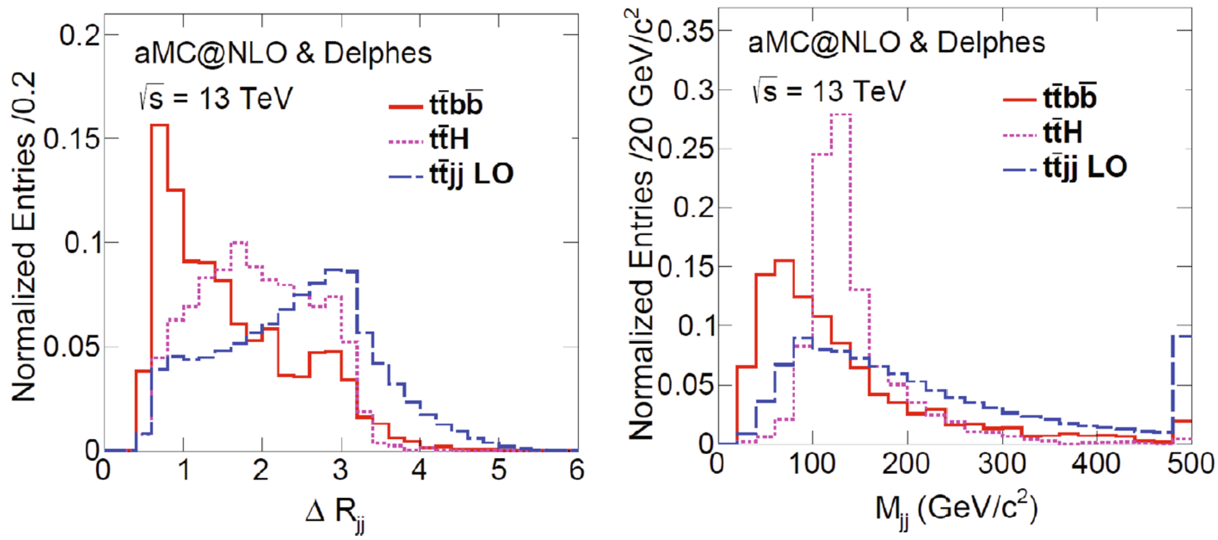

Figure 21: $\Delta R_{j\bar{j}}$ and $M_{j\bar{j}}$ distributions for the first and second additional jets which are not from top quark in the semileptonic mode. Image from [68].

4.3 Analysis Strategy

The analysis that will be presented relies on the semileptonic mode of $t\bar{t}b\bar{b}$ decay requiring exactly one electron or muon in the final state, without taking into account decays via tau leptons.

The ATLAS and CMS collaborations previously obtained measurements of the inclusive and differential $t\bar{t}b\bar{b}$ cross sections at $\sqrt{s} = 7$, 8 and 13 TeV in final states with zero, one, or two charged leptons, using up to 41.5 fb^{-1} of integrated luminosity [69, 70, 71, 72, 61, 73, 74, 60, 75].

This analysis provides the first differential measurement for semileptonic $t\bar{t}b\bar{b}$ production at CMS with the full LHC Run II dataset consisting of data recorded between 2016 and 2018 with a center of mass energy of $\sqrt{s} = 13$ TeV, amounting to a total integrated luminosity of 138 fb^{-1}.

The differential cross section is then calculated relative to a number of different kinematic observables, the most important of which are related to the $b\bar{b}$ pair.

These cross-sections are then compared to those derived from a number of different Monte-Carlo generators with different calculation methods and assumptions.

An important element of the analysis is the determination of which b jets are the so-called "additional" b-jets, that is to say which b jets are not derived from the decay of a top quark. Note that the origin of a jet is not an observable that can be determined independently of model but is constrained by the generator that is being considered. This is addressed with the use of a simple kinematic approach to provide a suitably high sensitivity without depending too strongly on modelling assumptions.

The cross-sections are measured in four different phase spaces all of which require the presence of exactly one isolated electron or muon and at least five jets, three of which have to be b jets. This basic selection is to keep into account the $t\bar{t}b\bar{b}$ events where either one of the bottom quarks was out of acceptance or the two b-quarks merged into a single b-jet. This selection can be made more stringent with a requirement of at least six jets, four of which are b jets. This selection is to study the fully-reconstructed $t\bar{t}b\bar{b}$ events where all jets in the decay have been identified and accepted. Finally, each of these two selections can be modified with the requirement of one extra light-jet to consider additional light radiation. This results in selections with at least six (seven) jets, three (four) of which should be b jets and three non-b jets.

The analysis proceeds by unfolding the data with a maximum likelihood fit which combines data from all years and channels.

The first step in this analysis to be discussed will be the definition of the different phase spaces, objects, and observables that will be used throughout.

5 Phase Space and Observables

The $t\bar{t}b\bar{b}$ cross sections are obtained by considering the final states of the $t\bar{t}b\bar{b}$ interaction and studying the particle-level kinematic observables of these end states before they interact with the detector. Particles are considered as belonging to the final state if they are quasi-stable with a lifetime of $\tau_0 \leq 10$mm/c.

The analysis investigates the semileptonic decay mode for the $t\bar{t}$ pair by requiring that there be exactly one muon or electron in the final state but without considering the decay history of the individual top quarks given at generator level. This approach guarantees that no fully-hadronic decay modes will be present because they have no charged leptons in their final state; however, it is possible that dileptonic events will pass this selection if only one of their charged leptons is identified within acceptance. In practice, this is not a problem for the analysis since the dileptonic contributions are too small to impact our results. This chapter will detail the different phase spaces and definitions of objects that are used in the analysis together with the observables whose cross-sections will be measured.

5.1 Phase Spaces

All selections in the analysis require exactly one muon or electron to be present in the final state and veto any additional electrons or muons. Four separate phase spaces are then further defined to target different cases:

6j4b requires a minimum of six jets, four of which must be identified as b jets. This selection is the primary one used in this analysis and takes into account those cases where all the final state b jets are within detector acceptance, in particular the two additional b jets.

5j3b requires a minimum of five jets, three of which must be identified as b jets. This selection is a less restrictive version of the previous one. Here the target are the $t\bar{t}b\bar{b}$ events where either one b jet ended up outside of detector acceptance or the two additional b quarks cannot be resolved and are grouped in a single b jet.

7j4b3l requires a minimum of seven jets, four of which must be identified as b jets, and three as non-b jets. This selection is an extension of 6j4b which takes into account additional light-jet radiation.

6j3b3l requires a minimum of six jets, three of which must be identified as b jets, and three as non-b jets. This selection is analogous to 7j4b3l and is an extension of 5j3b which takes into account additional light-jet radiation.

These phase spaces are represented visually in Figure 22.

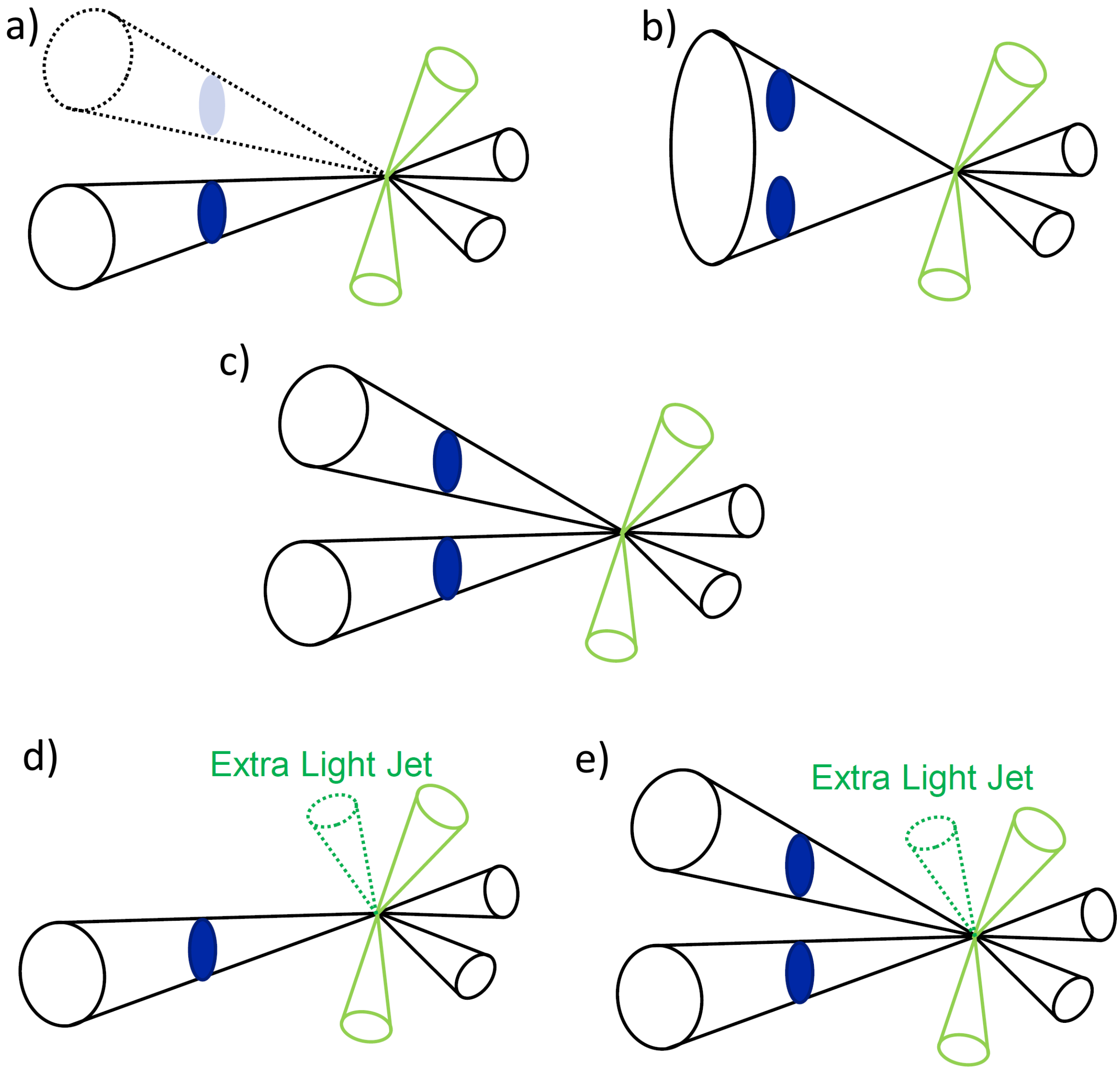

Figure 22: Diagram of the fiducial phase spaces in the analysis. a) and b) are the events targeted by the 5j3b selection with a) considering the case where one of the extra b-jets falls out of acceptance and b) the case where the two extra b-hadrons are grouped into one b jet. c) is the event targeted by the 6j4b selection. d) is the target of the 6j3b3l selection. e) is the target of the 7j4b3l selection. The b jets are represented in black, the extra b-hadrons in blue, and the light jets in green.

5.2 Object Definitions

Each phase space uses the same series of particle-level definitions for a number of different objects

Electrons are defined as generator level electrons or positrons where $p_T > 29$GeV and $|\eta| < 2.4$. An electron is further considered as "dressed" if it has any photons within ΔR ≤ 0.1. In such a case, the four-momentum of the photons is added to the electron.

Muons are defined as generator level muons or anti-muons where $p_T > 26$GeV and $|\eta| < 2.4$. The above definition of "dressed" applies in this case as well and dressed muons add the four-momentum of the photons within $\Delta R \leq 0.1$ to their own.

Veto Electrons are defined as any electron or positron where $p_T > 15$GeV and $|\eta| < 2.5$. The same dressing as above applies.These veto electrons are used to exclude dileptonic $t\bar{t}$ decays.

Veto Muons are defined as any muon or anti-muon where $p_T > 15$GeV and $|\eta| < 2.4$. The same dressing as above applies.These veto muons are used to exclude dileptonic $t\bar{t}$ decays.

Jets are defined as jets clustered using the anti-k_T algorithm [76, 77] with a radius parameter R = 0.4. This is done by considering all stable particles except neutrinos at generator level. A further restriction is added by requiring that all jets have $p_T > 25$GeV and $|\eta| < 2.4$. Any jet found within $\Delta R < 0.4$ of a hard isolated electron or muon (defined as above) is not considered.

b Jets are defined as jets (defined as above) which have been associated to a hadron containing a b quark via *ghost matching*. This ghost matching consists in taking the four-momentum of the hadron and maintaining its direction while reducing its magnitude to a negligible value. The jet clustering is then re-run with this configuration and the hadron can be considered ghost matched to the jet within which it is clustered [78].

Light Jets are defined as any jet (defined as above) which is not ghost matched to either a hadron containing a b or c quark.

5.3 Observables

The observables studied in this analysis are derived in part from previous studies [79, 71, 80]. These observables are all defined based on the stable particles in the end state of the event without taking into account their history. This allows for direct comparison between the detector-level observations and the observables defined below. Also, it guarantees that the observable definition is independent of the generators being used and allows for comparison to multiple generators. This is both valuable during the analysis itself where data can be compared to a number of different predictions and after the analysis has been completed to allow for easy comparison of the results with future generators.

However, this approach does not allow for an immediate distinction between b jets that are derived from top decay and those generated by gluon splitting. Within the 6j4b selection, the two b jets derived from gluon splitting are referred to as "additional b-jets" (bb^{extra}) to better probe this aspect of the physics. To identify which pair of b jets corresponds to the desired additional b-jets, it was decided to use particle level information about these jets to determine their angular separation ΔR_{bb} defined as:

$$\Delta R_{bb} = \sqrt{(\Delta\phi_{bb})^2 + (\Delta\eta_{bb})^2} \tag{12}$$

The bb^{extra} jets are thus determined as the pair of jets in the event with the smallest ΔR_{bb} between them. This approach allows for proper identification of the extra jets for 45% of events. Attempts were made to identify the bb^{extra} pair with other observables such as selecting the third and fourth b-jets when sorted by p_T but this approach proved to be less effective with a correct identification rate of 30%.

In the 5j3b selection, it is not possible to directly identify the bb^{extra} pair either because one of these jets fell out of acceptance or because the pair is combined into a single jet. As such, the kinematics of the b jets derived from gluon splitting can be best studied by observing the third b-jet when sorted by p_T. In this case, this allows for correct identification of one of the bb^{extra} jets in 50% of events in the 5j3b selection.

In the 6j3b3l and 7j4b3l selections, the object of study is the additional light jet radiation so no special attention is paid to the b jets in the system. In these cases, the two light jets closest to the mass of the W boson are excluded since they are likely derived from W-boson decay and then the kinematics of the remaining one or two light jets is studied.

The inclusive cross section σ_{tot} is calculated for all phase spaces. The observables considered are separated by the phase space considered and are the following:

In the 5j3b phase space we measure:

- the number of jets in the event, N_{jets};
- the number of b jets in the event, N_b;
- the p_T and $|\eta|$ of the 3rd b jet, $p_T(b_3)$, $|\eta(b_3)|$;
- the scalar sum of the p_T of all jets, H_{T}; and
- the scalar sum of the p_T of all b jets, H_{T}^b.

In the 6j4b phase space we measure:

- the number of jets in the event, N_{jets};
- the p_T and $|\eta|$ of the 3rd and 4th b jets, $p_T(b_3)$, $p_T(b_4)$, $|\eta(b_3)|$, $|\eta(b_4)|$;
- the scalar sum of the p_T of all jets, H_{T};
- the scalar sum of the p_T of all b jets, H_{T}^b; and

  considering all possible bb pairings:

  - the average $\Delta\mathrm{R}_{bb}$ over all pairings, $\Delta\mathrm{R}_{bb}^{\text{avg}}$; and
  - the largest invariant mass, $\mathrm{m}_{bb}^{\text{max}}$.

  and for the bb pair with the smallest $\Delta\mathrm{R}_{bb}$, denoted by bb^{extra}:

  - the opening angle between the two b jets of the pair, $\Delta\mathrm{R}_{bb^{\text{extra}}}$;
  - the invariant mass of the pair, $\mathrm{m}(bb^{\text{extra}})$;
  - the p_T of the pair, $p_T(bb^{\text{extra}})$; and
  - the $|\eta|$ of the pair, $|\eta|(bb^{\text{extra}})$; and
  - the p_T and $|\eta|$ of the leading and sub-leading b jets in the pair, $p_T(b_1^{\text{extra}})$, $p_T(b_2^{\text{extra}})$, $|\eta(b_1^{\text{extra}})|$, $|\eta(b_2^{\text{extra}})|$.

In the 6j3b3l and 7j4b3l phase spaces the observables considered are:

- the p_T of the first remaining light jet, $p_T(\mathrm{lj}_1^{\text{extra}})$;
- the azimuthal angle between the hardest remaining light jet and the softest b jet, $|\Delta\phi(\mathrm{lj}_1^{\text{extra}}, b_{\text{soft}})|$; and
- the scalar sum of p_T of the light jets in the event, $H_{\mathrm{T}}^{\text{light}}$.

5.4 Signal and Background Definitions

For all the phase spaces mentioned above, the signal component is defined as the component matching the phase space definition at generator level. On the other hand, the background is defined as the component that satisfies the detector level selection but not the generator level requirements. But, while the signal is not further subdivided, the $t\bar{t}$ background components are split further into a number of categories for fitting purposes. The categories for events of the form $t\bar{t}$ + jets are distinguished by the presence of different hadrons in the outgoing jets. This categorization is done by the `GenHFHadronMatcher` tool [81, 82] where the flavor is determined by ghost matching (as is the case for the b jets defined above) combined with the Monte-Carlo history of the identified jets. This allows for a separation into three separate categories:

- $t\bar{t}$B which includes all events with a minimum of one b-jet

- $t\bar{t}$C which includes all events without additional b-jets but a minimum of one jet containing a c hadron (c jet). This category is separate from the $t\bar{t}$+light as the c jets are more likely to be mistaken for b jets and have dedicated systematic uncertainties.
- $t\bar{t}$+light which includes all remaining $t\bar{t}$ + jets events not included in the previous two categories

The $t\bar{t}$B events defined above are further split into $t\bar{t}$B proper where the event is within the fiducial phase space and is selected at detector level and $t\bar{t}$B out-of-acceptance (OOA) where the event has been selected at detector level but falls outside of the fiducial phase space. These $t\bar{t}$B OOA events are thus treated as background. However, given that the $t\bar{t}$B OOA events found in the 6j4b phase space can have either one or two additional b-jets, it becomes necessary to distinguish the two configurations due to their different topology. The case with a single additional b-jet is labeled as $t\bar{t}b$ OOA while the one with two additional b-jets is labeled $t\bar{t}b\bar{b}$ OOA. This difference is then used for correlation purposes between systematics. A schematic overview of these divisions can be found in Figure 23.

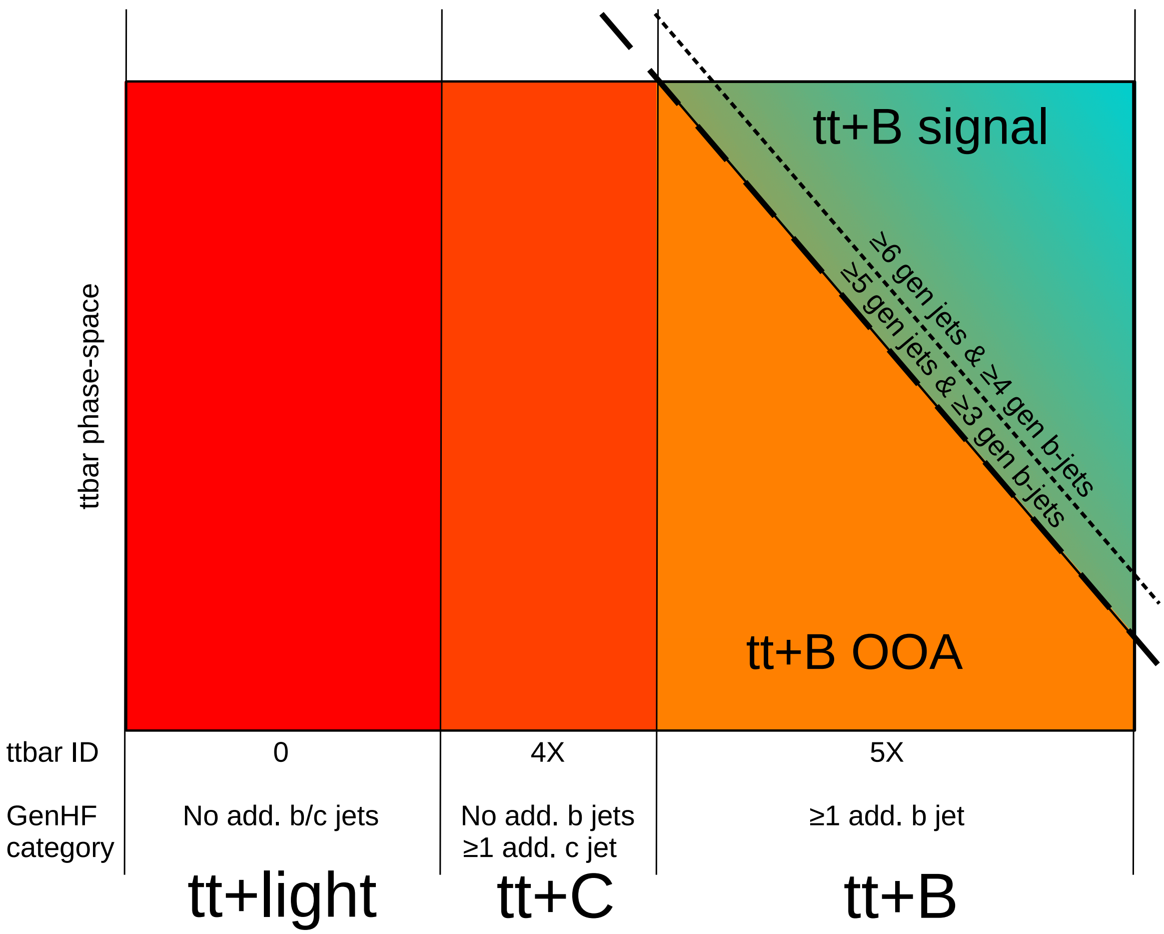

Figure 23: Overview of the $t\bar{t}$ + jets division into $t\bar{t}$+light, $t\bar{t}$C, and $t\bar{t}$B based on the presence of b or c jets. Also displayed is the subdivision of $t\bar{t}$B into signal and OOA components based on phase space

Background events are mostly comprised of $t\bar{t}$B OOA, $t\bar{t}$C, and $t\bar{t}$+light but there are a number of other minor contributions Among these are $t\bar{t}$ production with heavy bosons, single top-quarks, and vector bosons with additional jets. The first of these can be visualized as a single $t\bar{t}$X contribution, be subdivided into $t\bar{t}H$ and $t\bar{t}$V or the $t\bar{t}$V can be itself divided into $t\bar{t}$Z and $t\bar{t}$W.

6 Object and Event Selection

After having defined the phase spaces and observables used in the analysis, it becomes necessary to define how the event selection is done with the detector-level information

A set of detector-level selections are defined to match the object and event selections defined at generator level in Section 5. They are constructed in such a way as to ensure a good correspondnce between the generator-level definitions, the information available at detector level, and the underlying physics.

These may vary based on when the data in question was gathered, which is divided into data-taking "eras". These are 2017 and 2018 based on the year of collection while 2016preVFP and 2016postVFP are distinguished by the correction of a voltage bias problem within the detector during the 2016 data-taking period.

6.1 Trigger Requirements

Candidate events are first selected by using single lepton triggers which vary based on year and lepton.

The reconstruction of muons is performed from the outside of the detector working inwards, i.e. tracks are first fit in the outer muon spectrometer and these tracks are then used to reconstruct the tracks in the inner tracker. The isolation of the muon is obtained through a combination of tracker and calorimeter information followed by a subtraction of average pile-up energy.

The electron and muon triggers used in this analysis are listed in Table 1.

Table 1: Triggers used in the analysis

Year	Electron Trigger(s)	Muon Trigger(s)
2016	`HLT_Ele27_WPTight_Gsf`	`HLT_IsoMu24` OR `HLT_IsoTkMu24`
2017	`HLT_Ele28_eta2p1_WPTight_Gsf_HT150` OR `HLT_Ele32_WPTight_Gsf_L1DoubleEG`	`HLT_IsoMu27`
2018	`HLT.Ele32_WPTight_Gsf` OR `HLT_Ele28_eta2p1_WPTight_Gsf_HT150`	`HLT_IsoTkMu24`

Electrons are reconstructed through clusters of ECAL deposits that are used to match with tracks in the pixel detector where the momentum ratio is tracked via cuts on the energy of the cluster. The isolation requirement is fulfilled by considering data from the tracker and HCAL.

To avoid potential issues that might arise from the modelling edge conditions of the triggers where the lepton kinematics are near the requirement boundaries, the final requirements for the object selection are chosen to be more stringent than the triggers themselves.

6.2 Event Cleaning and Corrections

In p-p collisions, it is expected that total initial and final momentum in the transverse direction should be zero. However, the presence of weakly or non-interacting particles can cause an imbalance in the energy along the transverse direction which is called Missing Transverse Energy (MET).

To ensure that the events being used were taken under conditions where the MET is well understood [83], each event is tagged with a flag indicating its suitability, which is then used to veto events with properties that rendered the MET unreliable.

L1 prefiring takes into account a detector effect whereby certain objects are reconstructed in the incorrect bunch crossing and cause a veto of the bunch crossing that the object was originally part of [84].

One such issue presented itself with the ECAL in 2016 and 2017 where a gradual timing shift was not properly propagated and caused triggering information to be assigned to successive bunches. Given that the L1 trigger vetoes consecutive triggers, this caused the events in question to veto themselves. This effect was especially pronounced at a pseudorapidity of $2 < |\eta| < 3$.

A similar situation arises in the muon system where a self-veto can also be triggered by a mistaken muon assignment to the wrong bunch crossing. This effect is primarily present in 2016 data and has a η dependence that can amount to a 3% effect [85].

These effects are not considered directly in the simulation but are applied later as a correction that takes into account these self-vetoes. This correction is obtained by assigning a prefiring probability to each object in an event based on its kinematics. From these probabilities, the event is assigned its own probability as a product of the ones of the objects within the event. Once this final probability has been obtained, a reweighting factor is applied to the event based on this value.

6.3 Detector-Level Object Definitions

6.3.1 Electrons

Reconstructed electrons, much like their generator-level counterparts, are divided into two types with different roles. First, the primary electrons are used to identify the semileptonic decays of $t\bar{t}b\bar{b}$ events. Then the veto electrons are selected with looser criteria to serve as a veto for events with more than a single charged lepton. A summary of the selections used in the analysis for electrons can be found in Table 2.

Table 2: Selections used for electrons in the analysis.

	primary electrons		veto electrons
p_T [GeV] and $\|\eta\|$	$p_T > 29$ AND $\|\eta\| < 2.4$ ($p_T > 34$ AND $\|\eta\| < 2.4$) OR ($p_T > 30$ AND $\|\eta\| < 2.1$)	(2016) (2017,2018)	$p_T > 15$ AND $\|\eta\| < 2.4$
$\|\eta\|_{SC}$	< 1.4442 OR > 1.566		
IP cuts [cm]	$\|d_{xy}\| < 0.05$ AND $\|d_z\| < 0.1$ $\|d_{xy}\| < 0.1$ AND $\|d_z\| < 0.2$	($\|\eta\|_{SC} \leq 1.479$) ($\|\eta\|_{SC} > 1.479$)	

The electrons are reconstructed by using a multivariate analysis that takes into account the inner track with the energy deposited in the ECAL. A series of further criteria are applied to exclude other processes such as photon splitting into an electron positron pair or hadron decay [86].

The isolation of the electrons is taken into account with limits on the number of missing hits in the tracker, criteria related to photon conversion, angular compatibility between the track and ECAL deposits, and requirements defined by the ratio of the additional energy within the ΔR cone around the electron to the total electron energy [86].

The electron is also required to be compatible with an origin in the primary vertex. This compatibility is determined by considering the distance between the primary vertex and the nearest point of the reconstructed electron trajectory. This distance is not considered in the absolute but decomposed in the longitudinal direction (d_z) and in the transverse plane (d_{xy}). These components are considered separately and depend on the $|\eta|$ associated with the electron.

Regarding the kinematic and cut-based conditions, the veto electrons are required to have $p_T > 15$GeV and $|\eta| < 2.5$.

This is in contrast to the primary analysis electrons whose p_T and $|\eta|$ requirements vary based on years and kinematic considerations. The different p_T thresholds are designed to be as low as possible while maximising the signal selection efficiency by being just above the trigger activation level. It is relevant to note that these threshold variations are not significant for the analysis since the lepton kinematics are not among the observables considered and the leptons are only used for semileptonic event selection which results in a minimal correlation with the observables used in the analysis.

6.3.2 Muons

Muons are analogous to electrons in both their use and selection. Regarding their use, primary muons are used for the selection of semileptonic $t\bar{t}b\bar{b}$ events while veto muons have looser selection criteria and veto events with more than one charged lepton. A summary of the selections used in the analysis for muons can be found in Table 3.

Muons are reconstructed either by combining tracks in the inner tracker with tracks in the muon system in the outer region of the CMS detector (global muons) or by combining tracks in the inner tracker with segments (i.e. short straight-line tracks) in the muon system (tracker muons) [87].

Table 3: Selections used for muons in the analysis.

	primary muons		veto muons
p_T [GeV]	> 26 > 29	(2016,2018) (2017)	> 15
$\|\eta\|$	< 2.4		< 2.4
I_μ	< 0.15		< 0.25

As in the electron case, the muons used for veto purposes have a less stringent selection and can be either global or tracker muons matched to segments in the muon system. The selection for veto muons has a high efficiency but this is contrasted by a high misidentification rate.

The primary muons of the analysis instead place extra requirements on the muon reconstruction. To satisfy these criteria, the muon must be a global muon with additional cuts placed on the goodness of fit of the track, the number of muon chambers and stations matched to the track, the impact parameter of the track and the number of pixel and tracker layers containing hits from the muon track [87, 88]. Under these conditions, the muon identification efficiency is of around 95%.

A further selection that is considered is that of relative muon isolation I_μ which serves to reject muons not derived from the primary vertex but rather from hadron decays or fakes. A cone with size $\Delta R < 0.4$ around the muon is defined including all the charged particles originating from the primary vertex, as well as contributions from neutral particles, with a pileup corrections. Then the isolation is defined by considering the ratio of the scalar p_T sum of all particles in the previously defined cone, excluding the muon itself, to the p_T of the muon. Finally, kinematic requirements are also placed on the p_T and η of the muons used in the analysis.

6.3.3 Jets

Jet reconstruction begins with particle candidates derived from the particle-flow algorithm [89] identified using the anti-k_T algorithm [76, 77], with a distance parameter $R = 0.4$. A number of criteria are then applied in order to select the jets that are well-reconstructed while vetoing any leptons that have been mis-reconstructed as jets. The selection criteria for jets are found in Table 4.

Table 4: Selections used for jets in the analysis.

	jets
clustering algorithm	anti-k_T, $R = 0.4$
p_T [GeV]	> 30
$\|\eta\|$	< 2.4
$\Delta R_{\ell,j}$	> 0.4

A further selection is applied in the case where jets within $\Delta R < 0.4$ of any electron or muon (as defined in the previous sections) are removed. Also, jets are required to have $p_T > 30\,\text{GeV}$ and $|\eta| < 2.4$.

The jets then have their energy and four-momentum corrected depending on several jet-related quantities such as p_T and η.

To match the momentum resolution observed in data, smearing is applied to the simulated jet momenta. This is done with a hybrid method that smears the jet momentum relative to the momentum of the matched generator-level jet if one is available, if not, a stochastic smearing is applied.

6.3.4 B Jets

The DeepJet [90] b-tagging algorithm is used to identify jets with different working points based on the likelihood of a jet being a b jet.

If a jet satisfies the "medium" working point of the b-tagging classifier (which amounts to a 1% misidentification rate to light jets and 15% to charm jets for $t\bar{t}$B events [91] [92]), it will be assigned as a b-tagged jet. If a jet satisfies the "tight" working point (0.1% light-jet and 3% charm jet mistag rate for $t\bar{t}$B events [91] [92]), it will not be given a different definition but will be used for the definition of an ancillary variable for the fit as described in Section 7.3. The b-tagging discriminant values are displayed in Table 5 with separate values for eras and working points.

Table 5: Working points of the DeepJet b-tagging algorithm.

Year	Medium WP	Tight WP	
2016preVFP	0.2598	0.6502	[93]
2016postVFP	0.2489	0.6377	[94]
2017	0.3040	0.7476	[95]
2018	0.2783	0.7100	[96]

To account for variations in the b-tagging efficiencies between data and simulation, b-tagging scale factors are used [97].

The b-tagging scale factors used in this analysis are called "fixed working point" scale factors because they only correct the b-tagging discriminators in discrete bins based on the chosen working point, era, and kinematics of the jet. Corrections and their efficiencies are calculated individually for each event for both the medium and tight working points and are then applied to each jet based on the chosen working point. This is described further in Section 9

Without preselection of the number of b-tagged jets in the event, the application of these corrections should not affect either the shape or rate of the kinematic observables of the jets but only modify the b-tagging scale factor associated with the jets in the event. This behavior was verified for the fixed working point scale factors by studying kinematic distributions in phase space with ≥ 4 jets and no requirement on the number of b-tagged jets and can be seen in Figure 24.

6.4 Detector-Level Event Selection

Every fiducial phase space defined in Section 5.1 has a corresponding detector-level selection with a closely matching definition. This is to select events enriched in the process of interest and use a phase space where the detector-level quantities are well matched to the generator-level physics objects considered. The detector-level observables are then used to calculate the differential and inclusive cross sections following the unfolding process covered in Section 8.

Every event selection has the requirement that the event fire one of the electron or muon triggers as defined in Section 6.1 and it must satisfy the event-cleaning requirements described in Section 6.2.

Once these first conditions are satisfied, the semileptonic requirements are added by calling for exactly one electron or muon with no veto electrons or muons to be present, as is described in Sections 6.3.1 and 6.3.2. Note that to avoid overlap between the lepton triggers, the reconstructed lepton in each event is required to match its trigger; i.e. a reconstructed electron must correspond to an electron trigger and similarly for the muons. Each event is classified based on the lepton reconstructed, with separate detector level information for the two categories.

The different event selections are then defined based on the number of jets (defined in Section 6.3.3) and b jets (defined in Section 6.3.4) present in the event.

A first selection with at least four jets and two b-jets is defined as a control region, being only used to check the validity of the description of detector-level distributions and to ensure that the backgrounds are well modelled.

Then the detector-level selection criteria are defined analogously to the fiducial phase spaces to target different processes and observables. They are:

- corresponding to the 5j3b fiducial phase space is the detector-level event selection requiring at least five jets, including at least three b-tagged jets;
- to target the 6j4b fiducial phase space, we define a detector-level selection requiring six jets, including at least four b-tagged jets;
- for the 6j3b3l, we define a detector-level phase space requiring at least six jets, at least three b jets, and at least three jets which are not b-tagged; and

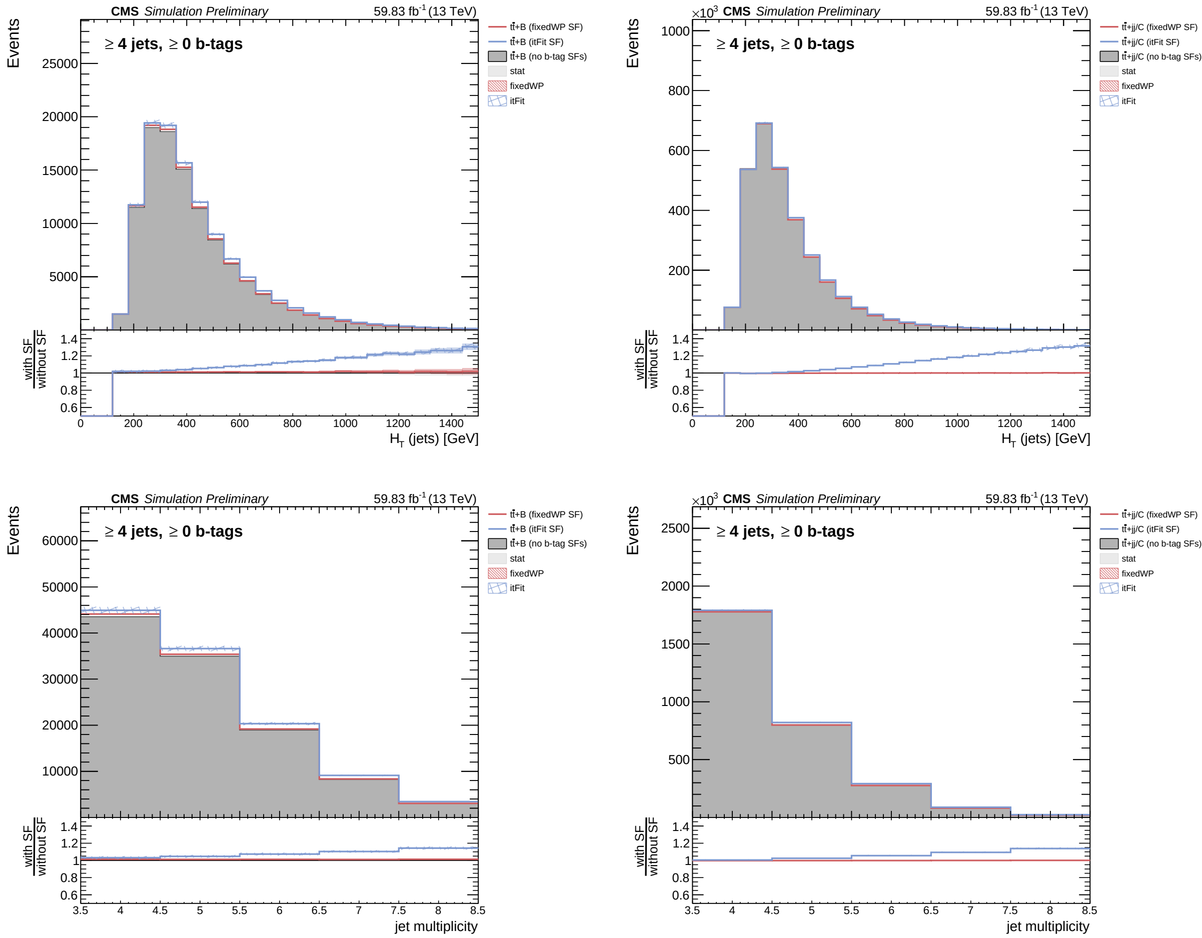

Figure 24: Jet H_{T} (top) and jet multiplicity (bottom) distributions for 2018 data in a ≥ 4 jets phase space. The histogram in grey represents the expected distribution for $t\bar{t}$B events (left) or $t\bar{t}$C $+t\bar{t}j\bar{j}$ events (right). The blue line indicates the adjusted distribution with the itFit b-tagging scale factors which deforms the distribution (which should not be affected by b-tagging). The red line indicated the adjusted distribution with the fixedWP b-tagging scale factors (used in this analysis) which maintain the distribution in its original condition. The panels under each histogram indicate the ratio of the distributions with applied scale factors to the distribution without.

- corresponding to the 7j4b3l phase space is the detector-level selection with at least seven b jets, including at least four b-tagged jets and at least three jets which are not b-tagged.

Given that these detector-level selections are constructed to match the generator-level phase spaces, they are going to be indicated with the same notation. A further specification will be included if there is an ambiguity between the two.

It is important to remember that these selections are not mutually exclusive and, for example the 6j4b selection is fully included in the 5j3b selection since the former *does* have a minimum of five jets and three b jets.

7 $t\bar{t}$B Identification

The properties of the $t\bar{t}$B signal allow for preliminary isolation of this contribution before the fitting. The key factors in creating this distinction are the selections of the number of jets and b jets in the event from which the four primary phase spaces are defined as in Chapter 5.1. It also becomes interesting to investigate b jet tagging properties to provide a further isolation of the signal. This chapter details the modeling of the $t\bar{t}$B signal, the effects of the phase spaces on signal purity, and introduces the use of ancillary variables for the purpose of signal identification.

7.1 Signal Modeling

This analysis makes use of different simulation approaches for the $t\bar{t}b\bar{b}$ signal process. These approaches are distinguished by the combination of different event generators and parton shower simulations but they can be combined into two groups:

Inclusive $t\bar{t}$ + jets simulation: This approach simulates the $t\bar{t}$ pair at NLO precision while events with $t\bar{t}$ +1 jet are simulated at LO precision. The simulation of $g \rightarrow b\bar{b}$ splitting and additional QCD radiation is done via the Pythia [98] parton shower. These simulations are performed by ignoring the b quark mass in the 5 flavor scheme (5FS).

Dedicated $t\bar{t}b\bar{b}$ simulation: This approach simulates the $t\bar{t}b\bar{b}$ events at NLO [59] by using the Powheg-box-res [62, 63, 64, 56, 65, 66, 67] generator with OpenLoops [99]. It is similar to the previous approach in its use of Pythia for hadronization and parton showering but, unlike the inclusive $t\bar{t}$+jets simulation, this approach does not use Pythia for the additional $b\bar{b}$ production. These simulations are performed by taking the b quark mass into account in the 4 flavor scheme (4FS).

The list of generators used in this analysis can be found in Table 6.

Table 6: Generator settings for different modeling approaches.

Process (ME)	Generator	Shower	Flavor Scheme
$t\bar{t}$	Powheg v2	Pythia 8	5FS
$t\bar{t}b\bar{b}$	Powheg-box-res	Pythia 8	4FS
$t\bar{t}b\bar{b}$	Sherpa 2.2.4 [100]	Sherpa [100]	4FS
$t\bar{t}$	Powheg v2	Herwig 7.13 [101]	5FS
$t\bar{t}b\bar{b}$	MadGraph5_amc@NLO [54]	Pythia 8	4FS
$t\bar{t}$ + jets FxFx	MadGraph5_amc@NLO [54]	Pythia 8	4FS

7.2 Jet Multiplicity Effects

The detector selection criteria introduced in Section 6 provide a series of regions targeting measurements in different processes as defined by the fiducial phase space definitions in Section 5.1. This allows for the measurement of the differential cross-section via the unfolding process described later in Section 8.

The plots in Figure 25 and 26 compare jet and b-jet multiplicities and their process breakdowns between a control region with at least two b-jets and one of the signal regions defined in Section 5.1. The plots show that these control regions are enriched with background events such as $t\bar{t}$+light and $t\bar{t}$C while $t\bar{t}$B events are a small proportion overall. This is contrasted with the plots from the signal regions 5j3b and 6j4b where a higher number of jets and b-tagged jets is required, resulting in the signal component being more comparable to the $t\bar{t}$+light component. It is worth noting that the proportion of signal events increases with the number of b-tagged jets, which will be discussed further in Section 7.3.

Table 7 displays $t\bar{t}$B and background yields expected from simulation after the full selection criteria have been applied to the events.

As mentioned in Section 5.4, the $t\bar{t}$B event have been split into *signal* if the events fall within the generator-level fiducial phase space, and $t\bar{t}$B OOA if the events fall out of the acceptance of these regions.

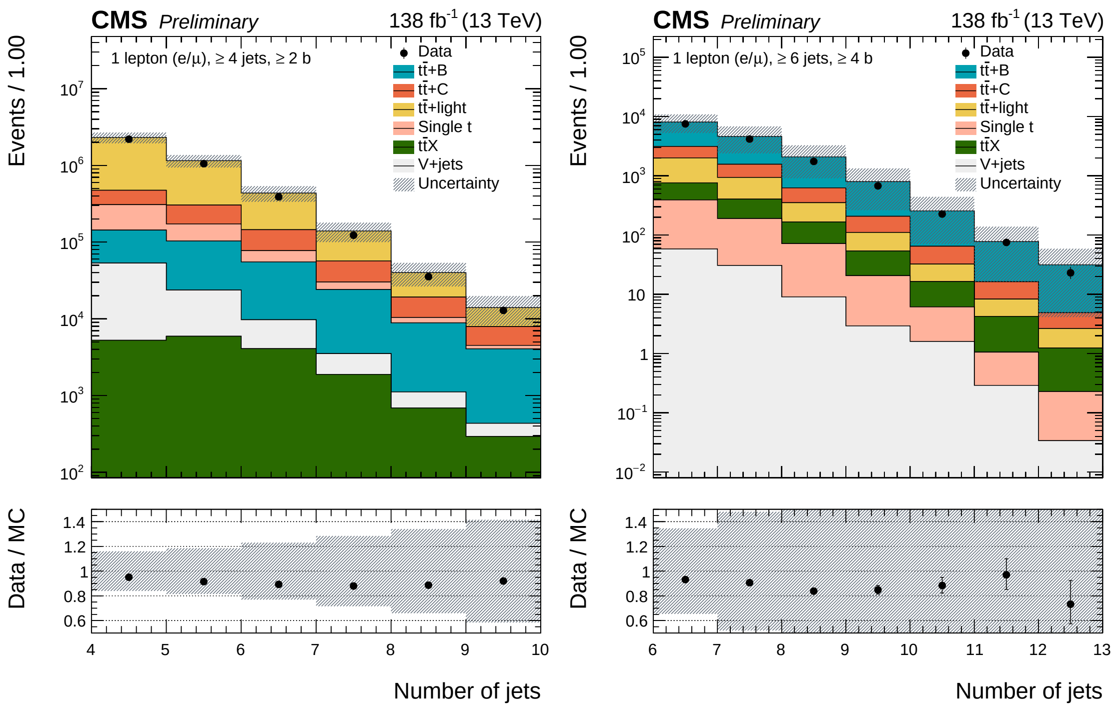

Figure 25: Plots of the jet multiplicity in the control region with at least four jets and at least two b-tagged jets (left) and in the 6j4b signal region (right). The data shown is for all eras combined. The shaded bands include all uncertainties as indicated in Section 9.

Table 7: Expected yields of the signal and background processes for the 5j3b, 6j3b3l, 6j4b, and 7j4b3l detector-level selections. The yields include the datasets from all eras and both muon and electron channels. The $t\bar{t}$B events have been split into *signal* if the events fall within the generator-level fiducial phase space, and $t\bar{t}$B OOA if the events fall out of the acceptance of these regions. Note that the definition of $t\bar{t}$B and $t\bar{t}$B OOA changes based on the phase space being considered. $t\bar{t}$B OOA is split into $t\bar{t}b\bar{b}$ OOA and $t\bar{t}b$ OOA based on the number of additional b-jets present but the two are only treated differently for the 6j4b and 7j4b3l phase spaces. The division is shown in the table for display purposes.

	5j3b	6j3b3l	6j4b	7j4b3l
process				
$\mathrm{t\bar{t}} + B$	67809	28786	6118	2905
$\mathrm{t\bar{t}} + b$ OOA	6570	3457	2701	1244
$\mathrm{t\bar{t}} + bb$ OOA	2114	3863	1126	688
$\mathrm{t\bar{t}} + C$	45430	21890	2101	974
$\mathrm{t\bar{t}}$+light	123213	44247	1978	747
$\mathrm{t\bar{t}V}$	1810	925	207	90
Single t	8985	3225	385	154
$\mathrm{t\bar{t}H}$	2467	1228	517	240
VJets	2531	915	103	42
Total MC	260929	108535	15235	7083
data	254533	103570	14450	6538
Data/MC Ratio	0.98	0.95	0.95	0.92

While in the 5j3b and 6j3b3l phase spaces, $t\bar{t}$+light is the dominant process, there is still a significant proportion of $t\bar{t}$B events (approximately 25% in each phase space). At the same time, the 6j4b and 7j4b3l

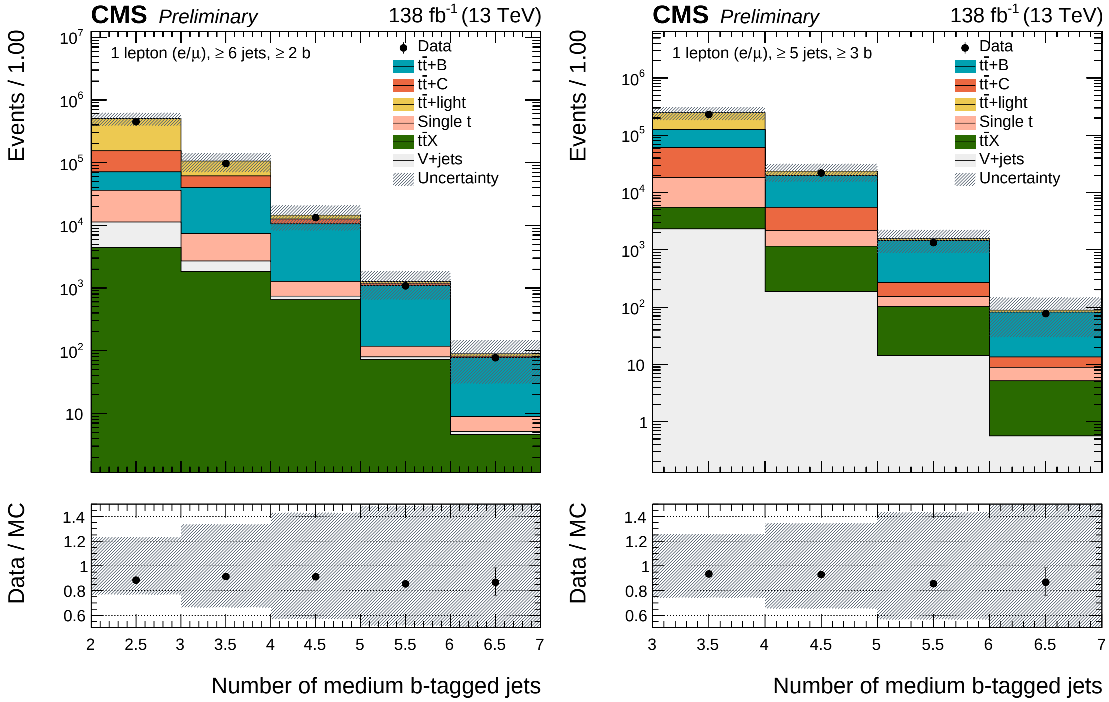

Figure 26: Plots of the medium working point b-tagged multiplicity in a control region with at least six jets and at least two b-tagged jets (left) and in the 5j3b signal region (right). The data shown are for all eras combined. The shaded bands include all uncertainties as indicated in Section 9.

selections have a more significant $t\bar{t}$B enrichment with the signal events as the dominant process, accounting for approximately 40% of events.

7.3 Ancillary Observables

Having noted that the proportion of signal events increases with the number of b-tagged jets, this was identified as a useful parameter to further separate signal and background components by using *ancillary observables*. This allows for the splitting of the detector-level selection into subcategories as dictated by the value of the ancillary observable and, given that the ancillary observable is sensitive to signal, this will produce signal and background enriched subregions for each selection.

The specific ancillary variable chosen to describe the increase in b-tagged jets is the number of b jets which pass the `tight` b-tag working point; its distribution in the 5j3b and 6j4b selections can be seen in Figure 27. Note that this means that, for example, in the 5j3b selection at least three b-tagged jets are required but this could be medium or tight tagging, this allows for events within the 5j3b phase space to have any number of *tight* tagged jets, even below three. In any case, since the signal events contain either three or four particle-level b jets and the background events typically have fewer, the region with most tight-tagged b jets will be signal enriched while the region with the fewest tight-tagged b jets will be background enriched and aid in background modelling. This information is used in the unfolding process according to the description in Section 8.

As mentioned above, ancillary variables are used as a further dimension during unfolding to better separate signal and background-enriched regions.

The most favorable choice to study $t\bar{t}b\bar{b}$ is the number of b-tagged jets in an event. In particular, $t\bar{t}b\bar{b}$ processes have four particle-level b-tagged jets while background events have fewer such as $t\bar{t}b$ processes with three b-tagged jets and $t\bar{t}$C and $t\bar{t}j\bar{j}$ with two b-tagged jets. However, this is not always reflected at the detector level because of the tagging inefficiency and the mis-tagging rate connected to the medium b-tagging

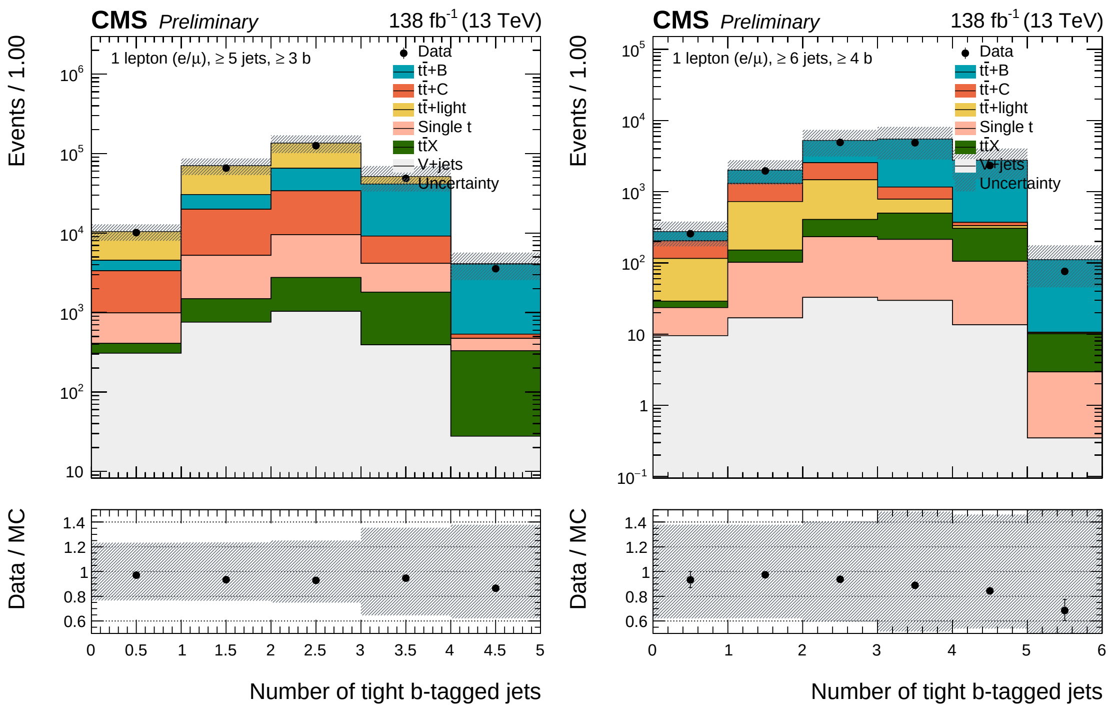

Figure 27: Number of tight-tagged b-tagged jets in the 5j3b signal region (left) and in the 6j4b signal region (right). The data shown is for the datasets of all eras combined. The shaded bands include all uncertainties as indicated in Section 9.

working point used to determine the signal phase space (amounting to 1% as described in Section 6.4). This can cause light jets to be mis-tagged as b jets and allow for background events to fall within signal phase spaces. But this mis-identification effect can be mitigated by also using the tight b-tagging working point which only has a mis-tagging rate of 0.1% and can better separate the background processes; in particular $t\bar{t}$C and $t\bar{t}j\bar{j}$ which only have two 'true' b-jets and are unlikely to have two extra light jets be mis-tagged as b jets. Two ancillary regions were chosen for 6j4b and 7j4b3l while three for 5j3b and 6j3b3l to allow for good discrimination while maintaining a statistically significant number of events in each bin. In the 6j4b and 7j4b3l case, one bin was used for the case of less than three tight-tagged b jets and the second bin for events with at least three tight-tagged b jets. In the 5j3b and 6j3b3l case, the first bin contained events with zero or one tight-tagged b jets, the second bin for events with exactly two tight-tagged b jets, and the third bin containing events with at least three tight-tagged b jets.

8 Unfolding Strategy

The process of *unfolding* aims to correct for the effects of the detector on data. This is because the way in which the detector is constructed and processes data can distort the data compared to the true distribution. This process is advantageous because its results are rendered independent of the detector which allows them to be easily compared with theoretical calculations, Monte Carlo simulations, and results from other detectors (provided that they also have undergone unfolding). A diagram summarizing this process is depicted in Figure 28

To perform the unfolding, a model linking particle-level to detector-level values of observables is constructed and a *maximum likelihood fit* is performed.

The process of maximum likelihood estimation serves to determine the value of a series of parameters such that they maximise the likelihood of the model describing the observed data. This is achieved by varying the parameters within the range allowed by the model with the goal of minimizing a likelihood function (Equation 13). This function indicates the likelihood that the observed data would be measured given a certain value of the parameters in the statistical model being considered. This differs from the probability because likelihood refers to how well the given data matches a certain model (with the chosen parameter settings) while the probability refers to the chance that a certain dataset is produced by a given model. Note that the parameters used are both related to the total and differential cross-sections (parameters of interest (POI)) and the systematic uncertainties that are being considered for the measurement (nuisance parameters).

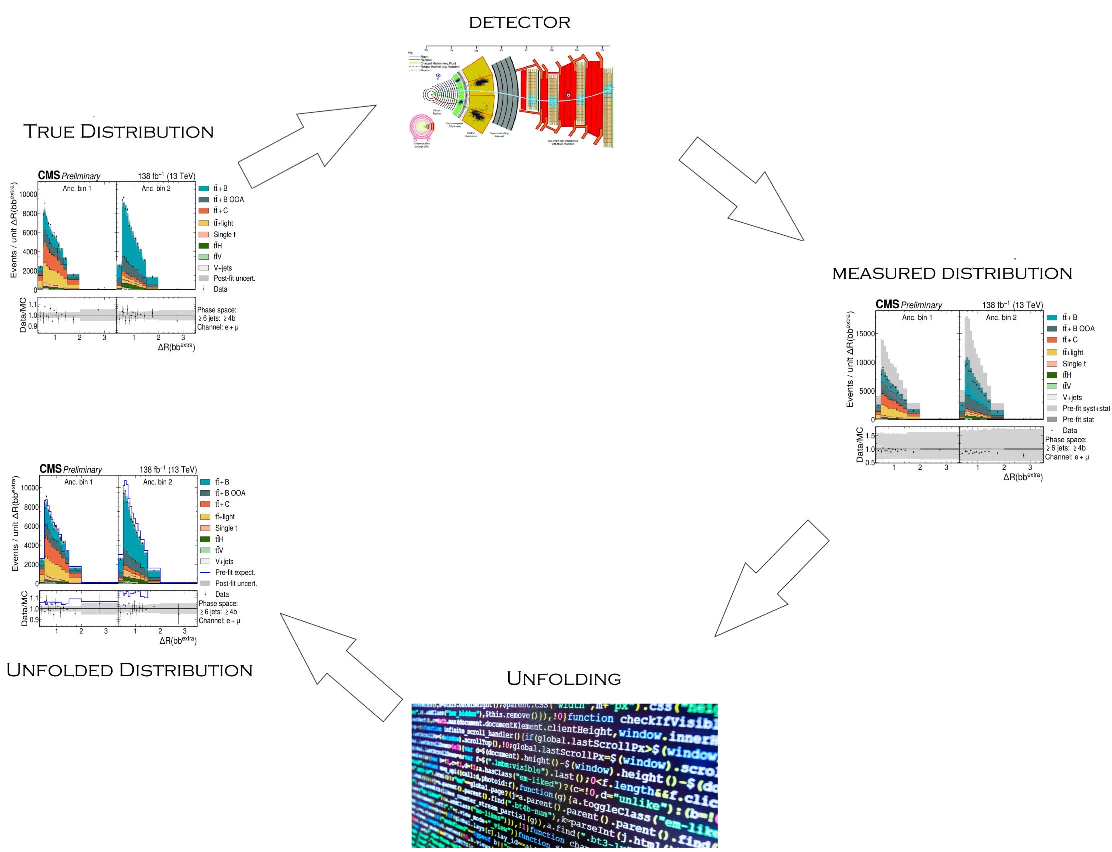

Figure 28: Diagram showing the process of unfolding.

The model used for unfolding is obtained by taking the simulated samples used in the analysis and putting them through a simulation of the detector's behavior. This allows for a comparison between the generated observable values and the values observed after the distortion of the detector. At this point, the maximum likelihood fit is performed by obtaining the maximum likelihood values for the parameters of interest and the nuisance parameters which represent the systematic uncertainties. The fit then outputs a central value for each of these parameters together with their confidence intervals.

The process is repeated in the same way for all the observables considered in the analysis within their respective phase spaces as described in Section 5.1. The information is then organized in such a way as to obtain a normalized differential cross-section for each observable and an inclusive cross-section which is given for each phase space separately. The normalized cross-section is obtained by performing a separate fit where the parameters of interest being used are the fractions of each observable bin rather than the nominal value of the bins. This will be discussed in detail in Section 8.1.2.

8.1 Fit Setup

The fit is performed by using simulation to connect the detector-level reconstructed observables with the generator-level differential cross-sections. The expected contribution of events from a certain generator-level bin being reconstructed to a certain reco-level histogram is derived from the nominal simulation i.e. the POWHEG+OPENLOOPS NLO $t\bar{t}b\bar{b}$ 4FS sample. This contribution is modified based on the systematic uncertainties considered. The choice of nominal $t\bar{t}b\bar{b}$ simulation sample to describe the translation of generator-level to detector-level quantities is well justified and will be discussed in Section 8.3.3. A freely-floating parameter of interest is then assigned to each generator-level bin for the fit.

Besides signal, background processes are also included in the model and modify the number of events expected to be present in each reco-level bin. Unlike the signal, these contributions are not assigned to a free-floating POI but are determined according to the expectations of the simulation samples. Each background component is determined individually to allow for a separate variation within its own uncertainties, this is described further in Section 9.

It's worth remembering at this point, that a fraction of detector-level $t\bar{t}b\bar{b}$ events does not fall within the fiducial phase space defined in Section 5.1 and are identified as background while being simulated as signal. These "out of acceptance" (OOA) events present an ambiguity as to their treatment because they are part of the $t\bar{t}b\bar{b}$ process that is being measured but, since they fall out of the fiducial phase space, they cannot be properly measured. Given this behavior, the OOA $t\bar{t}b\bar{b}$ events are treated as a background with variation allowed within the theoretical systematic uncertainites of the nominal $t\bar{t}b\bar{b}$ simulation.

The fit is run with separate histograms being used for the muon and electron channels. A similar procedure is also observed for the four data-taking eras considered (2016preVFP, 2016postVFP[1], 2017, and 2018) which each have a separate histogram for the fit. The separation of eras can lead to a certain variation in the relationship between generator-level and reco-level quantities because the different detector and beam conditions of the time are kept into account. All these separate histograms are then fit simultaneously to obtain the final result.

The likelihood function used to measure the unfolded distributions is the following:

$$L(\vec{\mu}, \vec{\alpha}) = \left[\prod_{e,i} \mathrm{Poi} \left(D_{e,i} \middle| \sum_j \mu_j M^e_{ij}(\vec{\alpha}) + \sum_{p \in \mathrm{bkg.}} N^p_{e,i}(\vec{\alpha}) \right) \right] \mathcal{N}(\vec{A}|\vec{\alpha}, \mathbf{\Sigma}^{\alpha}), \tag{13}$$

where:

- The parameters $\vec{\mu}$ are free-floating parameters of interest.
- The parameters $\vec{\alpha}$ are nuisance parameters used modelling the systematic uncertainties.
- $D_{e,i}$ are the observed yields in data in data-taking era e and reco-level bin i (channels are treated as bins).

[1]The two 2016 eras are distinguished by the application of a Preamplifier Feedback Voltage Bias (VFP) to correct a saturation in the front end electronics [102]

- M^e_{ij} are the expected yields in era e and reco-level bin i, and generator-level bin j, obtained using the nominal simulation of the $t\bar{t}b\bar{b}$ signal. These will be referred to as *migration matrices*, and will be discussed in more detail in Section 8.1.1.

- $N^p_{e,i}$ are the expected yields of background process p in era e and reco-level bin i.

- $\mathrm{Poi}(d|\nu)$ is the Poisson probability mass function for a number of counts d with mean ν.

- $\mathcal{N}(\vec{A}|\vec{\alpha}, \mathbf{\Sigma}^\alpha)$ is the constraint term of the nuisance parameters. It is approximated as the probability density of a multivariate normal distribution with mean $\vec{\alpha}$ and covariance matrix $\mathbf{\Sigma}^\alpha$ (although, in practice, $\mathbf{\Sigma}^\alpha = \mathbf{1}$ is used). $\vec{A}$ are auxiliary observables (not to be confused with the ancillary observables introduced in Section 7.3) associated with the nuisance parameters, introduced to treat the nuisance parameters with a consistent frequentist treatment. Those auxiliary observables are only relevant for the generation of frequentist toys (see Sec. 8.3.2); in all other cases they are fixed to $\vec{A} = \vec{0}$.

The Negative-Log-Likelihood (NLL) referred to in the following sections is defined from the above as: $\mathrm{NLL} = -\log(L)$. The *statistical model* will be represented as $L(\vec{D}, \vec{A}|\vec{\mu}, \vec{\alpha})$ and can either be interpreted as a probability distribution from which to sample $\vec{D}$ and $\vec{A}$ given fixed parameters $\vec{\mu}$ and $\vec{\alpha}$ or as a likelihood with floating $\vec{\mu}$ and $\vec{\alpha}$ and fixed $\vec{D}$ and $\vec{A}$.

The best-fit parameters $\hat{\mu}_j$ and $\hat{\alpha}_j$ can be obtained in this method either by maximising the likelihood or by minimizing the NLL. These results can then be used to derive the measured cross-sections for a given bin j by calculating $\hat{\sigma}_j = \hat{\mu}_j \sigma^0_j$ where $\hat{\mu}_j$ are the best-fit values for the parameters of interest and σ^0_j is the cross-section in the generator-level bin j as predicted by the nominal simulation. These values can then be reinterpreted as differential cross sections by dividing the cross-section in generator-level bin j by the width of that bin:

$$\frac{\mathrm{d}\hat{\sigma}_j}{\mathrm{d}X} = \frac{\hat{\mu}_j \sigma^0_j}{w_j}. \tag{14}$$

The binning used varies between generator level and reco level where the latter is chosen to be finer than the former to avoid biases, improve signal and background separation, and avoid the need for regularization that comes with a large variation between bins due to low statistics. In particular, each of the reco-level bins are chosen to be about half the width of the generator-level bins. This treatment has the advantage of providing more information to the fit by increasing granularity at reco level while avoiding large fluctuations that may require regularization by not increasing the number of generator-level bins.

As discussed in Section 7.3, the addition of an ancillary variable is a useful tool that provides more information to the fit and is used in unfolding. This ancillary variable is treated as an extra axis in the fit as, for example, during the fit of $\Delta \mathrm{R}_{bb^{\mathrm{extra}}}$, the reco-level histogram that is being provided is not a one-dimensional histogram but two-dimensional, combining the $\Delta \mathrm{R}_{bb^{\mathrm{extra}}}$ information with that of the ancillary variable. This allows for a reduction in uncertainty by discriminating between signal and background thanks to the signal and background enriched regions that the ancillary variable provides. The usage of ancillary variables in unfolding is described in more detail in Section 8.2.

An attempt was made to improve upon the ancillary variables by the addition of further control regions into the fit to better separate events with $t\bar{t}$ and light jets which are the main background of the analysis.

However, upon investigation, it was found that these control regions did not significantly improve the expected sensitivity beyond what can be obtained with the ancillary variables alone. For this reason, it was decided to not include this additional control regions in the fit.

Most of the systematic uncertainties considered that relate to the detector modify both signal and backgrounds in a correlated manner but this is not necessarily the case across eras and depends on the uncertainty in question. Theoretical uncertainties, on the other hand, are always correlated between eras but not necessarily between processes. The treatment and behavior of the systematic uncertainties will be discussed in more detail in Section 9.

8.1.1 Migration Matrices and Ill-posedness Checks

Migration matrices display the relation between generator-level and reco-level observables based on acquisition effects. They are two-dimensional histograms whose contents are determined based on the $t\bar{t}b\bar{b}$ signal samples being used. The use of ancillary variables adds a further dimension to these histograms, making them 3d histograms but, for technical and visual purposes, they are "unrolled" into two-dimensional histograms where the observables of each ancillary region are concatenated. Notation-wise, the event yield for each bin of the migration matrix is written as M^e_{ij} where it denotes the expected number of $t\bar{t}b\bar{b}$ events present in the i reco-level bin and j generator-level bin for the era e. Note that, due to the "unrolling" performed on the migration matrix, the index i goes over the different reco bins associated with the different ancillary regions, a similar behavior is present for the e and μ channels. This results in a total of:

$$(4 \text{ eras}) \times (2 \text{ channels}) \times (2-3 \text{ anc. regions}) \times (2 \text{ bins}) = 32-48 \text{ reco-level bins.} \tag{15}$$

for each generator-level bin.

This information can then be used to calculate the total expected signal yields for a given reco-level bin i and era e as:

$$N^e_i(\vec{\mu}) = \sum_j \mu_j M^e_{ij}, \tag{16}$$

with μ_j being the fit POI that scales generator-level bin j

In the context of unfolding, it is useful to consider the probability K_{ij} that an event originating in the generator-level bin j be selected and reconstructed in the reco-level bin i; this probability also varies based on the era e being considered. With this probability, it is possible to obtain the expected event yields as:

$$M^e_{ij} = \mathcal{L}_e \sigma^0_j K^e_{ij}, \tag{17}$$

where $\mathcal{L}_e$ is the integrated luminosity for the chosen era e.

This process is performed separately for each era and channel but the results are summed into a single migration matrix for the purposes of visualization. This results in a two-dimensional migration matrix with one axis containing information on the generator-level bins and the other containing information on the reco-level bins and ancillary variables:

$$\hat{M}_{i'j} = \sum_e M^e_{i'j}, \tag{18}$$

where the detector-level index i' indicates that the e and μ channels have also been summed.

Having performed these summations, a final transformation is performed by normalizing the migration matrices column by column:

$$T_{i'j} = \frac{\hat{M}_{i'j}}{\sum_{i'} \hat{M}_{i'j}} = \frac{\sum_e M^e_{i'j}}{\sum_{e,i'} M^e_{i'j}} = \frac{\sum_e \mathcal{L}_e K^e_{i'j}}{\sum_{e,i'} \mathcal{L}_e K^e_{i'j}}. \tag{19}$$

where $T_{i'j}$ is the content of the $(i';j)$ bin of the migration-matrix bin that is plotted. An example of this can be seen in Figure 29 where two migration matrices of different observables are presented both in the case with and that without ancillary variables being displayed. From these plots, it is possible to see that the migration matrices are strongly diagonal which shows a good matching between the generator-level and reco-level observables and their definitions.

To determine the effectiveness and performance of the correspondence in the migration matrix, it is useful to define quantities such as selection efficiency and signal-to-background purity.

The selection efficiency is defined as the probability that a signal event from a certain generator-level bin j be reconstructed and selected without taking into account the reco-level bin in which it is reconstructed. This efficiency will be 100% if every signal event can be selected and reconstructed. For each era, the efficiency calculation can be written as:

$$\epsilon^e_j = \sum_i K^e_{ij}. \tag{20}$$

This information can then be used to calculate the efficiency averaged by era ϵ_j as:

$$\epsilon_j = \frac{\sum_e \mathcal{L}_e \epsilon^e_j}{\sum_e \mathcal{L}_e} = \frac{\sum_{ei} M^e_{ij}}{\nu_j}, \tag{21}$$

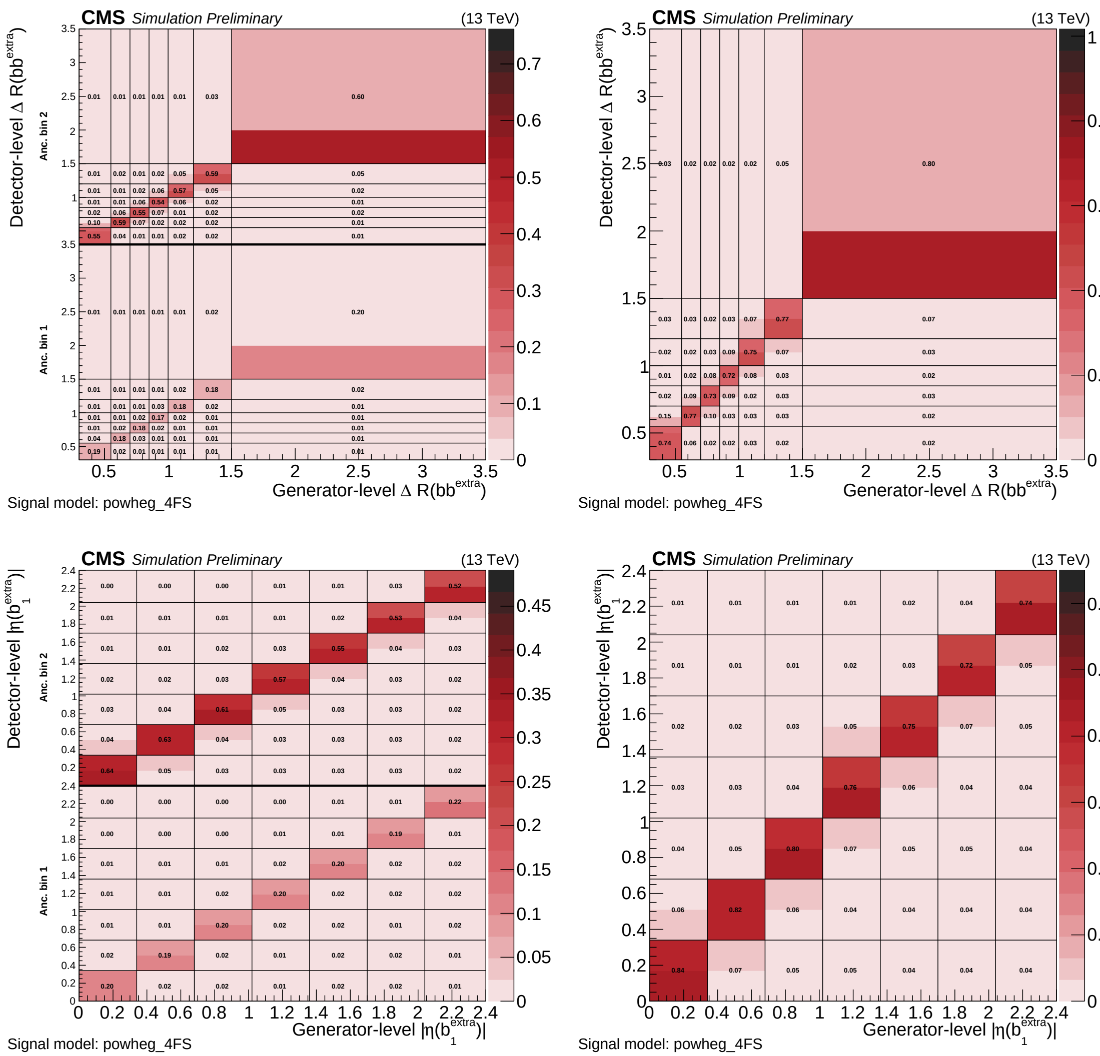

Figure 29: Migration matrices for $\Delta R_{bb^{\text{extra}}}$ (top) and for $|\eta(b_1^{\text{extra}})|$ (bottom), in the 6j4b phase space, contents defined as in Equation (19). The x axes indicate the generator-level bins of the observables (corresponding to the j index) while the y axes indicate the reco-level bins of the observables (corresponding to the i' index). In the plots on the left, the ancillary variable is being used and is unrolled onto the y axis resulting in the reco-level binning being repeated twice (once per ancillary region of the 6j4b phase space). The plots on the right, on the other hand, sum the components of the different ancillary variables to give a more general idea of the overall relation between generator-level and reco-level observables. The color in each bin is split in two to indicate the finer binning present at reco level where each bin has half the width of the corresponding generator-level bin. The numbers written in the bins instead refer to the values that would be obtained if the generator and reco-level binning were the same.

where $\nu_j = \sigma_j^0 \sum_e \mathcal{L}_e$ is the total expected yield at generator-level in bin j for all eras. An example of this efficiency in a selection of observables is shown in Figure 30. The efficiency was not shown to change significantly when comparing the Powheg simulations between the inclusive 5FS and exclusive 4FS, strengthening the validity of using the 4FS sample as nominal signal sample. These two types of samples are distinguished by their treatment of the b quark mass in simulation. The 4FS samples include the b mass and calculate the additional b-jets in the matrix elements. The 5FS samples instead treat the b quarks as massless and the additional b-jet radiation is mostly generated in the parton shower.

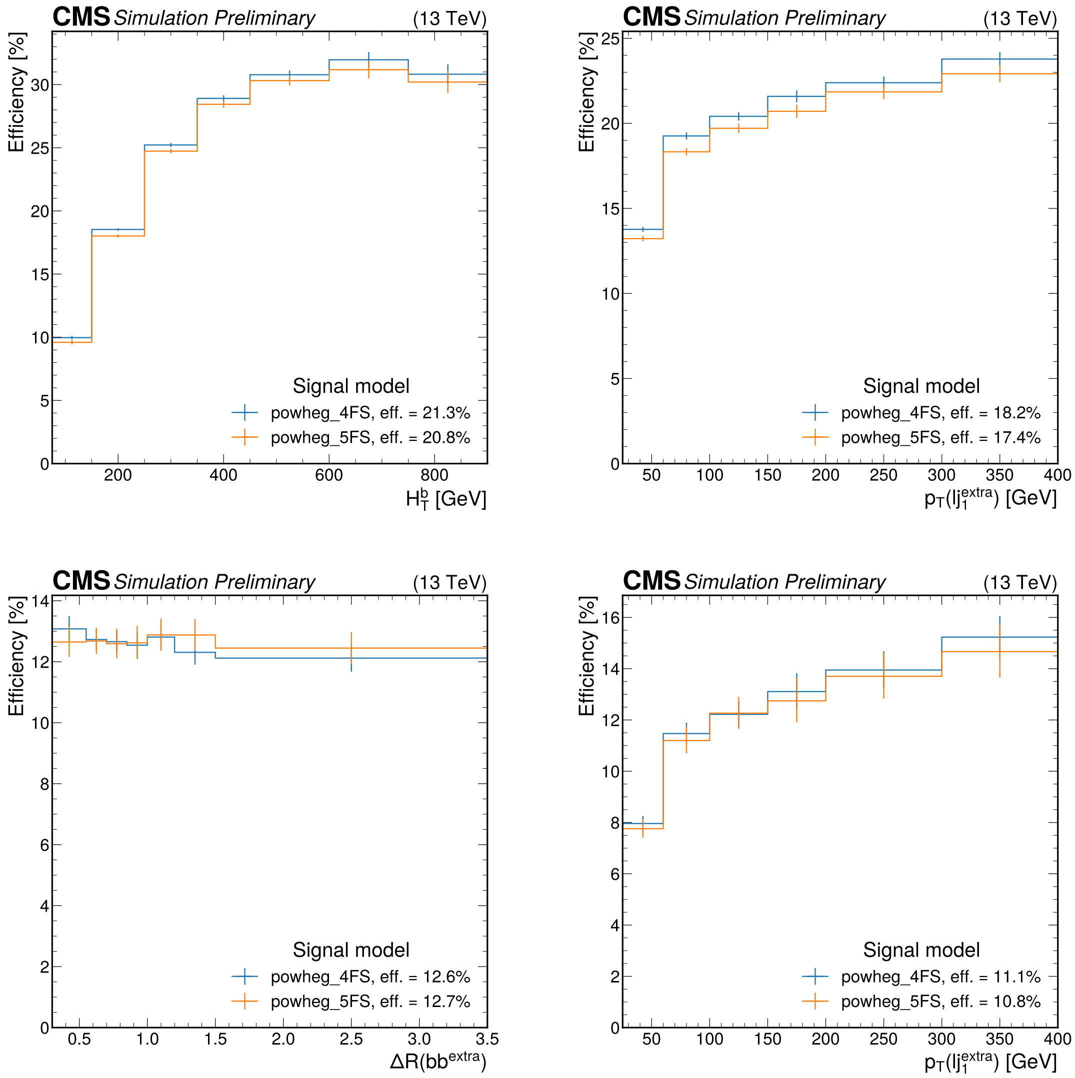

Figure 30: Selection efficiencies for different generator-level observables with an average across e and μ channels and eras. The efficiencies are calculated following Equation (21) and only statistical uncertainties are displayed. The observables presented are H_T^b in the 5j3b phase space (top left), $p_T(\mathrm{lj}_1^{\mathrm{extra}})$ in the 6j3b3l phase space (top right), $\Delta\mathrm{R}_{bb^{\mathrm{extra}}}$ in the 6j4b phase space (bottom left), and $p_T(\mathrm{lj}_1^{\mathrm{extra}})$ in the 7j4b3l phase space (bottom right).

While the purity of the migration matrix cannot be calculated in the case of non-square migration matrices, it is possible to calculate the signal purity which represents the signal-to-background ratio for the reco-level observables. The purity was calculated in three different ways to highlight the behavior of three different components: the signal $t\bar{t}$B events passing the fiducial phase-space definition ("S"), the OOA component of the $t\bar{t}$B events not passing the fiducial cuts ("OOA"), and the rest of the background processes ("BKG"). The three different purities were:

- $(S + OOA)/(S + OOA + BKG)$ describing the overall number of signal events over the sum of all events without considering the effect of fiducial cuts on the $t\bar{t}$B component.
- $S/(S + OOA + BKG)$ which indicates the number of signal events passing the fiducial cuts over the sum of all events.

- $S/(S + OOA)$ describing the fraction of $t\bar{t}$B events that pass the fiducial cuts.

Since the purities do not vary significantly across eras and e/μ channels, the values shown in Figure 31 for some example observables are averaged across these different sections. However, given that there is a notable difference between ancillary regions (as is their role), these are shown separately to display their power to obtain signal-enriched and background-enriched regions.

For the purpose of investigating the effect of different nominal samples, the purity for the inclusive 5FS simulations was compared to the exclusive 4FS simulations. The purity plot shows a good correspondence in the fraction of $t\bar{t}$B events passing the fiducial cuts especially in the 5j3b phase space but varies in the 6j4b phase space which can be understood as the two models predict different b-jet multiplicities.

Greater differences can be observed in the signal over background distributions (in both their expressions) but this is due to the different predicted cross-section between the models where the 4FS signal model has a higher cross-section which results in a higher purity when compared to the background. The opposite effect is present for the 5FS signal model which yields a lower cross-section.

With regards to the OOA contribution, its impact is minimal in the 5j3b phase space where comparatively few fiducial requirements are needed but its magnitude becomes comparable to the signal in the 6j4b phase space whose requirements are more stringent. The events that do not satisfy the fiducial requirements generally do so because of b-jet mis-tagging, i.e. when one of the "additional" b jets falls out of acceptance but an external c jet is mis-tagged as a b jet. This can be noted by comparing the $S/(S+OOA)$ information in the first and second ancillary regions where, when more stringent b-tagging requirements are requested in the second ancillary region, the purity increases significantly.

While the above quantities describe the effect the migration matrix has on the data and its effectiveness, they do not account for the migration matrix's performance in the fit or whether it would result in an ill-defined inversion problem. This can be studied by computing the *condition number* (CN) of the migration matrix which is obtained via the single-value decomposition of the migration matrix. The decomposition provides the singular values σ_k which is used to derive the CN as $\max(\sigma_k)/\min(\sigma_k)$. The desired value of CN is usually a small number because a large one indicates that changes in the input (generator-level distribution) cause only small changes in the output (reco-level distribution). A large CN is problematic because during the fit small variations in the reco-level distribution can cause large changes in the derived generator-level distribution; this indicates that the inversion problem is ill-defined.

The magnitude of the CN is dependant on what is being used as a "migration matrix", whether it be M^e_{ij} or K^e_{ij} as previously defined. However, this choice should not affect the overall well or ill-posedness decision if considered within the appropriate frame. The following section uses CN values calculated from the M^e_{ij} migration matrix where it has been computed either with or without the ancillary variables.

The CN for all observables considered is displayed in Table 8 with the comparison between the computation with and without ancillary variables. By observing these two options, it can be determined that the ancillary variables do not have a large effect on the CN, indicating that the variable resolution does not change significantly across different ancillary regions. Furthermore, the CN are small ($\lesssim 10$) for almost all variables which indicates that the inversion problem is well-posed and the unfolding can be performed without need for regularization.

8.1.2 Absolute and Normalized Differential Cross Sections

Following the fits in Section 8.1, it is possible to use the best-fit parameters $\hat{\mu}_j$ (corresponding to the POI μ_j) to derive the absolute differential cross section for the observable X being considered. This is done by using the width of each bin w_j in the relation $\mathrm{d}\hat{\sigma}_j/\mathrm{d}X = \hat{\mu}_j\sigma^0_j/w_j$ which provides the differential cross-section for observable X in bin j. It is then possible to calculate the total fiducial cross-section in a given phase space as:

$$\hat{\sigma}_{\text{tot}} = \sum_j \hat{\sigma}_j. \tag{22}$$

After the central value of the cross-section has been obtained, confidence intervals are obtained by using a profiling procedure where the upper and lower bounds are calculated for each bin $k \neq j$ with the profiling of other parameters and nuisance parameters. This results in a $\hat{\mu}^{\pm}_k$ that satisfies:

$$\text{NLL}\left(\hat{\hat{\mu}}_1(\hat{\mu}^{\pm}_k), \cdots, \hat{\mu}^{\pm}_k, \cdots, \hat{\hat{\mu}}_n(\hat{\mu}^{\pm}_k), \hat{\hat{\alpha}}(\hat{\mu}^{\pm}_k)\right) = \text{NLL}_0 + \delta_{\text{NLL}}, \tag{23}$$

Table 8: CN for all the observables studied in the four fiducial phase spaces, calculated with and without the use of ancillary variables. The CN have been calculated based on the M^{e}_{ij} migration matrices.

Phase space	Observable	With ancillary	No ancillary
5j3b	N_{jets}	16.7	16.9
5j3b	N_{b}^{M}	5.0	6.4
5j3b	$H_{\mathrm{T}}^{\mathrm{j}}$	3.5	3.5
5j3b	$H_{\mathrm{T}}^{\mathrm{b}}$	27.9	5.7
5j3b	$\|\eta(\mathrm{b}_3)\|$	4.3	4.2
5j3b	$p_{\mathrm{T}}(\mathrm{b}_3)$	101.8	116.4
6j4b	N_{jets}	5.7	5.7
6j4b	$H_{\mathrm{T}}^{\mathrm{j}}$	5.2	5.3
6j4b	$H_{\mathrm{T}}^{\mathrm{b}}$	8.6	6.7
6j4b	$\|\eta(\mathrm{b}_3)\|$	6.1	6.1
6j4b	$p_{\mathrm{T}}(\mathrm{b}_3)$	28.4	28.4
6j4b	$\|\eta(\mathrm{b}_4)\|$	4.3	4.2
6j4b	$p_{\mathrm{T}}(\mathrm{b}_4)$	32.5	34.1
6j4b	$\|\eta(\mathrm{b}_1^{\mathrm{extra}})\|$	7.7	7.5
6j4b	$p_{\mathrm{T}}(\mathrm{b}_1^{\mathrm{extra}})$	7.9	7.9
6j4b	$\|\eta(\mathrm{b}_2^{\mathrm{extra}})\|$	6.0	5.9
6j4b	$p_{\mathrm{T}}(\mathrm{b}_2^{\mathrm{extra}})$	11.6	12.0
6j4b	$\mathrm{m}(\mathrm{bb}^{\mathrm{extra}})$	7.0	7.1
6j4b	$p_{\mathrm{T}}(\mathrm{bb}^{\mathrm{extra}})$	5.0	5.0
6j4b	$\|\eta\|(\mathrm{bb}^{\mathrm{extra}})$	6.6	6.5
6j4b	$\Delta\mathrm{R}(\mathrm{bb}^{\mathrm{extra}})$	2.0	2.0
6j4b	$\Delta\mathrm{R}_{\mathrm{bb}}^{\mathrm{avg}}$	6.8	6.9
6j4b	$\mathrm{m}_{\mathrm{bb}}^{\mathrm{max}}$	4.5	4.6
6j3b3l	$\|\Delta\phi(\mathrm{lj}_1^{\mathrm{extra}}, \mathrm{b}_{\mathrm{soft}})\|$	2.8	2.9
6j3b3l	$p_{\mathrm{T}}(\mathrm{lj}_1^{\mathrm{extra}})$	4.9	4.9
6j3b3l	$H_{\mathrm{T}}^{\mathrm{light}}$	7.5	5.2
7j4b3l	$\|\Delta\phi(\mathrm{lj}_1^{\mathrm{extra}}, \mathrm{b}_{\mathrm{soft}})\|$	2.7	2.7
7j4b3l	$p_{\mathrm{T}}(\mathrm{lj}_1^{\mathrm{extra}})$	4.5	4.6
7j4b3l	$H_{\mathrm{T}}^{\mathrm{light}}$	6.0	4.5

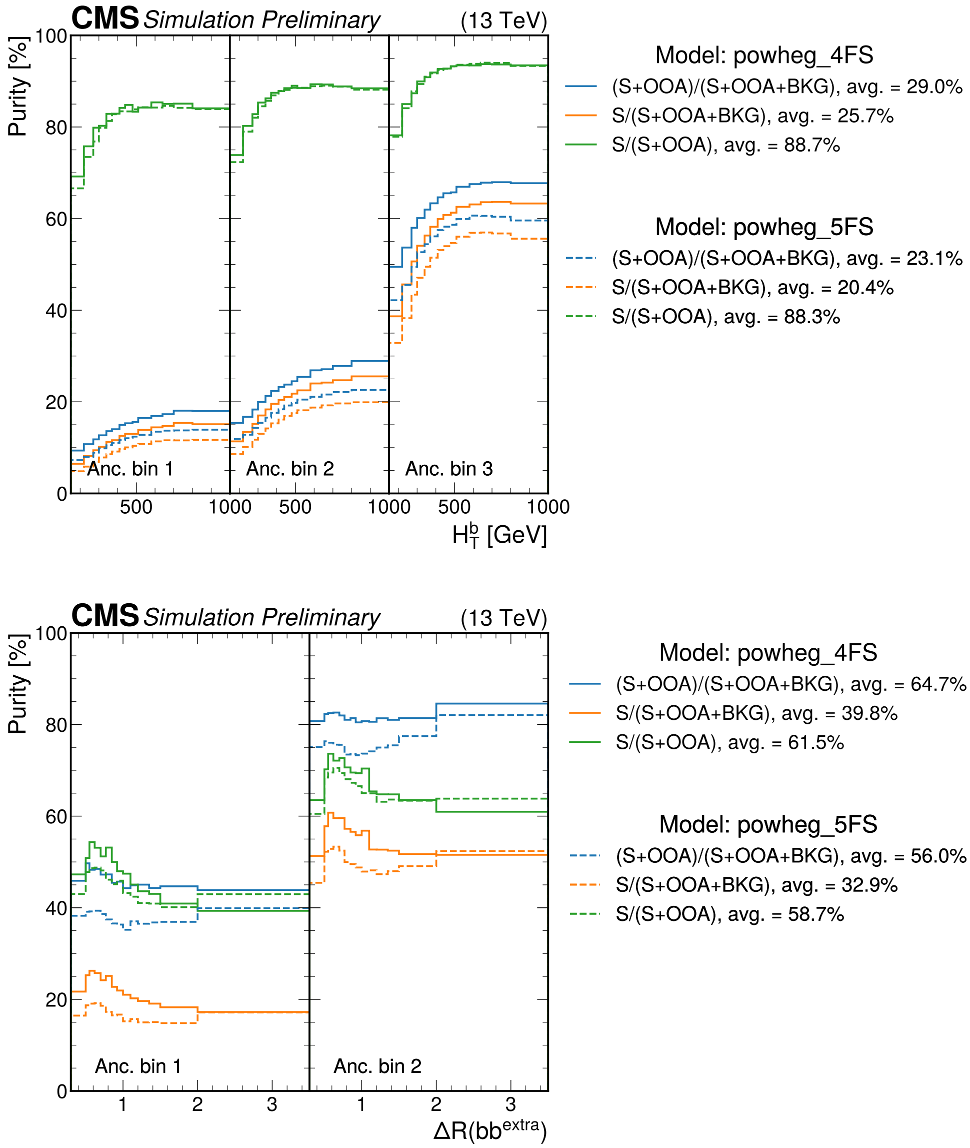

Figure 31: Signal-to-background purity of H_{T}^{b} in the 5j3b phase space (top) and $\Delta\mathrm{R}_{bb^{\mathrm{extra}}}$ in the 6j4b phase space (bottom) with three different methods of calculation. Each of the observables is split into its ancillary regions. The dashed lines represent the data corresponding to a 5FS signal model while the solid line represents the data corresponding to a 4FS signal model (nominal case).

where:

- $\hat{\hat{\mu}}(\hat{\mu}_k^{\pm})$ is the profiled value of μ, corresponding to the value of μ that minimizes $\mathrm{NLL}(\mu,\theta)$ while applying $\theta = \hat{\mu}_k^{\pm}$ as constraint,
- $\mathrm{NLL}_0 = \mathrm{NLL}(\hat{\vec{\mu}}, \hat{\vec{\alpha}})$ is the best-fit (minimum) value of the NLL,
- and $\delta_{\mathrm{NLL}} = 1/2$ to define the intervals at 68% confidence level (CL).

If the number of samples being considered is large, it is also possible to obtain the confidence intervals from the covariance matrix between the parameters being fitted $\hat{\boldsymbol{\Sigma}}^{\mu}$. This matrix can be obtained as the inverse of the Hessian matrix of the NLL taken in its minimum. It is then possible to obtain the confidence intervals for each POI (μ_j) as $\hat{\sigma}_j \pm \sqrt{\hat{\boldsymbol{\Sigma}}^{\mu}_{jj}}$, also known as "normal intervals". This can also be used for the total fiducial cross section whose variance $\hat{V}_{\sigma_{\text{tot}}}$ can be calculated as:

$$\hat{V}_{\sigma_{\text{tot}}} = \sum_{i,j} \sigma_i^0 \hat{\boldsymbol{\Sigma}}^{\mu}_{ij} \sigma_j^0. \tag{24}$$

This result can be used to obtain the confidence interval of the total cross-section under the assumption of a Gaussian distribution as $\hat{\sigma}_{\text{tot}} \pm \sqrt{\hat{V}_{\sigma_{\text{tot}}}}$. By performing some comparisons between the normal intervals and these obtained through the profiling procedure, the difference between the two methods was seen to be very small. Based on this observation, the normal intervals were chosen as the default method of calculation and will be the ones reported to avoid the computationally expensive profiling method.

Having obtained the absolute differential cross-section and the total cross-section, it possible to calculate the normalized differential cross-section as $1/\hat{\sigma}_{\text{tot}} \cdot \mathrm{d}\hat{\sigma}_j/\mathrm{d}X$. However, standard error propagation in this case is not a sufficient treatment with regards to the uncertainties, particularly if the uncertainty of the $\hat{\sigma}_{\text{tot}}$ is very high. This case would fall outside the linear approximation and cause the final uncertainties to be significantly lower. Furthermore, this treatment would neglect the correlations induced between POIs by the normalization conditions. This issue calls for an alternative method of obtaining the normalized differential cross sections. This can be done through a separate fit rather than the scaling of each bin as just shown. This separate fit uses one parameter θ_{tot} to scale the total fiducial cross section and $n-1$ parameters θ_j that scale the fractions of events within the first $n-1$ bins of the given observable. The last bin is not included in the fit because its value derives from the normalization conditions and the values of the $n-1$ other bins. This results in the first $1 \leq j < n$ generator-level bins being scaled by $\theta_{\text{tot}}\theta_j$ while the final bin n is scaled by $\theta_{\text{tot}}\theta_n(\theta_1 \ldots \theta_{n-1})$ with

$$\theta_n(\theta_1 \ldots \theta_{n-1}) \equiv \frac{1}{F_n}\left(1 - \sum_{i=1}^{n-1} \theta_i F_i\right). \tag{25}$$

where $F_j = \sigma_j^0/\sigma_{\text{tot}}^0 = \sigma_j^0/\sum_i \sigma_i^0$ is the pre-fit fraction of events within bin j.

This process allows for the calculation of the total fiducial cross-section as $\hat{\sigma}_{\text{tot}} = \hat{\theta}_{\text{tot}}\sigma_{\text{tot}}^0$ while the normalized differential cross-sections are $1/\hat{\sigma}_{\text{tot}}\mathrm{d}\hat{\sigma}_j/\mathrm{d}X = \hat{\theta}_j F_j/w_j$ (for $j = 1 \ldots n$). The confidence intervals can be obtained in both cases either by profiling the θ_{tot} and θ_j (for $j < n$) parameters or by using the covariance matrix as previously described $\hat{\boldsymbol{\Sigma}}^{\theta}$. As in the previous case, the covariance matrix is used to obtain the confidence intervals since it has only minor differences compared to the profiling and is less computationally expensive. This new method of cross-section calculation has the advantage of removing the need to rely on the linear Gaussian approximation for the normalized differential cross-sections and allowing for the appropriate correlations between bins.

Given that the last bin n is determined uniquely based on the values of the other bins, its uncertainty is redundant because it is contained in the information of the other bins. However, to give a more immediate idea of what this uncertainty is, it is calculated by using the covariance matrix $\hat{\boldsymbol{\Sigma}}^{\theta}$ according to the constraints in Equation (25)

Having defined these methods, future sections will display the inclusive cross-sections as well as the normalized differential cross-sections. In the reporting of the inclusive cross-sections it must be noted that different observables within the same phase space can have different uncertainties and values based on how the nuisance parameters are constrained in different conditions. As such, the total cross-section will be measured by using the observable with the smallest expected uncertainty in the total cross-section.

An issue that presents itself in the calculation of the differential cross-sections is that some unfolded distributions do not have a well-defined upper bound. However, the number of events expected past a certain value becomes negligible and can be practically considered as the desired upper limit. This approach could be viable but depends strongly on which limit is effectively chosen but, if that limit is too high, that will lead to arbitrarily small differential cross-sections in the last bin. To account for these possibilities, a "reasonable" upper limit is chosen without a "systematic" calculation (ensuring that it contain any overflow events) and the differential cross-section is calculated based on the resulting width of the final bin.

8.2 Ancillary Observables in Unfolding

Ancillary variables have been added to the unfolding process to help differentiate between signal and background contributions and reduce the uncertainty of the unfolding results. These ancillary variables are added as an extra dimension to the unfolding histograms. By choosing the number of tight-tagged b-jets in each event as an ancillary variable, it is possible to produce signal-enriched and background-enriched regions which respectively give more information about the signal and help constrain the background.

A different number of regions is used for the ancillary variables depending on the phase space, this is done to ensure suitable statistics in each region. In the 5j3b and 6j3b3l phase spaces three regions are used: the first with zero or one, the second two, and the third three or more tight b-tagged jets. In the 6j4b and 7j4b3l phase spaces two regions are used: the first with less than three, and the second three or more tight b-tagged jets.

To allow for better visualization of the ancillary regions, they are unrolled and displayed side-by-side as is the case in Figure 32 which compared two pre-fit observables split by ancillary region.

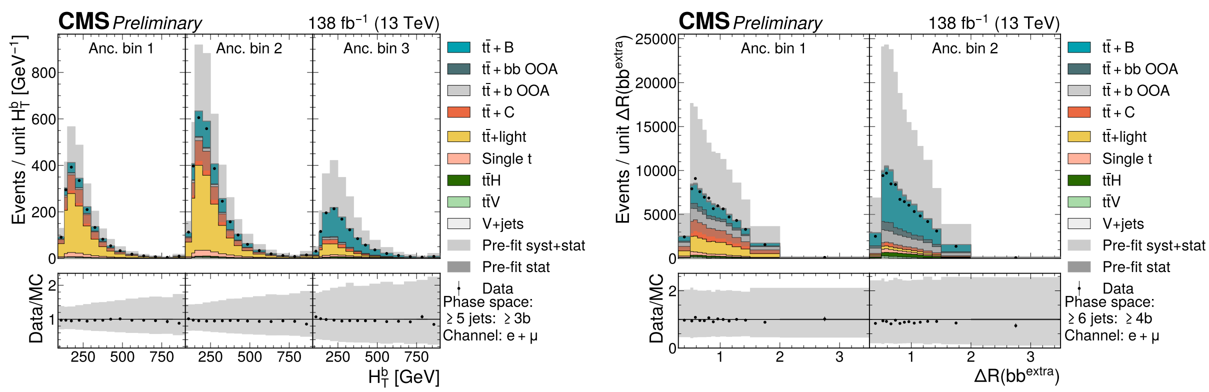

Figure 32: Reco-level pre-fit distributions of H_T^b in the 5j3b phase space (left) and of $\Delta R_{bb^{\text{extra}}}$ in the 6j4b phase space (right). The ancillary variables are unrolled and displayed side-by-side. The dataset is composed of e and μ channels summed together with all eras. The shaded bands include all the uncertainties considered. It can be noted that the higher ancillary regions contain a larger proportion of signal, indicating a signal-enriched region (and vice versa for the lower regions).

To determine the effectiveness of such an addition, it was decided to compare the best-fit uncertainties of the signal strengths in the two cases where the ancillary variable is and isn't used by using an Asimov dataset; that is to say, a dataset where all statistical fluctuations are suppressed and all the observable values are set equal to expectation.

The difference in sensitivity between fits with and without ancillary variables are displayed in Table 9.

Table 9: Result of the fit with and without the use of an ancillary variable. The values shown are the best-fit uncertainties of the generator-level bins of the ΔR_{bb} observable. The best-fit values are not shown as they are always 1.00 being fits to Asimov data (see Section 8.3).

gen-bin	[0.4, 0.6]	[0.6, 0.7]	[0.7, 0.9]	[0.9, 1.1]	[1.1, 1.4]	[1.4, 3.2]
`None`	$+0.16/-0.16$	$+0.16/-0.16$	$+0.17/-0.17$	$+0.19/-0.19$	$+0.22/-0.23$	$+0.26/-0.27$
`Ancillary`	$+0.10/-0.09$	$+0.11/-0.10$	$+0.10/-0.09$	$+0.10/-0.10$	$+0.11/-0.10$	$+0.11/-0.10$

Adding the ancillary variable is shown to decrease the best-fit uncertainties from $15-30\%$ to 10%.

8.3 Fit Validation

Having defined the fit procedure, a series of different tests were performed to validate the fit, confirming its expected behavior and investigating potential flaws. These tests were performed through the use of specially-produced pseudo-data based on a certain model. This is done to ensure that the distributions and central values of the pseudo-data are known so that the fit can be studied by using known quantities.

The model used to generate the pseudo-data was varied based on the validation test being undertaken to model different behaviors. The simplest method used was that with the so-called "Asimov Data" where the pseudo-data is set equal to the expectations without the presence of statistical fluctuations. This validation method is used for the most basic tests where it provides a consistency check on the fit while indicating how the data and its uncertainty are transformed by the fit. These tests are detailed in Section 8.3.1.

More complex are the frequentist studies where the nominal model is used to draw toys and, unlike the Asimov dataset, fluctuations are allowed according to the probability distribution of the model. The focus of these tests is to ensure the statistical coverage of the statistical model and check for biases. These tests are detailed in Section 8.3.2.

While the previous tests use the nominal model as a base, further tests were performed with pseudo-data derived from alternative models. This is done to ensure that the fit is not overly dependent on the nominal model being used to define it. These tests are detailed in Section 8.3.3.

8.3.1 Fits to Asimov Toy Data

The first test performed is a fit to Asimov data where the pseudo-data is set to be the same value that is expected in the model, without accounting for statistical variation. In the ideal case, the results of these tests should be the nominal values of the model. Their goal is to ensure that the fit functions properly at the basic level i.e. it outputs proper POI correlations, uncertainties, and nuisance parameters.

An example of such a fit is shown in Figure 33 relative to $\Delta R_{bb^{\mathrm{extra}}}$ in the 6j4b phase space. The image on the left shows the outcome of the fit for the normalized differential cross-section of the Asimov toy where the uncertainties have been obtained with the profiling method. Different icons on the plot represent the predictions of alternative models for reference compared to the nominal model. It can be noted that the unfolding process did not distort the Asimov value but kept it as expected while improving on the uncertainty compared to the pre-fit case (as seen in Figure 32). The right image shows correlations between the different POI of the fit as taken from the best-fit Hessian. As described in Section 8.1.2, one of the POIs scales the total cross section while the others scale the respective $n-1$ bins of the observable, with the last bin being determined from the others. From this plot it can be noted that adjacent parameters are anti-correlated, as expected for bins where events on their edge are likely to pass from one to the next.

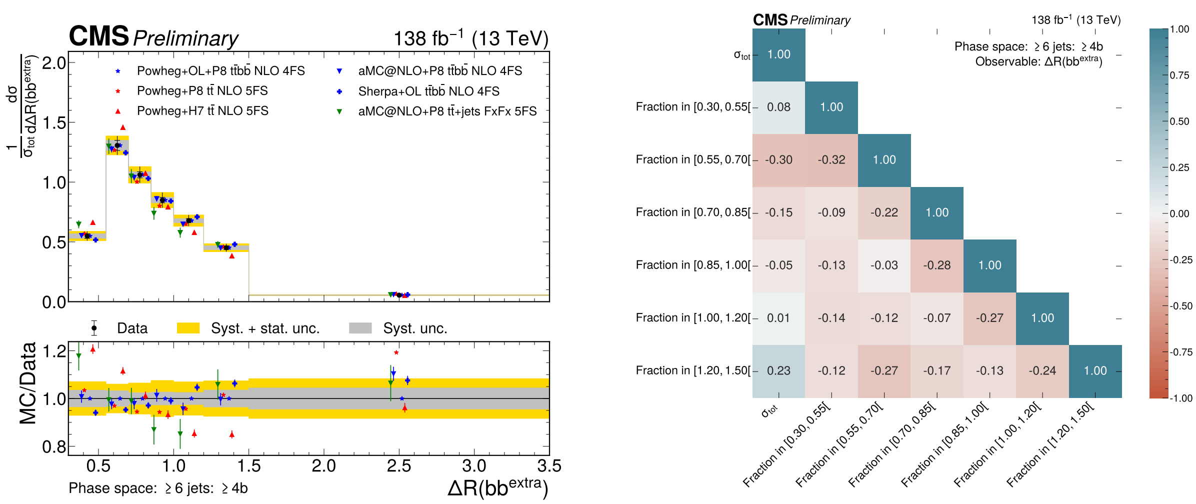

Figure 33: Results of fit for an Asimov dataset of $\Delta R_{bb^{\mathrm{extra}}}$ in the 6j4b phase space. The plot on the left shows the normalized differential cross-section of the Asimov toy. The plot on the right shows the correlation matrix between the POIs of the fit. The first parameter scales the total cross section while the other six scale the first six bins of $\Delta R_{bb^{\mathrm{extra}}}$.

This first look at the results of the fits gives a good starting idea of its performance but can be expanded by computing the *pulls*, *impacts* and *Kullback-Leibler (K-L) divergence* for the nuisance parameters being considered. The pulls are the post-fit values and uncertainties of the nuisance parameters and give an idea of how constrained each parameter is by the fit. In the current case of the simple Asimov toy, the post-fit value should be equal to the pre-fit case (i.e. zero) while the uncertainties should be equal or less than the Gaussian constraint term in Equation (13) (i.e. ≤ 1). It is expected that the nuisances will be constrained because of the information resulting from the ancillary variables and binning that the fit uses to better understand the signal and background. However, care must be taken that these nuisances are not excessively constrained because that case would indicate problems in the systematic uncertainty definition and modelling requiring a deeper study

The "profiled" impacts represent the relative impact that each nuisance parameter has on the parameter of interest if the nuisance parameter were fixed at its upper or lower limit. This impact can be estimated based on the covariance matrix used for the fit as $\hat{\mathbf{\Sigma}}_{pn}/\sqrt{\hat{\mathbf{\Sigma}}_{nn}}$ where $\hat{\mathbf{\Sigma}}$ is the covariance matrix, n is the nuisance parameter and p the POI. As in previous cases, the calculation of the impact via covariance matrix is much less computationally expensive than the profiling case and obtain similar results (though the covariance results are symmetrical, unlike the profiling case). For these reasons, the impacts are calculated with the covariance matrix for test cases and profiled for the final results. For ease of visualization, the impacts of the nuisances are shown relative to the total fiducial cross-section (corresponding to the first POI).

The K-L divergence instead indicates the impact that each nuisance parameter has on the shape of the unfolded distribution rather than its overall value and is a measurement of how much the given probability distribution differs from another distribution used as reference [103]. The K-L divergence D_{KL} can be calculated as:

$$D_{\mathrm{KL}}^{\alpha_i,\pm} = \sum_{j=1}^{n} \hat{F}_j \log\left(\frac{\hat{F}_j}{F_j^{I(\alpha_i,\pm)}}\right), \tag{26}$$

where $F_j = \sigma_j/\sigma_{\mathrm{tot}}$ are the bin fractions, $\hat{F}_j$ is obtained from the best-fit $\hat{\theta}_j$, and $F_j^{I(\alpha_i,\pm)}$ is derived from the up/down impact values following the nuisance parameter α_i

These three quantities are displayed in Figure 34 with the top twenty nuisance parameters arranged in decreasing order of impact on σ_{tot}. In this result of the Asimov fit, the nuisance parameters are seen to be constrained but not excessively. The largest impacts come from the nuisance parameters related to the b tagging, jet energy scale, and the modelling of $t\bar{t}$+light and $t\bar{t}$C backgrounds. The K-L divergence shows that certain nuisance parameters have a small effect on the shape of the distribution even if their impact on σ_{tot} is comparatively large, this is the case of the luminosity.

While Figure 34 shows the impact of the nuisance parameters on the total cross-section, it does not provide information about their impact on the differential cross-sections. This effect is shown in Figure 35 which has the shifts in the differential cross-sections caused by a setting certain nuisance parameters at their upper or lower pull values.

Figure 36 shows the inclusive fiducial cross-sections obtained with the Asimov fit for all observables considered. The cross-section of each observable in the same phase space has the same value, indicating the proper behavior of the fit. There are small differences in the uncertainties based on the observable used due to the different impact that the nuisance parameters have on the observable.

8.3.2 Frequentist Toy Fits

Having determined the validity of the Asimov fits, more stringent tests were attempted in the form of frequentist toy fits to check the coverage and bias of the nominal model being used. The pseudo-data for these toys is generated following the nominal model distribution (with likelihood defined in Equation (13)) where the nuisance parameters are set to their default value of zero and the POIs (θ_{tot} and θ_j) are set to a pre-determined value $\vec{\theta}_0 = \vec{1}$.

This generation results in a Poissonian distribution of events in each bin with the mean in the number of events expected in that bin.

The ancillary variables $\vec{A}$ corresponding to each event are also randomized where they are generated following a multivariate normal distribution where the mean is set according to the default value of the nuisance parameters $\vec{\alpha}_0 = \vec{0}$.

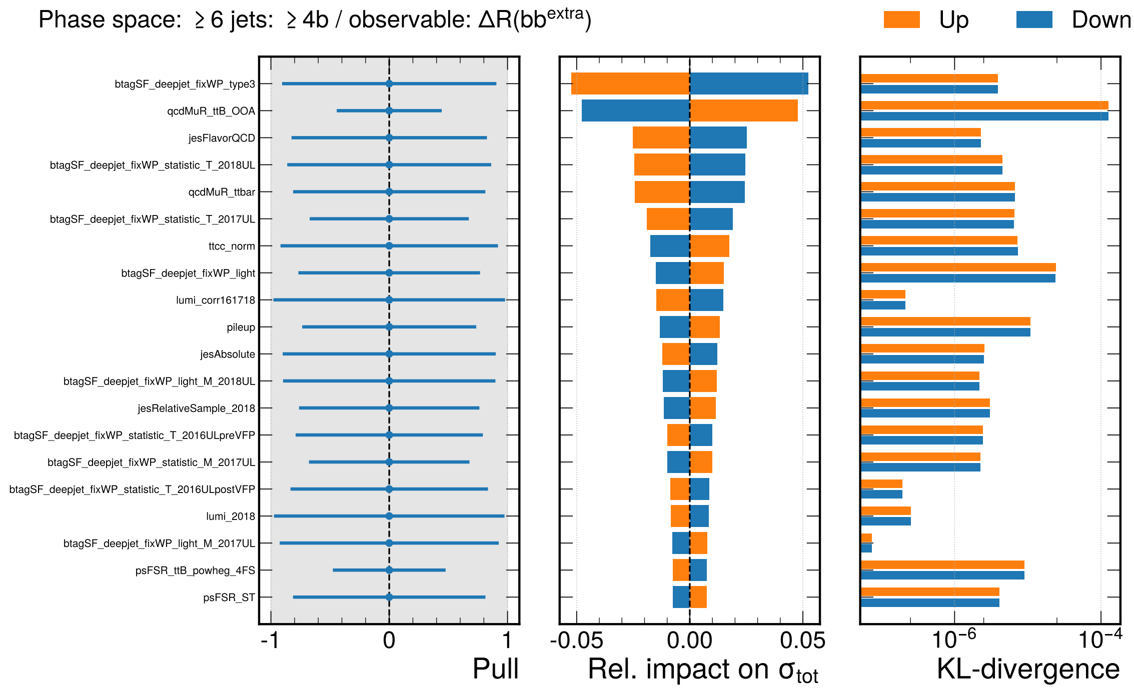

Figure 34: Pulls (left), impacts (center), and K-L divergence(right) for the Asimov fit of $\Delta R_{bb^{\text{extra}}}$ in the 6j4b phase space. Only the top twenty nuisance parameters arranged in decreasing order of impact on σ_{tot} are shown.

Having obtained these quantities, the yields observed for the toys $D_{e,i}$ and the ancillary variables $\vec{A}$ are used to fit the statistical model and check its coverage and bias. The expected coverage result in the case of a functioning fit is that the 68% confidence intervals $[\hat{\theta}_j^-, \hat{\theta}_j^+]$ (obtained via profiling, see Section 8.1.2) contain the true value of the toy 68% of the time. The expected bias result is that the mean difference between fitted and true value of the toy should be close to zero for the full set. A last element of study is the correlation between different parameters for the toy set. This can be compared to the Asimov dataset case to ensure a general level of compatibility between the ideal and frequentist cases.

An example of such a frequentist test for $\Delta R_{bb^{\text{extra}}}$ in the 6j4b phase space is shown in Figure 37 This produced the desired results as, while there is some bias in a few of the fitted parameters, the bias is very small and a roughly 68% coverage has been achieved for the $[\hat{\theta}_j^-, \hat{\theta}_j^+]$ 68% confidence intervals. A similarly positive result was obtained for the parameter correlations where a negative correlation between adjacent parameters is observed in a manner similar to the previous Asimov test (Figure 33 right).

8.3.3 Fits to Alternative Models

While previous tests showed the positive performance of frequentist and Asimov fits, they both relied on the 4FS inclusive model of $t\bar{t}b\bar{b}$ production. To ensure that this choice of fitting model does not bias the final results, it was decided to perform some Asimov fits by fitting a dataset based on model A with the migration matrix from model B. The expectation is that the choice of fitting model should not strongly affect the fitted result but leave it recognizable as the fruit of a different model despite biases from the difference in migration matrices. In practice, in the following tests the fit is performed by using the same migration matrices as previously (based on the 4FS $t\bar{t}b\bar{b}$ model) and using them on an Asimov dataset generated according to the 5FS $t\bar{t}$ prediction.

The results of these fits are shown in Figures 38 and 39 which respectively show the unfolded normalized

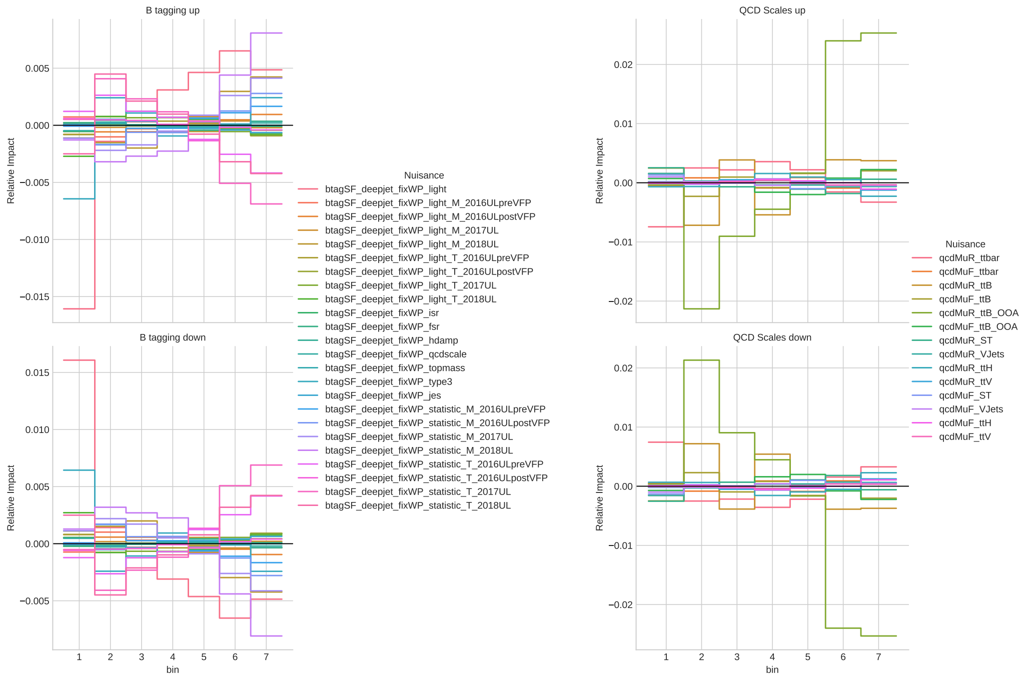

Figure 35: Impacts of select nuisance parameters on the differential cross-section for the Asimov fit of $\Delta R_{bb^{\text{extra}}}$ in the 6j4b phase space. The upper rows show the impact of the nuisance parameters on the distribution by setting the parameters at their upper pull value. Analogously, the lower rows show the impact when the parameters are set at their lower pull value. The left column has nuisance parameters related to the b-tagging efficiency while the right column has the uncertainties related to the renormalisation and factorisation scale.

distributions for a pair of observables and the inclusive cross-sections for the full list of observables. Based on these results, it is possible to see that a small bias is present in the differential cross-sections but that it is on the order of the systematic uncertainties of the distribution. This provides the expected result that the choice of model for the unfolding process does not overly affect the results and that the systematic uncertainties are estimated properly to account for such effects.

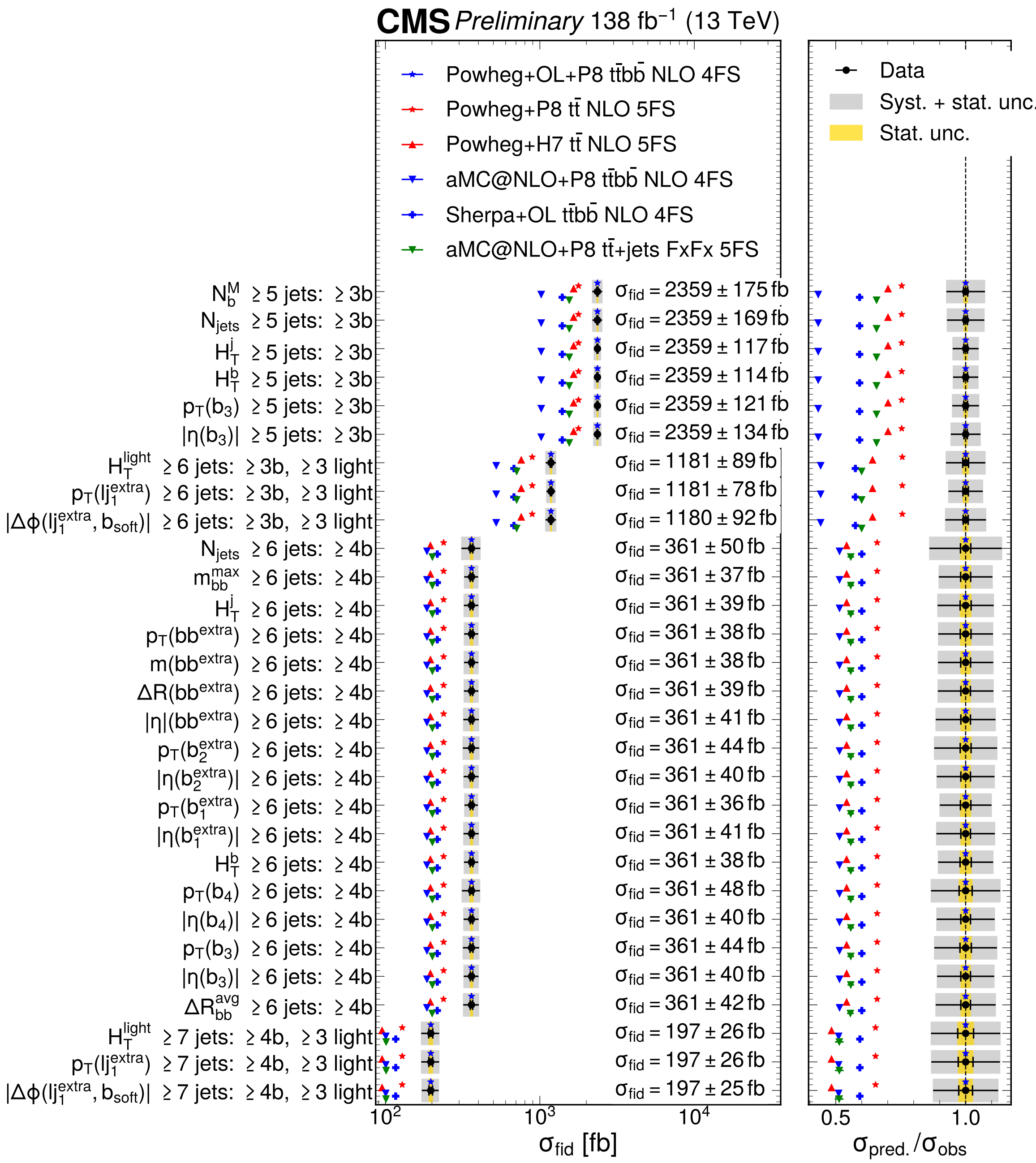

Figure 36: Inclusive fiducial cross-sections for all observables considered in their respective phase spaces derived from an Asimov fit. Different symbols are assigned to the predictions of different models. The left side indicates the absolute value of the inclusive cross-section. The right side has the inclusive cross-section and predictions normalized to the measured value of the inclusive cross-section, this is for easier comparison between models.

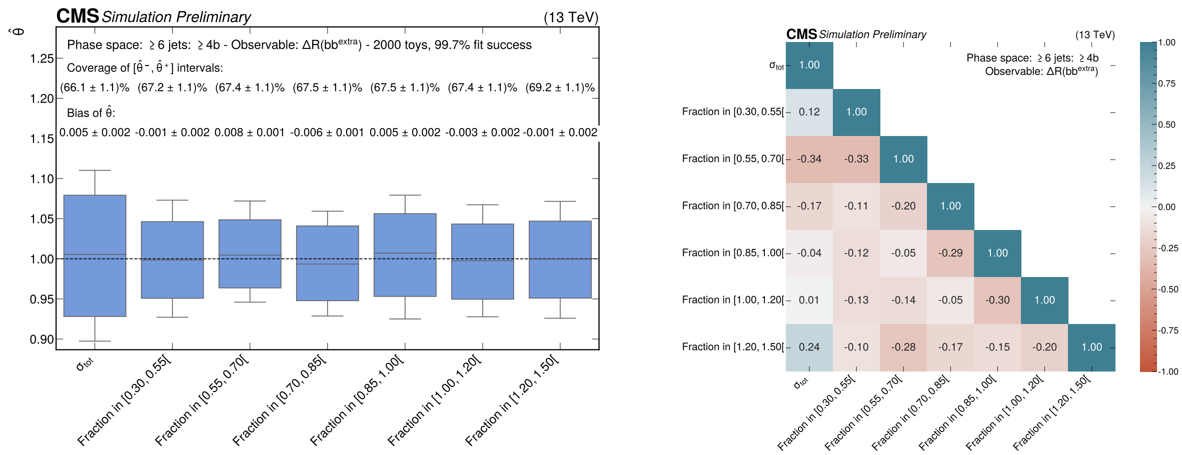

Figure 37: Analysis of the fit of 2000 frequentist toys of $\Delta R_{bb^{\text{extra}}}$ in the 6j4b phase space. On the left, each POI of the model is shown with its coverage and bias. The statistical uncertainties due to toy number are also indicated. The boxes indicate the 25%, 50% (median) and 75% thresholds for the spread of central toy values in the POI. The whiskers instead show the 68% best fit range from which the coverage is obtained. The right plot shows the correlation matrix between the POIs of the fit computed across all toys. The first parameter scales the total cross section while the other six scale the first six bins of $\Delta R_{bb^{\text{extra}}}$.

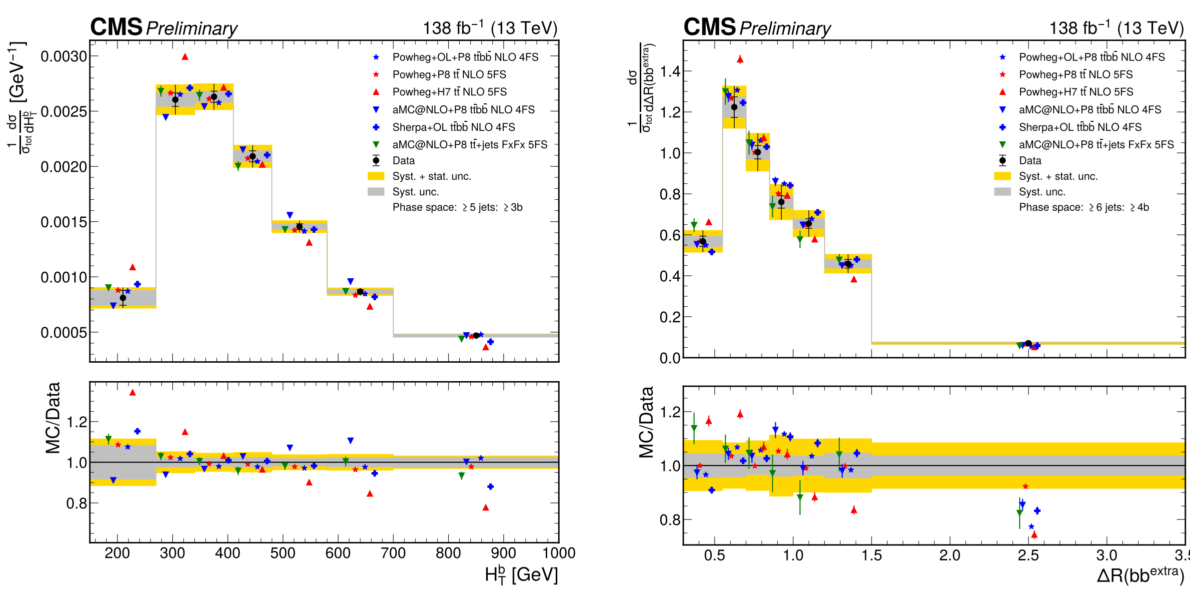

Figure 38: Unfolded normalized distributions of Asimov toy data generated from the POWHEG inclusive $t\bar{t}$ 5FS model (red stars) and fit with migration matrices generated from the POWHEG $t\bar{t}b\bar{b}$ 4FS (blue stars) model. The left plot displays the distribution for H_{T}^{b} in the 5j3b phase space while the right the distribution for $\Delta R_{bb^{\text{extra}}}$ in the 6j4b phase space. Small variations from the true 5FS distribution (red stars) are seen due to the difference in the model of the migration matrix but they remain within the systematic uncertainties.

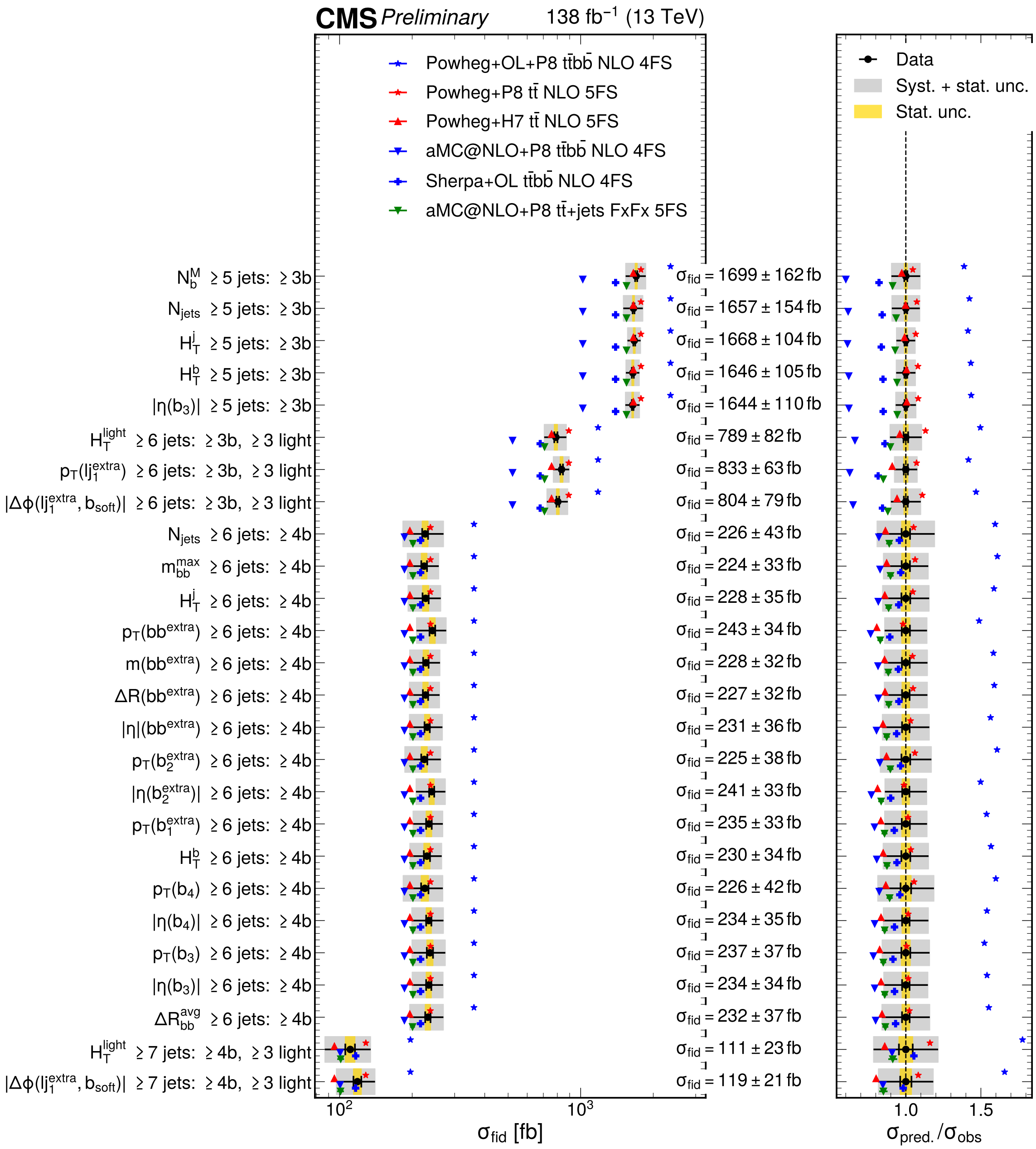

Figure 39: Inclusive cross-section for all observables studied with a comparison to various different models. Asimov toy data generated from the POWHEG inclusive $t\bar{t}$ 5FS model (red stars) and fit with migration matrices generated from the POWHEG $t\bar{t}b\bar{b}$ 4FS (blue stars) model.

9 Systematic Uncertainties

In order to properly estimate the uncertainties on the cross-section measurements in the analysis, several sources of systematic uncertainty need to be kept into account. This chapter details which uncertainties are used and how they are treated in the analysis. All systematic uncertainties and their correlations are summarised in Table 10. More details of these sources are listed below.

Table 10: Systematic sources used in the analysis with comments on potential caveats in applications or correlations.

Uncertainty source	Comment
μ_R scale	groups: $t\bar{t}$B + $t\bar{t}b\bar{b}$ OOA; $t\bar{t}b$ OOA ; $t\bar{t}$+light + $t\bar{t}$C; all others
μ_F scale	groups: $t\bar{t}$B + $t\bar{t}b\bar{b}$ OOA; $t\bar{t}b$ OOA; $t\bar{t}$+light + $t\bar{t}$C; all others
Top p_T modelling	Only for $t\bar{t}$+light, $t\bar{t}$C, $t\bar{t}$B, and $t\bar{t}$B OOA
PDF	Not applied to single top
PS scale ISR	groups: $t\bar{t}$B + $t\bar{t}b\bar{b}$ OOA; $t\bar{t}b$ OOA; all others
PS scale FSR	groups: $t\bar{t}$B + $t\bar{t}b\bar{b}$ OOA; $t\bar{t}b$ OOA; all others
ME-PS matching (h_{damp})	groups: $t\bar{t}$B + $t\bar{t}b\bar{b}$ OOA; $t\bar{t}b$ OOA; $t\bar{t}$+light + $t\bar{t}$C
Underlying event	Only for $t\bar{t}$B, $t\bar{t}$B OOA, and $t\bar{t}$+light/$t\bar{t}$C
Colour reconnection	Only for $t\bar{t}$B, $t\bar{t}$B OOA, and $t\bar{t}$+light/$t\bar{t}$C
b-fragmentation	Not applied to single top, W+jets, or Z+jets
Inclusive $t\bar{t}$C cross section	Only for $t\bar{t}$C
Luminosity	See Table 11
Lepton scale factors	Reco and ID for electrons, ID and iso for muons
Trigger efficiency	One for electrons, one for muons
L1 prefire correction	
Pileup	
Jet energy scale	Scheme with 7 sources
Jet energy resolution	Scheme with 2 sources
HEM issue	Only for 2018
b tagging light flavour	
b tagging heavy flavour (b, c)	Pileup correlated with other pileup variations
Size of MC samples	

Since the impact of systematic uncertainties is estimated based on simulated samples obtained via Monte Carlo event generation, it is possible for statistical effects to arise. If the statistical uncertainty on a systematic uncertainty is greater or similar to the effect size or there is significant bin-to-bin variation, it becomes necessary to smooth the systematic templates. The decision is based on an algorithm that decides how to treat the systematics based on whether they display a shape or rate effect. If the systematic displays a shape effect, then it is smoothed with a lowess-procedure [], if not, then the systematic is converted to a rate-only uncertainty. If, on the other hand, the systematic under investigation has neither a shape nor rate effect, then it is removed entirely.

Theoretical Uncertainties

The theoretical uncertainties are those systematic uncertainties that relate to the modeling of the backgrounds in the analysis together with the migration matrices involved in unfolding. Most of these uncertainties have shape-changing effects, with some also affecting the overall normalization value of the predictions. Given that the theoretical assumptions are the same across years, these uncertainties are correlated across all data-taking eras.

Particular attention must be taken with regard to migration matrices and the $t\bar{t}$B signal prediction. This is because the theoretical uncertainties affect $t\bar{t}$B at generator and reco level which changes the predicted cross-section at generator level. However, the cross-sections are measured based on the unfolding POI rescaling the nominal predicted cross-section without directly accounting for the uncertainties. To match this effect, the systematic variations of the migration matrix need to be rescaled in each generator-level bin so that the generator-level yields are constant for all corresponding nuisance parameters.

It must be noted that the OOA component of $t\bar{t}$B is not included in the signal and is treated as other backgrounds, maintaining modeling uncertainties on rates and shapes.

Another issue that needs to be addressed is the correlation between $t\bar{t}$B signal and $t\bar{t}$C/$t\bar{t}$+light backgrounds as they are all dependant on the underlying $t\bar{t}$ prediction but are separated by the phase space and additional radiation. A number of common-sense choices were made on this account and are detailed in the individual sections for each systematic.

μ_R, μ_F scales: The renormalization scale μ_R is introduced to cancel out divergences in the calculation of matrix elements in the simulation while the factorization scale μ_F is the energy scale at which the PDFs are evaluated. The uncertainties on these two scales account for their independent variation up to a factor 2 and are applied by the addition of event-specific weights. The μ_R and μ_F uncertainties are decorrelated between processes such as the $t\bar{t}$B signal, the OOA $t\bar{t}$B, $t\bar{t}$ background ($t\bar{t}$C and $t\bar{t}$+light correlated with each other), and each other lesser background. μ_R was noted as an especially impactful uncertainty on the $t\bar{t}b\bar{b}$ cross-section and consequently on the normalization of the OOA $t\bar{t}$B. Due to its large impact, its shape and normalization components were split and decorrelated. Also, regarding the splitting of the OOA signal into $t\bar{t}b\bar{b}$ OOA and $t\bar{t}b$ OOA, the two elements are correlated separately for this systematic with $t\bar{t}b\bar{b}$ OOA being correlated to $t\bar{t}$B signal and $t\bar{t}b$ OOA treated separately.

Top p_T modeling: A notable difference between simulation and data of the top quark pair production is present in top physics analyses, displaying in particular a softer top quark p_T than predicted. Top p_T reweighting is an empirical solution to this mismodelling based on the relation between generated and observed top quarks.

PDF shape: The PDF shape systematic uncertainty accounts for the description of the substructure of the simulated protons colliding and is estimated via the application of specific event weights. The PDF shape uncertainty is decorrelated between processes ($t\bar{t}$C and $t\bar{t}$+light correlated with each other).

Parton Shower scales ISR/FSR: The calculation of the parton showers in PYTHIA makes use of approximations that affect the amount of additional gluon radiation. These uncertainties are split into two: initial state radiation (ISR) and final state radiation (FSR). These two uncertainties are estimated by a variation up to a factor 2 of the gluon renormalization scale and are decorrelated between processes.

ME-PS matching (h_{damp}): In the POWHEG+PYTHIA simulation, POWHEG acts as the matrix element generator while PYTHIA performs the parton showering. The matching between these two is controlled by the h_{damp} parameter. The h_{damp} uncertainty is decorrelated between processes ($t\bar{t}$C and $t\bar{t}$+light correlated with each other).

Underlying event: With the PYTHIA event generator, the underlying event is tuned according to the CP5 tune. The uncertainty on this tuning is obtained through a comparison with samples whose tune settings have been varied relative to the standard CP5 as described in [104]. This uncertainty is treated as correlated for all $t\bar{t}b\bar{b}$ and $t\bar{t}$ processes.

Color reconnection: To simplify parton shower calculations, an approximation is used where an infinite number of colors are present and the color lines of additional multi-parton scattering are disconnected from each other and the primary. Color Reconnection (CR) is a phenomenological model used to account for these approximations. This uncertainty is taken by considering a number of alternate CR models and comparing them to the nominal simulation [105]. This uncertainty is treated as correlated for all $t\bar{t}b\bar{b}$ and $t\bar{t}$ processes.

B fragmentation: The theoretical uncertainty related to the fragmentation of b quarks into b hadrons is subject to modeling uncertainties. This is estimated with a variation of the b jet p_T up and down by 1% at generator and detector level.

Inclusive cross-section of $t\bar{t}$C: An additional 20% normalization uncertainty is applied to the $t\bar{t}$C process based on the inclusive $t\bar{t}$C cross-section measurement performed at CMS [75].

Experimental Uncertainties

Experimental uncertainties are added to every process with the corrections being applied to simulation while data is left unchanged. These uncertainties are correlated across all processes due to the same experimental setup being used but can vary by era due to changes in the detector.

Luminosity: These uncertainties account for uncertainties in the luminosity of LHC and vary by era as indicated in Table 11.

Table 11: Uncertainties on the LHC luminosity split by year.

	2016	2017	2018
Uncorrelated 2016	1.0%		
Uncorrelated 2017		2.0%	
Uncorrelated 2018			1.5%
Correlated 2016/2017/2018	0.6%	0.9%	2.0%
Correlated 2017/2018		0.6%	0.2%

Lepton reconstruction (tracking, reconstruction, ID, isolation): Lepton reconstruction scale factors are applied to the simulation to account for variations in lepton identification efficiencies between data and simulation. These scale factors are applied separately for electrons (reconstruction and identification) and muons (identification and isolation) and are a function of the p_T and η (or $|\eta|$) of the leptons. These uncertainties are propagated in the analysis and are correlated between years.

Trigger efficiencies: The differences in behavior of the trigger efficiencies between data and simulation are addressed via the application of dedicated trigger scale factors. For the muon channel, these scale factors were externally provided and derived by considering a control region enriched with $Z \to \ell\ell$. The electron trigger scale factors were produced specifically for the analysis by comparison with the muon scale factors in events with both an electron and a muon (as described in previous research [106]). These uncertainties are treated separately for muons and electrons.

L1 prefire correction: Due to certain trigger objects being assigned to the wrong bunch crossing, it is possible that certain events can be vetoed incorrectly. This effect is kept into account by applying specific kinematics-based weights onto the simulated events. The uncertainty on this correction is obtained via propagation of the prefiring for each object and is taken to be the squared sum of a 20% relative uncertainty and the statistical uncertainty. These uncertainties are correlated across eras.

Pileup reweighting: The difference between simulated and actual pileup is taken into account with the variation of the total inelastic proton-proton cross-section by a factor of 4.6% compared to the nominal simulation value. This uncertainty is correlated across eras.

Jet Energy Scale (JES): The energy of the reconstructed jets is related to the true particle-level energy through the jet energy corrections. Uncertainties on the jet energy scale are considered by shifting the JES up and down one standard deviation for the reconstructed simulation jets, this is done separately for a number of JES uncertainties. Given that this can affect the jet selections, the events are re-analyzed at the new shifted scales and propagated to the final distribution where they are considered as shape-changing uncertainties. The different JES uncertainties have different era correlations based on the single uncertainties with some components being fully correlated across years and others fully decorrelated.

Jet energy resolution (JER): Uncertainties on the jet energy resolution are considered by increasing or decreasing the difference between the energies of jets. Given that this can affect the jet selections, the events are re-analyzed at the new shifted scales and propagated to the final distribution where they are considered as shape-changing uncertainties. The JER uncertainties for jets with $|\eta| < 1.93$ and those for jets with $1.93 \leq |\eta| < 2.4$ are decorrelated with each other. These uncertainties are decorrelated across eras.

b-tagging scale factors: The b-tagging scale factors are used to account for the tagging efficiencies in the simulation. These scale factors are referred to as ”fixed working point” b-tagging scale factors as each jet is connected to the medium or tight working point based on the value of its DeepJet b-tagging discriminator. These factors are obtained by using a combination of different factors in QCD enriched and $t\bar{t}$ enriched regions independent from those used in the analysis. These uncertainties are separately derived and used for b jets, c jets, and light jets and have both correlated and uncorrelated factors between eras.

Size of simulated samples

The model predictions for the fit are obtained via Monte-Carlo simulations rather than an analytical function and thus are subject to statistical fluctuations. These fluctuations are taken into account by using a modified version of the Barlow-Beeston method [107] called Barlow-Beeston-lite [108].

The general method applies a nuisance parameter for each bin of each sample that is multiplied by the bin contents and constrained to the number of expected events or PDF. The full Barlow-Beeston method uses a Poissonian distribution for the expected PDF based on the number of expected events. Alternatively, the lite method used in this analysis uses only a single parameter for the yield of each bin while the constraint is Gaussian rather than Poissonian. The effective number of events for each bin which defines the variance of the Gaussian is calculated as:

$$n_{\text{eff}} = \frac{n^2}{\sum_{\text{proc}} e^2_{\text{proc}}}. \tag{27}$$

With n being the sum of events from all sources of background and e_{proc} the statistical uncertainty for each process.

10 Results

This section presents the results of the analysis, displaying the inclusive and differential cross-sections and their comparison to the signal models presented in 7.1.

10.1 Inclusive Fiducial Cross-Sections

Figure 40 shows the inclusive $t\bar{t}$ cross-sections measured for each of the chosen phase spaces together with a comparison to a number of different $t\bar{t}b\bar{b}$ generators both 5FS and 4FS. The $t\bar{t}b\bar{b}$ generator markers colored in blue are those that use massive b-quarks and NLO QCD $t\bar{t}b\bar{b}$ matrix elements, those colored in red are inclusive $t\bar{t}$ generators at NLO in QCD with massless b-quarks while the green markers also indicate generators with massless b-quarks where $t\bar{t}$ events have up to two additional jets with NLO QCD in the matrix element. These results are summarized in Table 12. The reported cross-sections were chosen in each phase space as those of the observable whose inclusive cross-section is closest to the average for its phase space. The observables that have been chosen to represent the inclusive cross-section for the different phase spaces are: $|\eta|$ of the third hardest b jet in p_T for 5j3b, $|\eta|$ of the sub-leading additional b jet for 6j4b, H_T of all light jets for 6j3b3l, and the azimuthal angle between the extra light-jet and the softest b-jet ($|\Delta\phi(\mathrm{lj}_1^{\mathrm{extra}}, b_{\mathrm{soft}})|$) for 7j4b3l.

The detector level distributions for these observables are shown in Figure 41 for 5j3b and 6j4b and in 42 for 6j3b3l and 7j4b3l after fitting to data and combining the datasets of all eras and channels.

Table 12: Measured and predicted inclusive cross-sections in the four considered phase spaces (in fb) compared with the predictions of different $t\bar{t}b\bar{b}$ simulations. The value chosen for this table was that of the observable whose inclusive cross-section is closest to the average for its phase space.

Fiducial phase space	5j3b	6j3b3l	6j4b	7j4b3l
Measured cross section	2368 ±142 (syst) ±14 (stat)	1036 ±90 (syst) ±12 (stat)	289 ±36 (syst) ±6 (stat)	144 ±25 (syst) ±5 (stat)
POWHEG+OL+P8 $t\bar{t}b\bar{b}$ 4FS	2361	1183	361	197
POWHEG+P8 $t\bar{t}$ 5FS	1791	899	240	129
POWHEG+H7 $t\bar{t}$ 5FS	1665	762	197	95
SHERPA+OL $t\bar{t}b\bar{b}$ 4FS	1391	677	216	116
MG5_aMC+P8 $t\bar{t}b\bar{b}$ 4FS	1024	524	187	101
MG5_aMC+P8 $t\bar{t}+$jets FxFx 5FS	1560	712	203	101

From these cross-section measurements in all phase spaces, we can note that the measured values exceed most theoretical predictions; this matches with previous observations by CMS [73, 74, 60] and ATLAS [71]. An exception to this statement is that of the POWHEG+OL+P8 $t\bar{t}b\bar{b}$ 4FS model whose reduced renormalization and factorization scale [79] results in larger cross-sections for all phase spaces. However, while this prediction matches the 5j3b measurement, it overestimated the cross-section in the other phase spaces between $10-35\%$. However, this is accounted for when the 50% renormalization scale uncertainties (estimated with a factor 2 variation of μ_R) of POWHEG+OL+P8 $t\bar{t}b\bar{b}$ 4FS are considered for both matrix element and parton shower; in this case, these predictions agree also with measurements in the 6j3b3l and 7j4b3l phase spaces that target additional light jet radiation for $t\bar{t}b$ and $t\bar{t}b\bar{b}$.

10.2 Normalized Differential Cross Sections

The normalized differential cross section is measured in all four considered fiducial phase spaces with 29 different observables acquired only through stable particle level information without the use of any simulation information. Eight of the 29 observables target the "extra b-jets" that are not derived from the decay of top quarks. The bin size for each observable was chosen on a case-by-case basis, taking into account the resolution of the observables and statistical uncertainty in the measured event yields. The normalized differential cross-sections so obtained are shown in Figure 44 for the observables of the 5j3b phase space, in Figures 45– 47

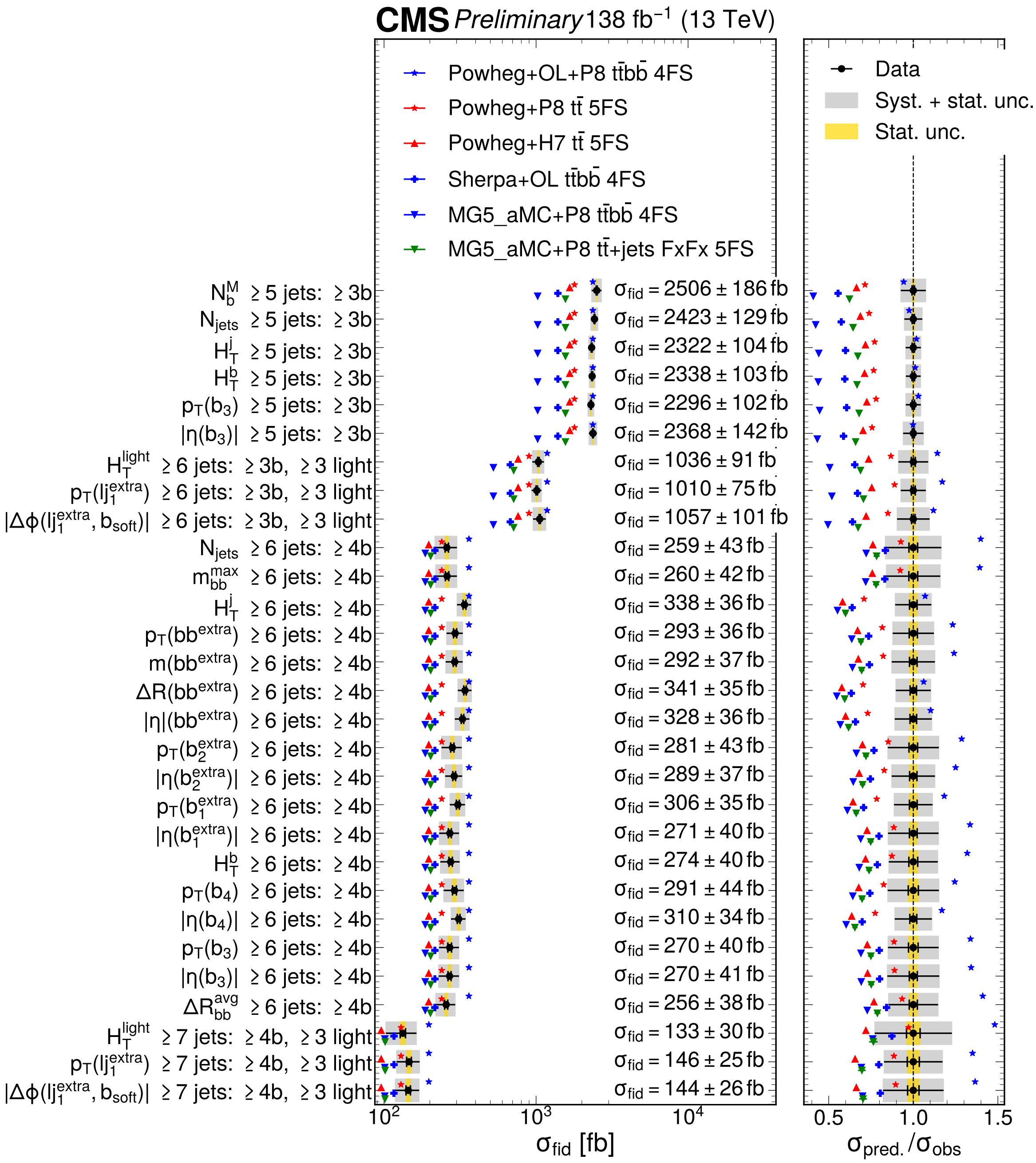

Figure 40: Inclusive $t\bar{t}b\bar{b}$ cross-sections measured for each considered phase space and compared to different $t\bar{t}b\bar{b}$ simulations. The plot on the left shows the value of the cross-sections while the one on the right shows the ratio between the predictions and the measured cross-section.

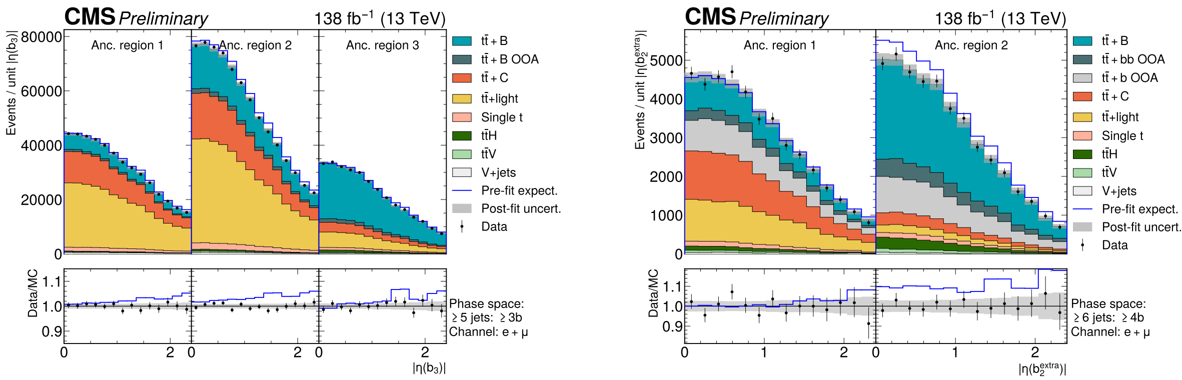

Figure 41: Detector level distributions after fit to data for the $|\eta|$ of the third hardest b jet in p_T ($|\eta(b_3)|$) in the 5j3b phase space (left) and the $|\eta|$ of the sub-leading additional b jet ($|\eta(b_2^{\text{extra}})|$) in the 6j4b phase space (right). The distributions shown combine the datasets of all eras and lepton channels combined with the different ancillary variables shown side-by-side (see Section 8.2). The shaded bands indicate all the uncertainties included in Section 9 after nuisance parameter profiling. The blue line shows the pre-fit sum of the predicted yields for all processes with nominal $t\bar{t}b\bar{b}$ samples and cross-section for the signal. The overflow has been included in the last bin of each histogram.

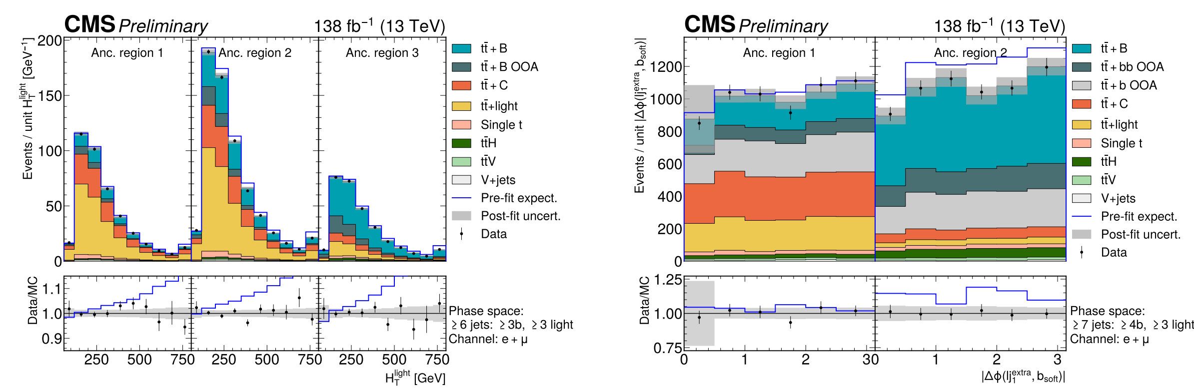

Figure 42: Detector level distributions after fit to data for the H_{T} of all light jets in the 6j3b3l phase space (left) and the azimuthal angle between the extra light-jet and the softest b-jet ($|\Delta\phi(\text{lj}_1^{\text{extra}}, b_{\text{soft}})|$) in the 7j4b3l phase space (right). The distributions shown combine the datasets of all eras and lepton channels combined with the different ancillary variables shown side-by-side (see Section 8.2). The shaded bands indicate all the uncertainties included in Section 9 after nuisance parameter profiling. The blue line shows the pre-fit sum of the predicted yields for all processes with nominal $t\bar{t}b\bar{b}$ samples and cross-section for the signal. The overflow has been included in the last bin of each histogram.

for the observables of the 6j4b phase space, and in Figure 48 for the observables of the 6j3b3l and 7j4b3l phase spaces. As in the previous section, these measurements are compared to six different predictions of $t\bar{t}b\bar{b}$ that are generated via different event generator and parton shower generators. These predictions are represented as differently colored symbols with the same significance as in 10.1. Note that the variables related to the additional b-jets are not compared to SHERPA+OL $t\bar{t}b\bar{b}$ 4FS predictions because that generator does not provide the required information (parton-level top quarks) to identify which b jets decay from top quarks and which do not.

From the results in Figure 43, it is clear that no event generator is able to describe every observable well even if different levels of compatibility are observed in individual cases.

This is particularly notable in the 5j3b phase space where none of the observables are well described by the predictions. The number of b jets N_b, which can be seen as an expression of the ratio between the $t\bar{t}b\bar{b}$ and $t\bar{t}b$ cross-sections, is only suitably described by the inclusive POWHEG $t\bar{t}$ simulations when matched to PYTHIA or HERWIG. On the contrary, the NLO $t\bar{t}b\bar{b}$ simulations predict a higher ratio than what is actually measured. The number of inclusive jets N_{jets} is generally overpredicted by most models though it shows better agreement with POWHEG+H7 $t\bar{t}$ 5FS and MG5_aMC+P8 $t\bar{t}$ + jets FXFX 5FS. The jet H_{T} (H_{T}^{j}) is reasonably well described by most models with the exception of MG5_aMC+P8 $t\bar{t}b\bar{b}$ 4FS which gives higher results than data and POWHEG+H7 $t\bar{t}$ 5FS which has the opposite expectation with lower values than data. The b jet H_{T} (H_{T}^{b}) is generally overestimated by simulation, except in the cases of POWHEG+H7 $t\bar{t}$ 5FS and SHERPA+OL $t\bar{t}b\bar{b}$ 4FS. The third b jet $|\eta|$ ($|\eta(b_3)|$) is mostly well described by the considered models.

In the 6j4b phase space, there is a better agreement between measurement and simulation, partially due to the increased measurement uncertainties, and the different models match each other more closely. The b jet H_{T} (H_{T}^{b}) and jet H_{T} (H_{T}^{j}) are well modelled for most simulations except for POWHEG+H7 $t\bar{t}$ 5FS which underestimates the measurements, as it already does in the 5j3b case; also H_{T} is poorly modelled in the low H_{T} region. The p_T and $|\eta|$ of the third and fourth b-jets ($p_T(b_3)$,$p_T(b_4)$,$|\eta(b_3)|$,$|\eta(b_4)|$) are mostly compatible with data though there is a minor trend of the data toward more central values for $|\eta|$ and lower values for p_T. The average ΔR between all pairs of b jets ($\Delta\text{R}_{bb}^{\text{avg}}$) and the maximum invariant mass of any b jet pair ($\text{m}_{bb}^{\text{max}}$) are slightly underestimated by the models considered, though this remains within the measurement uncertainties.

The observables in the 6j4b phase space that target the "extra b jets" are well modelled by the different simulations except for POWHEG+H7 $t\bar{t}$ 5FS which predicts a lower invariant mass for the $b\bar{b}$ pair and smaller angular separation in ΔR.

In the 6j3b3l and 7j4b3l phase spaces, the light jet H_{T} ($H_{\text{T}}^{\text{light}}$) and $|\Delta\phi(|)$ between the leading extra light jet and the softest b-jet ($|\Delta\phi(\text{lj}_1^{\text{extra}}, b_{\text{soft}})|$) are well modelled by most of the generators, with the exception of POWHEG+OL+P8 $t\bar{t}b\bar{b}$ 4FS that predicts a higher $H_{\text{T}}^{\text{light}}$. The extra light-jet p_T ($p_T(\text{lj}_{3/4}^{\text{extra}})$) tends to be overestimated by most predictions with only POWHEG+H7 $t\bar{t}$ 5FS matching the measurement more closely.

The compatibility of the different predictions with the measured distribution for each phase space was calculated via χ^2 tests. The χ^2 values were computed by using the predicted and measured normalized differential cross-sections together with the estimated covariance between the bins of the unfolded distributions. The inclusive cross-sections were not used for this calculation nor were the prediction uncertainties. The p-values from the χ^2 tests were converted to a z score. This indicates the number of standard deviations by which each theoretical prediction differs from the inclusive cross-section measurement. The z scores for all the observables considered are shown in Figure 43.

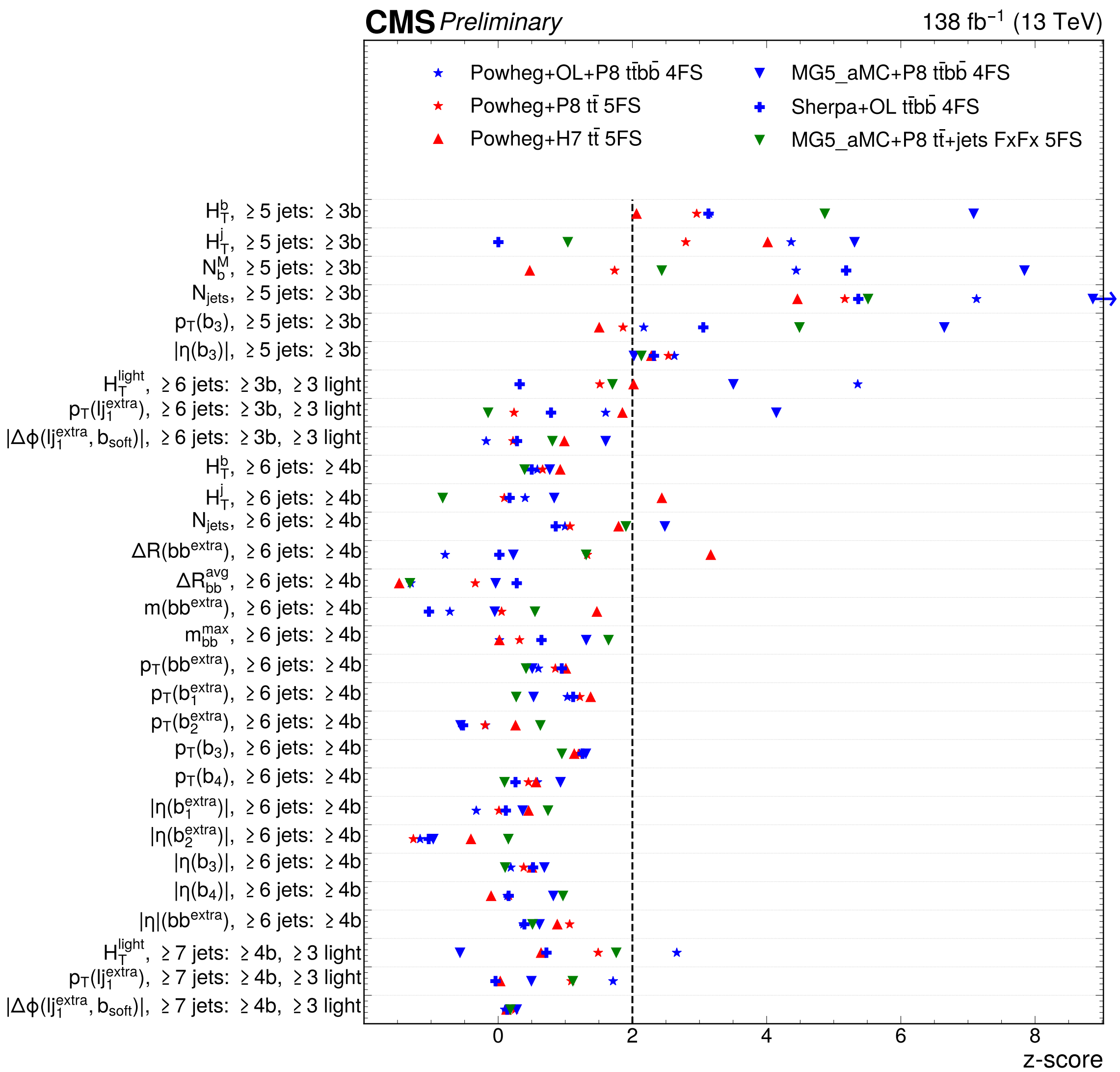

Figure 43: z score observed for each theoretical prediction based on the predicted and measured normalized differential cross-sections together with the estimated covariance between the bins of the unfolded distributions. A lower number corresponds to a better result, with the indicated 2 corresponding to two standard deviations away from the measurement. Some of the predictions fall out of the range of the plot and are indicated with an arrow (→).

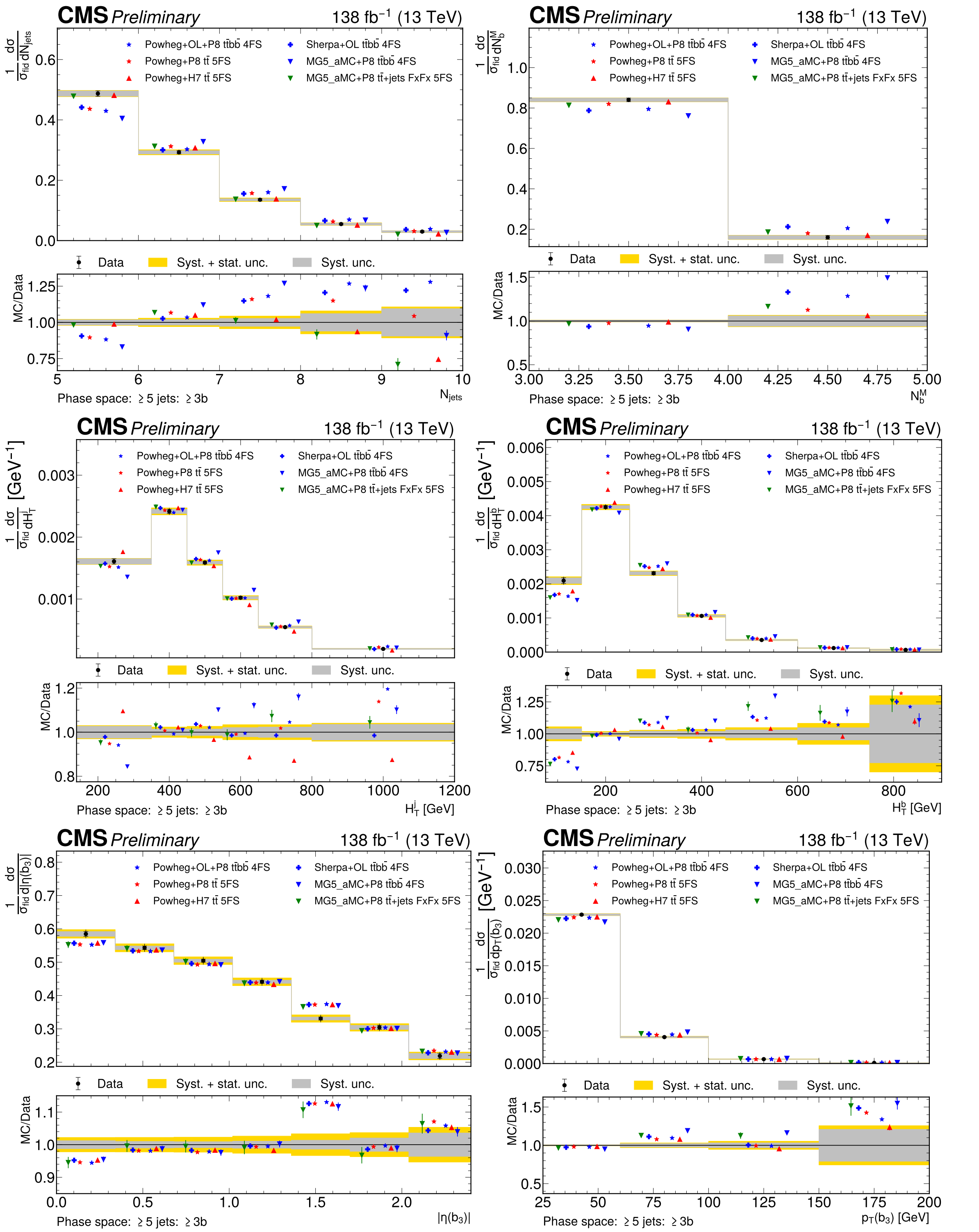

Figure 44: Measured normalized differential cross sections in the 5j3b phase space compared to different predictions represented with different symbols. The observables shown are the inclusive jet multiplicity (upper-left, N_{jets}), the b-jet multiplicity (upper-right, N_b), the inclusive jet H_{T} (middle-left, H_{T}^{j}), the H_{T} of b jets (middle-right, H_{T}^{b}), the $|\eta|$ of the third b jet (lower-left, $|\eta(b_3)|$), and the p_T of the third b-jet (lower right, $p_T(b_3)$). The last bins of N_b, N_{jets}, H_{T} and p_T contain the overflow. The measured values are indicated by black points with vertical bars representing the systematic uncertainties, these are also indicated by the gray bands while the total uncertainties are represented by the yellow bands.

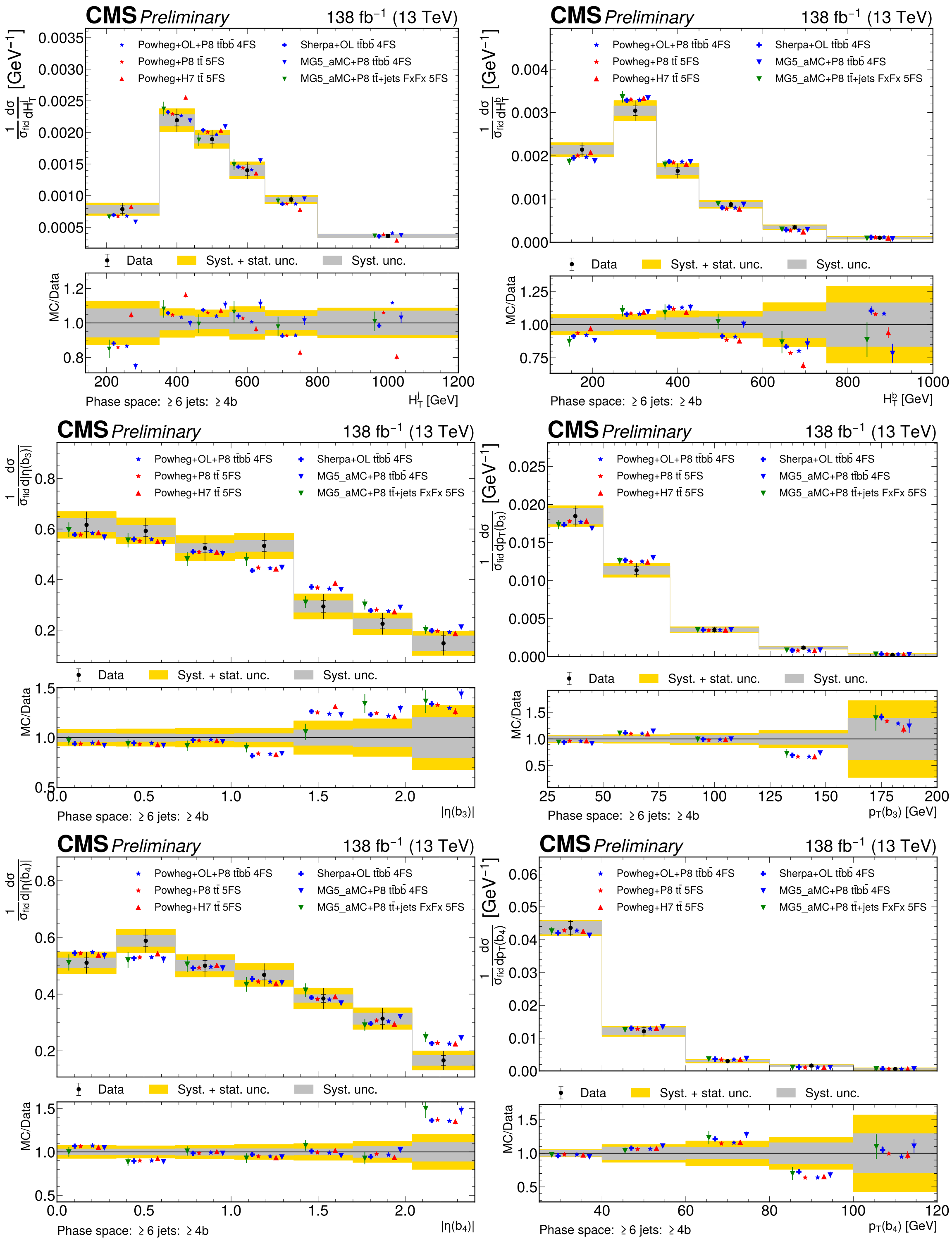

Figure 45: Measured normalized differential cross sections in the 6j4b phase space compared to different predictions represented with different symbols. The observables shown are the inclusive jet H_T (upper-left, H_T^{j}), the H_T of b jets (upper-right, H_T^{b}), the $|\eta|$ of the third b-jet (middle-left, $|\eta(b_3)|$), the p_T of the third b-jet (middle-right, $p_T(b_3)$), the $|\eta|$ of the fourth b-jet (lower-left, $|\eta(b_4)|$), and the p_T of the fourth b-jet (lower-right, $|\eta(b_4)|$). The last bins of H_T and p_T contain the overflow. The measured values are indicated by black points with vertical bars representing the systematic uncertainties, these are also indicated by the gray bands while the total uncertainties are represented by the yellow bands.

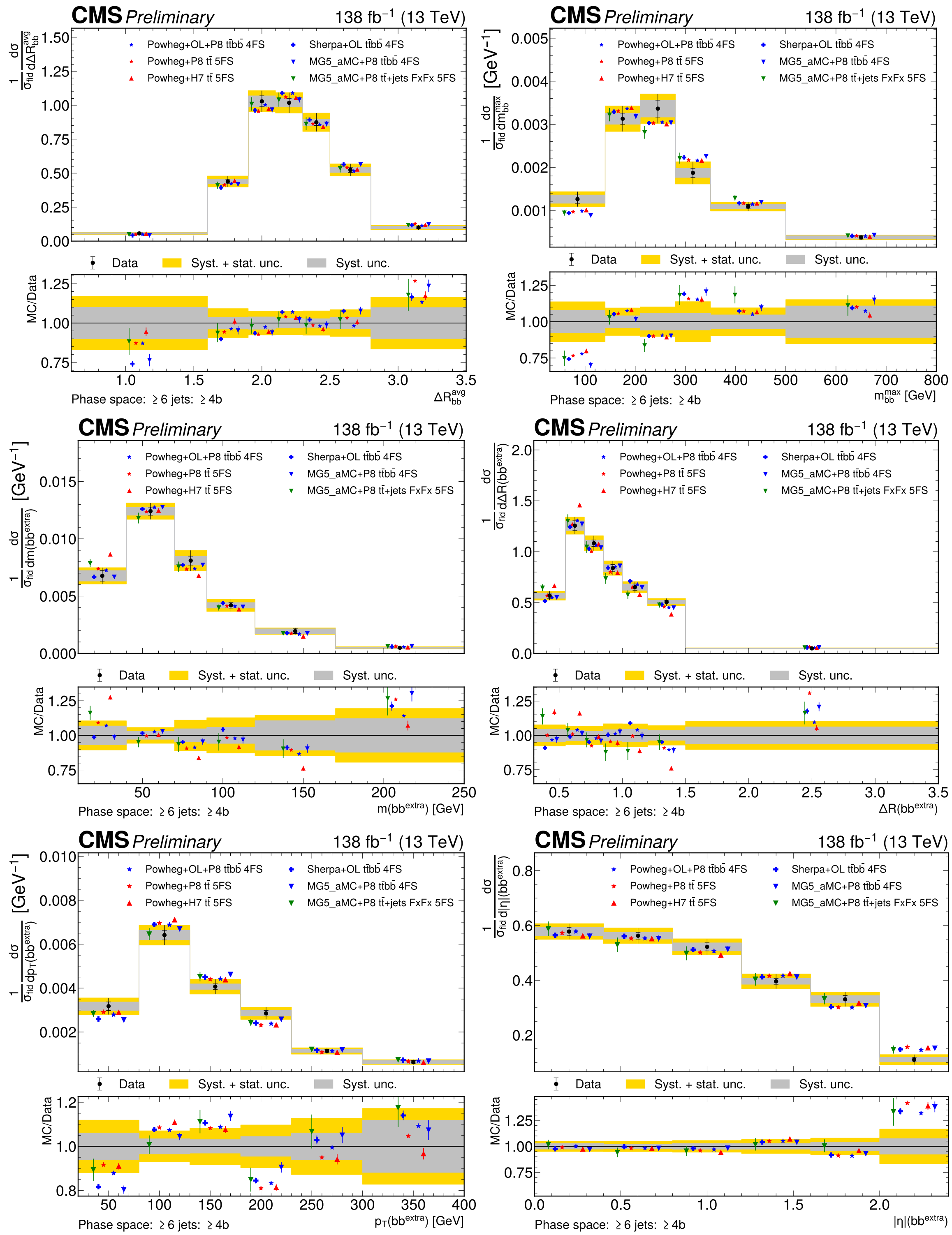

Figure 46: Measured normalized differential cross sections in the 6j4b phase space compared to different predictions represented with different symbols. The observables shown are the average ΔR of all possible $b\bar{b}$ pairs (upper-left, ΔR_{bb}^{avg}), the largest invariant mass of any $b\bar{b}$ pair (upper-right, m_{bb}^{max}) and the invariant mass (middle-left, $m(bb^{extra})$), ΔR (middle-right, $\Delta R_{bb^{extra}}$), p_T (lower-left, $p_T(bb^{extra})$), and $|\eta|$ (lower-right, $|\eta|(bb^{extra})$) of the extra b-jet pair. The last bins of m_{bb} and p_T contain the overflow. The measured values are indicated by black points with vertical bars representing the systematic uncertainties, these are also indicated by the gray bands while the total uncertainties are represented by the yellow bands.

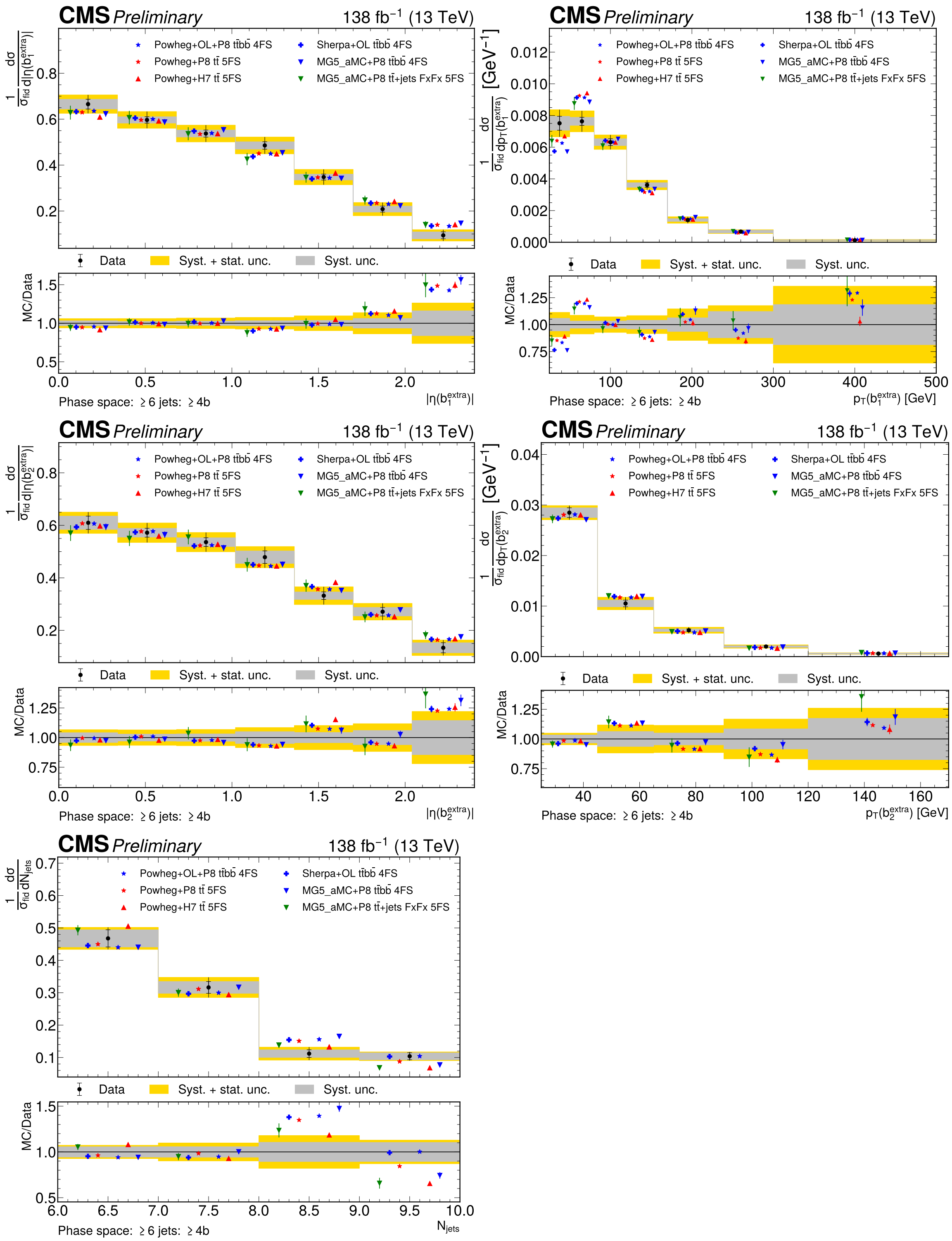

Figure 47: Measured normalized differential cross sections in the 6j4b phase space compared to different predictions represented with different symbols. The observables shown are the $|\eta|$ (upper-left, $|\eta(b_1^{\mathrm{extra}})|$) and p_T (upper-right, $p_T(b_1^{\mathrm{extra}})$) of the first extra b-jet, the $|\eta|$ (middle-left, $|\eta(b_2^{\mathrm{extra}})|$) and p_T (middle-right, $p_T(b_2^{\mathrm{extra}})$) of the second extra b-jet, and the inclusive jet multiplicity (lower-left, N_{jets}). The last bins of N_{jets} and p_T contain the overflow. The measured values are indicated by black points with vertical bars representing the systematic uncertainties, these are also indicated by the gray bands while the total uncertainties are represented by the yellow bands.

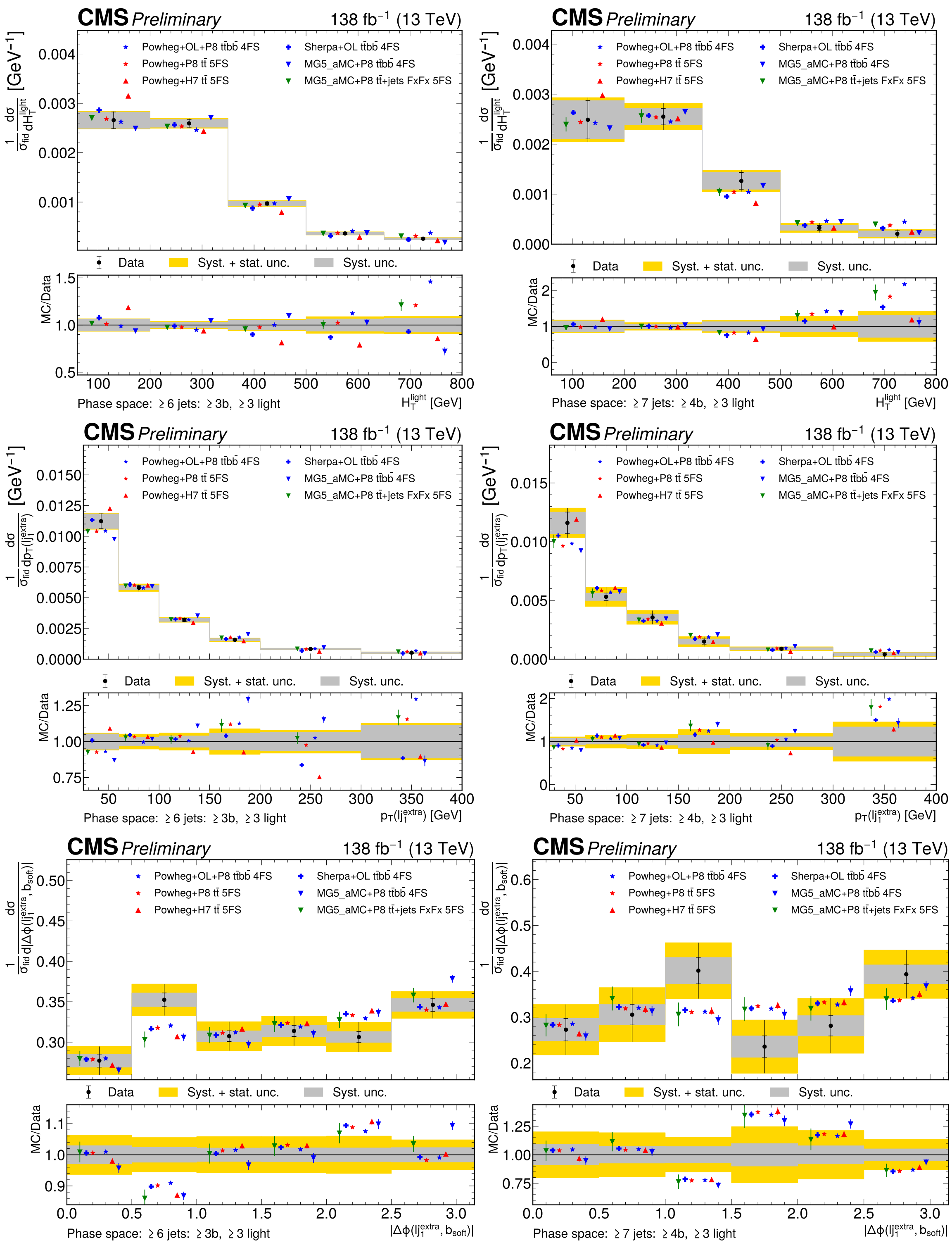

Figure 48: Measured normalized differential cross sections in the 6j3b3l (left) and 7j4b3l (right) phase spaces compared to different predictions represented with different symbols. The observables shown are the light jet H_T (top row, H_T^{light}), the extra light-jet p_T (middle row, $p_T(lj_1^{extra})$), and the $\Delta\phi(b)$ etween the extra light-jet and the softest b-jet (bottom row, $|\Delta\phi(lj_1^{extra}, b_{soft})|$). The last bins of H_T and p_T contain the overflow. The measured values are indicated by black points with vertical bars representing the systematic uncertainties, these are also indicated by the gray bands while the total uncertainties are represented by the yellow bands.

11 Analysis Summary

The analysis has produced measurements of the inclusive and differential cross-sections for the $t\bar{t}$ process in association with additional b-jets in the semi-leptonic decay mode, considering events with either an electron or a muon. These measurements were performed by using pp collision data gathered by the CMS detector at LHC with a center of mass energy of $\sqrt{s} = 13$TeV and an integrated luminosity of 138fb^{-1}. The cross-sections were measured in four different phase spaces with different jet, b jet and light jet multiplicity requirements, each targeting a different aspect of the $t\bar{t}b\bar{b}$ process. These measurements have achieved uncertainties in the $5 - 11\%$ range, making them the most precise measurements of the inclusive $t\bar{t}b\bar{b}$ cross-section to date. The uncertainties of the measurement are principally systematic sources whose largest component is that of uncertainties derived from the b-tagging calibration, jet energy scale, and renormalization scale for $t\bar{t}b\bar{b}$ signal and $t\bar{t}$ backgrounds. The differential cross-section measurements were performed as a function of a number of different observables in the aforementioned phase spaces and were chosen to primarily target b jets and additional light-jet radiation. Furthermore, in the 6j4b phase space, a series of observables were considered to target the "additional b-jets" which are those b jets not derived from the decay of a top quark. These additional b-jets are selected by choosing the two b-jets in the event closest to each other in ΔR. The uncertainties on the differential measurements are in the $2 - 50\%$ range and vary based on the phase space and observable considered. The measurements obtained are then compared to a number of different event generators to gauge their predictive ability where it was determined that no single generator can explain every observable in each phase space. In particular, the most inclusive phase space with at least five jets and at least three b-jets was poorly described by every model. In contrast, the phase space with at least six jets and at least four b-jets where the additional b-jets are resolved is generally well described by the generators studied. These newly performed measurements of the $t\bar{t}b\bar{b}$ production will aid in the improvement of the various event generators by allowing for a better determination of the theoretical uncertainties and the predicted central values of the $t\bar{t}b\bar{b}$ distribution.

Part II

Studies of the Readout Chip for the Phase 2 Upgrade of the CMS Pixel Detector

12 Inner Tracker Upgrade

The $t\bar{t}b\bar{b}$ analysis managed to achieve a more precise measurement than any other previous study in part due to the amount of data gathered by the CMS detector during Run2 from 2016 to 2018 amounting to an integrated luminosity of 138 fb^{-1}. One of the ways in which it is possible to improve measurements in the future is by increasing the integrated luminosity to provide ever greater amounts of data. This is the goal of the High Luminosity LHC (HL-LHC) [109, 110, 111] which aims to increase the instantaneous luminosity of LHC by approximately an order of magnitude (see Figure 49) and begin operation in 2029(see Figure 50 for the full schedule). However, this upgrade is not free of challenges as it will significantly increase pileup with up to 200 interactions per bunch crossing (approximately three to four times as many as in the current setup) and a much greater volume of information to process. To address these issues, significant work is being put into the upgrade of the CMS detector in view of an installation during the third Long Shutdown (LS3) between 2026 and 2028. In particular, the next chapters will describe studies testing the new solutions developed for the HL-LHC inner tracker.

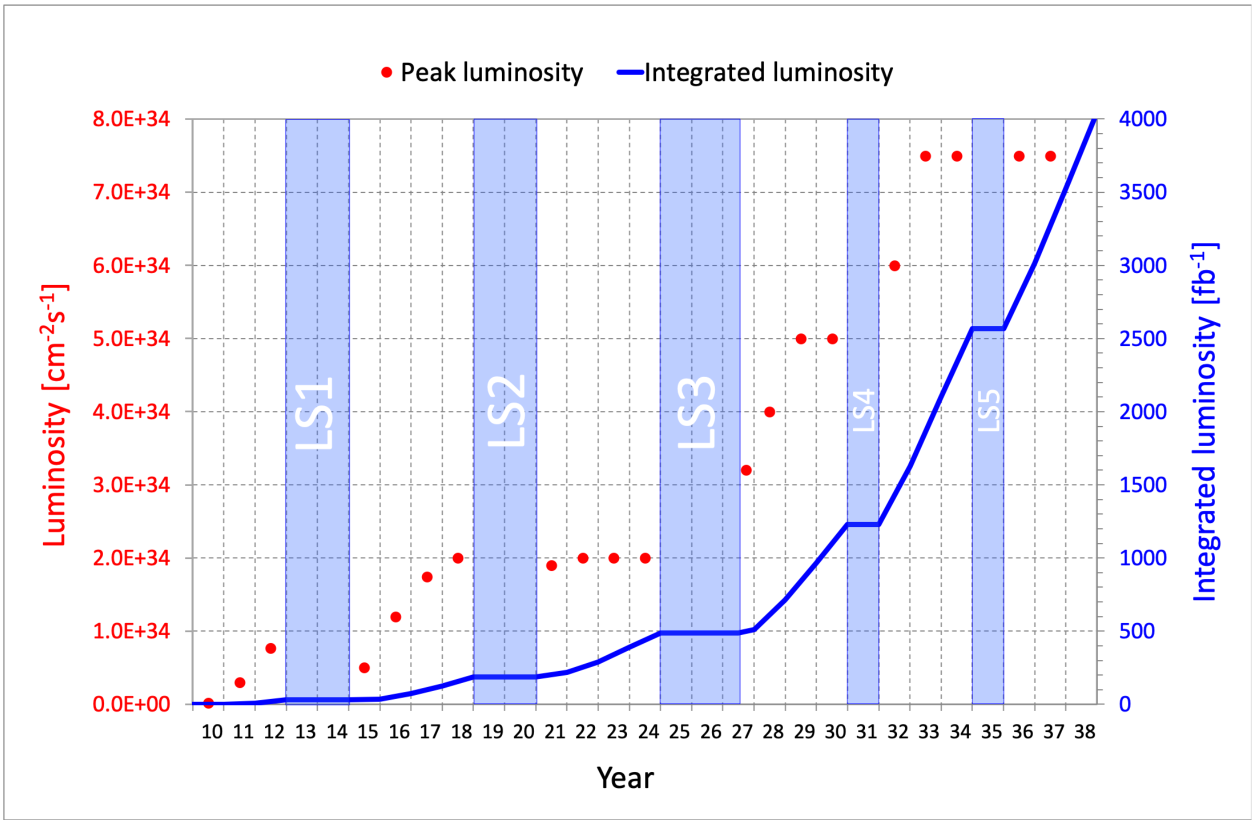

Figure 49: Expected peak luminosity (red dots) and integrated luminosity (blue line) by year. Note that the timeline displayed here is an older version before the revision in January 2022, refer to Figure 50 for the up-to-date timeline. Figure originally from [112].

12.1 Requirements

The HL-LHC inner tracker faces numerous challenges from the increased luminosity. Chief among these are the three to four times higher pileup, hit rate, trigger rate, and radiation than the current system. To account for this, the inner tracker is being designed with the capacity to withstand a radiation dose of 1.2 Grad. A number of solutions were identified to address these issues and improve physics performance such as an increased granularity (obtained by reducing the size of the tracker pixels), increased angular coverage up to $|\eta| \leq 4$, reduced material budget (a reduction in the light mechanics and service cables), and a new readout

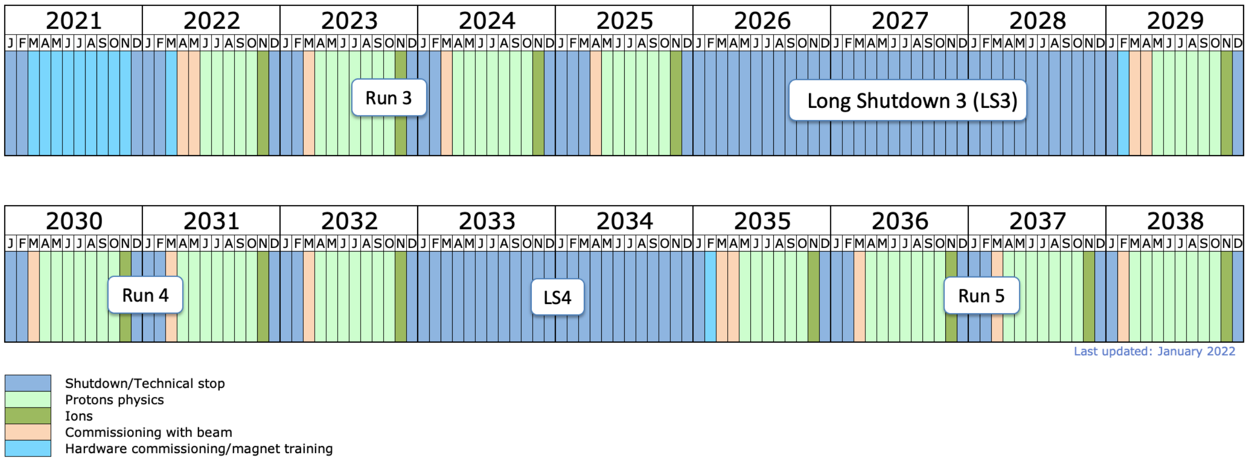

Figure 50: LHC schedule for LS3 and the beginning of HL-LHC. Figure originally from [112]

chip with a lower detection threshold. Improved tracking is particularly important for this goal because it can mitigate the effects of pileup in jets, MET, luminosity and lepton isolation with increased information. A diagram of the upgraded CMS tracker for HL-LHC can be seen in Figure 51.

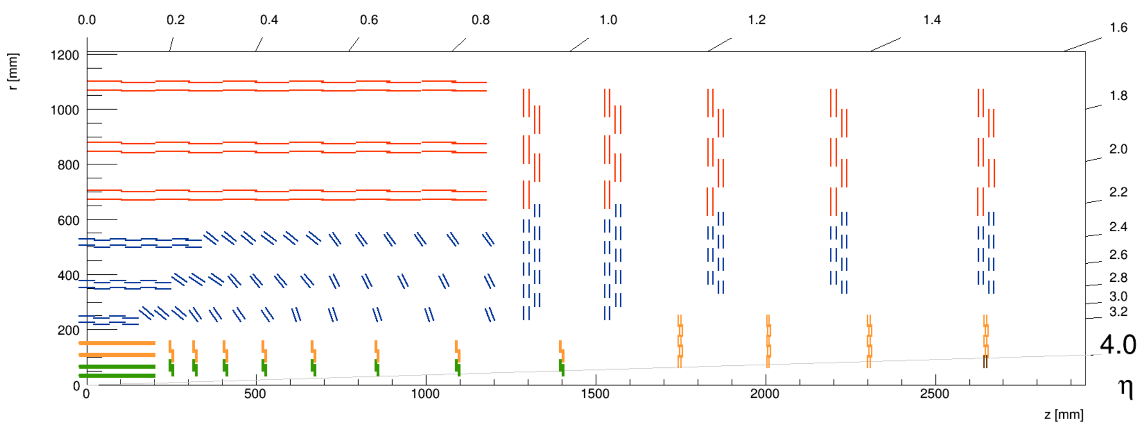

Figure 51: Diagram of one quarter of the upgraded CMS tracker for HL-LHC. The inner tracker is composed of silicon pixel modules with two (green) or four (yellow) readout chips per module while the outer tracker is composed of pixel strip sensor modules (blue), and two-strips sensor modules (red). Figure originally from [110].

A new tracker readout chip (whose basic design is common between CMS and ATLAS) was developed with an acceptable radiation hardness and the low-noise electronics to read out the relatively faint signals that can be provided by silicon sensors at the end of their lifetime.

12.2 RD53 Chip

The RD53 collaboration was established in 2013 to solve these issues and develop a new readout chip for HL-LHC [113]. A significant amount of work was put into radiation tolerance studies to allow for sufficiently radiation-hard circuits that can survive the environment presented by HL-LHC. The chip was also designed to function with serial powering where chains of a dozen chips can be supplied with current along the same line to reduce the amount of material in the detector and losses due to long cables.

A first pixel readout chip (RD53A) was developed in 2017 with all the necessary building blocks and three separate readout architectures that were tested for their individual performance [114, 115].

RD53A contained the common framework for the final CMS and ATLAS readout chips. Once its performance was deemed appropriate, two slightly different RD53B chips were developed in 2020 with improvements based on the RD53A experience [114]. The two CMS and ATLAS chips were distinguished primarily by the different choice in the analog section out of the three originally present in RD53A. The different chips can be seen in Figure 52. The next chapters will deal with both RD53A and RD53B as the experiments in question were conducted in the final stages of RD53A development and after the introduction of RD53B.

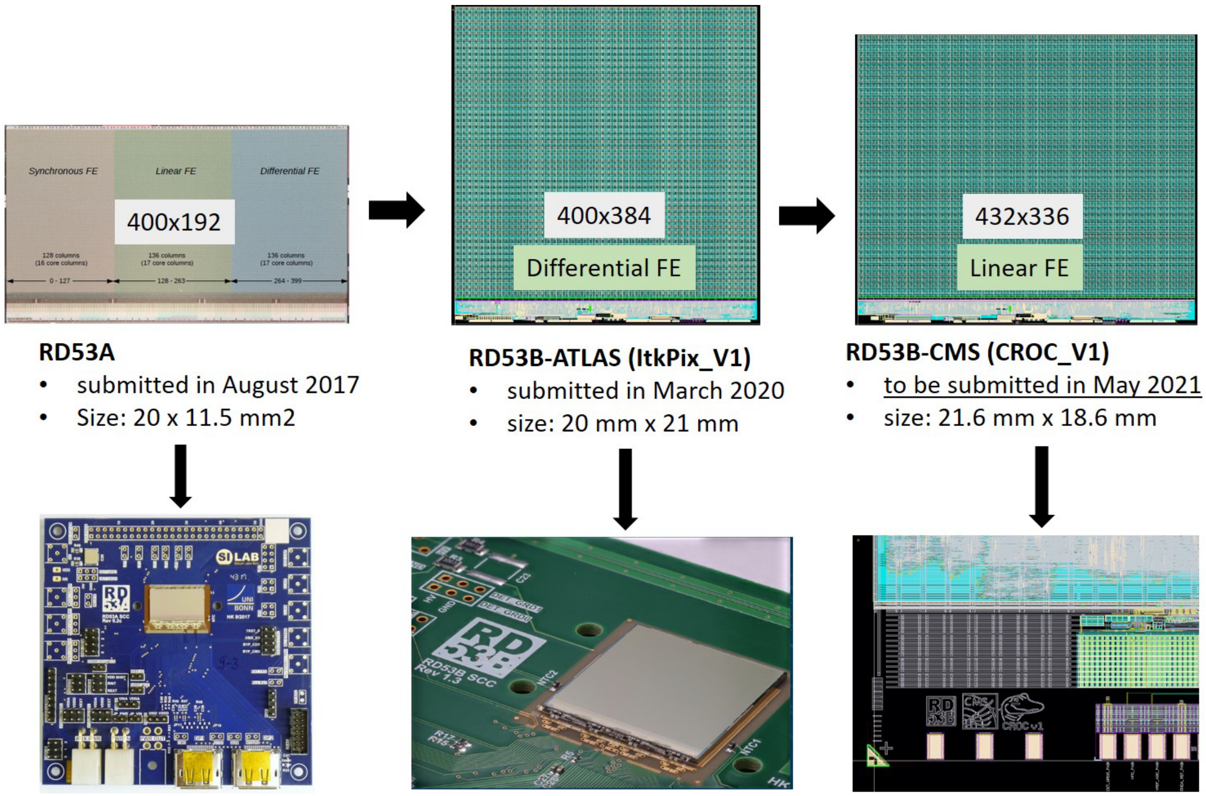

Figure 52: Different RD53 chip prototypes: from left to right, RD53A, ATLAS-specific RD53B, CMS-specific RD53B with their respective front ends. Figure originally from [110]

Outside of the pixel readout region, the RD53 is provided with a chip bottom that contains the control and processing elements together with a series of reference voltages and currents. These elements can be used to monitor the performance of the chip together with its temperature and radiation exposure.

A further important component of the RD53 chip are the protection elements for serial powering. These are a number of systems whose purpose is to maintain the function of a chain of chips powered in series under different failure conditions.

Section 13 will discuss the different tests that were run to validate the serial powering protections. Section 14 will deal with tests of the chip's functionality under high doses of irradiation and the methods used to measure this functionality.

13 Serial Powering Tests

The RD53 chips were designed with a serial powering scheme in mind and dedicated tests were started with the RD53A prototype. This is intended to reduce any power losses due to long cables and reduce the amount of material present in the detector by having a single current line connecting a chain of modules. Figure 53 shows a schematic for the serial powering setup with two powering lines present shown in blue and red. The blue line powers the digital logic and front end of the chips and is a relatively low voltage with a current of the order of 1 A. This is the element for which the serial powering scheme is applied. The red line instead serves to bias the sensor for tracker detection and this is a much higher voltage contrasted with a current before irradiation of the μA order.

The intended setup should have up to twelve pixel modules powered in series with a constant current and a total of 500 serial powering chains in the inner tracker [116].

To ensure a common operational voltage for these chains, each RD53 chip is provided with a Shunt-LDO Regulator (SLDO) which combines two separate functionalities. The Shunt section regulates the input voltage for the LDO (Low-DropOut regulator) based on the chip's input current while the LDO serves to output a fixed voltage of 1.2 V that powers the pixel chip. These elements allow for each chip in the chain to be powered with the same voltage and current regardless of its position in the chain. The behavior of input and output voltages based on input current under normal operational conditions is illustrated in Figure 54.

However, it must be noted that maintaining the chips connected in series can lead to the failure or malfunction of the whole chain if one of the chips within it is compromised. The issue of a total chain failure is addressed at first by allowing the current to bypass an unresponsive module and continue along the chain but this does not ensure that the other modules would not fail in turn due to transitional effects. These issues were addressed by different measures such as Undershunt Protection (USP) and Overvoltage Protection (OVP) that will be described below.

13.1 Undershunt Protection

Undershunt protection is used to protect chips in series from the effects of the failure of an upstream chip. This can be dangerous for a number of reasons. Firstly, this type of failure will cause an increase in the input voltage of the downstream chip which could be damaging if it exceeds the 2 V limit. Furthermore, the upstream chip failure can lead to dangerous transient behaviors in the downstream chip which could impact the V_{out} and compromise the functioning of the chip. This protection of the USP is achieved by lowering the output voltage of the failing upstream chip below its operational value which, in turn, allows the current of the chain to be undisturbed.

Different tests were performed under separate chip configurations to evaluate the usefulness and performance of the USP.

13.1.1 Series Test

The first such test was conducted by setting two chips in series and forcing the upstream chip to fail by subjecting it to a 1 A load pulse of the length of 1 ms to simulate an unusually high current requirement which can occur during an especially populated event. This effect is particularly visible in the case where the current required by the chip is higher than the one passing through the serial powering line. This was the case of the experiment that was conducted where the current input by the serial powering line was $I_{in} = 0.9$ A and the load current requested by the chip and required to make it fail was $I_{load} = 1$ A.

The experiment was conducted with this same setup in two separate conditions according to the diagram in Figure 55. In the first case, the USP was not active, allowing the voltages and currents involved to vary without stabilization. In the second case, the USP was activated and stabilized the involved voltages and currents. In both cases, the upstream and downstream chips were monitored with an eye towards maintaining the V_{out} of the SLDO at a constant 1.2 V, which would allow for continued operation of the chip. The other quantities monitored were the V_{in} provided by the Shunt, the I_{in} current of the serial powering line, and the I_{load} causing the failure.

The results of these experiments are shown in Figure 56. This allows several conclusions to be drawn. First, it is immediately apparent that the application of the USP stabilizes the behavior of voltages and

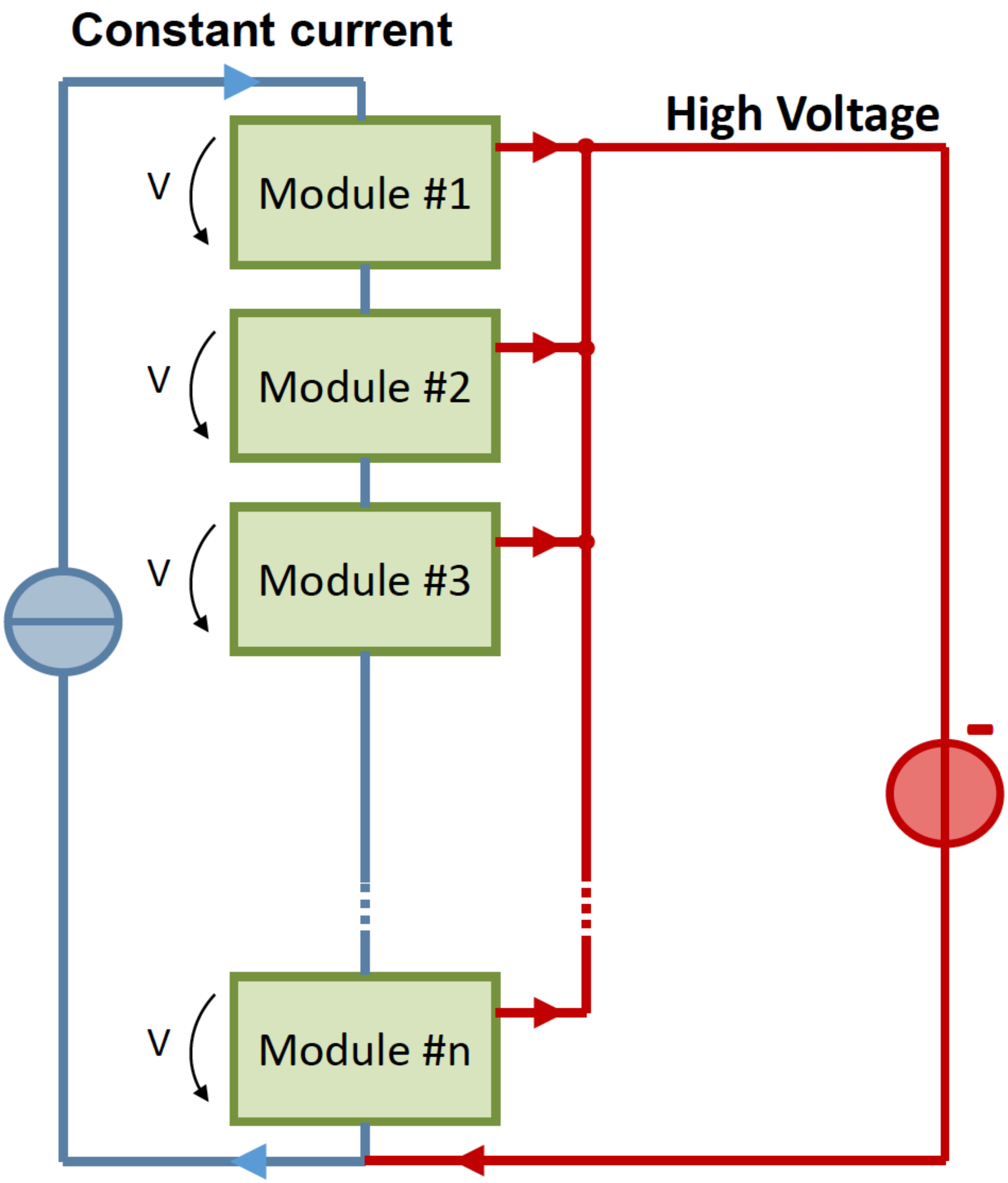

Figure 53: Schematic of the serial powering chain for RD53. The current line in blue powers the digital logic and front end of the chips and delivers a constant current to all the modules in the chain. The voltage line in red provides the necessary high voltage to each module for the functioning of the pixels. Figure modified from [116].

currents for both upstream and downstream chips at the expense of an 0.4 V reduction in the V_{out} of the chip whose excessive load caused it to fail. This behavior allows for the continued functioning of the downstream chip as its operational voltage is a constant $V_{out} = 1.2$ V. In contrast, if the USP is not active, the relevant voltages and currents oscillate at the beginning and end of the load pulse, forcing the downstream chip to endure a $V_{in} = 2.3$ V, which risks damaging the chip as the maximum recommended voltage is $V_{in} = 2.0$ V. However, it is interesting to note that the V_{out} of the downstream chip remains constant. This would allow for continued functioning of this module, particularly if the dangerously high

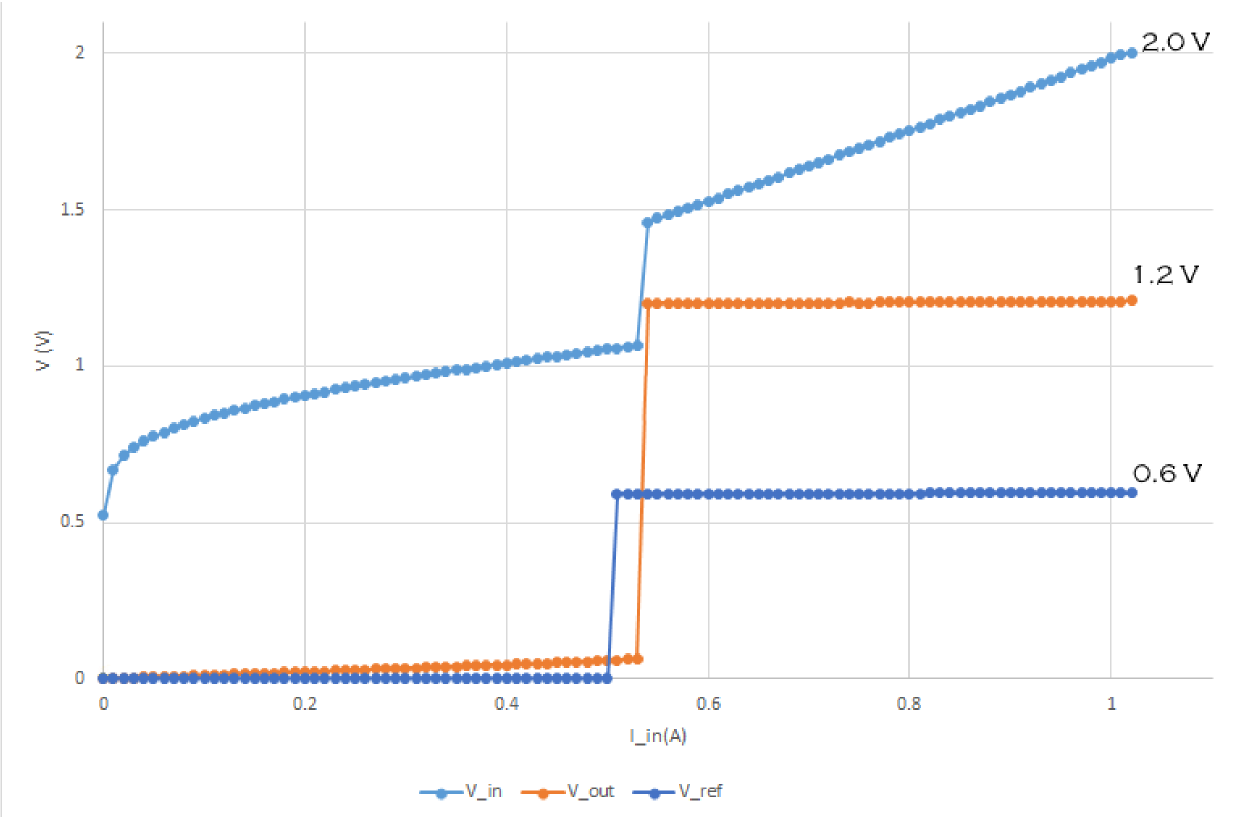

Figure 54: Plot of the voltage regulation in the RD53 modules. The V_{in} is the voltage provided by the Shunt based on the constant input current. The V_{out} is the voltage output by the LDO to power the pixel chip while the V_{ref} is a reference voltage used to generate the V_{out}. It can be noted that, once the V_{in} passes a certain current threshold, the desired $V_{out} = 1.2$ V is generated and remains constant regardless of current or V_{out}.

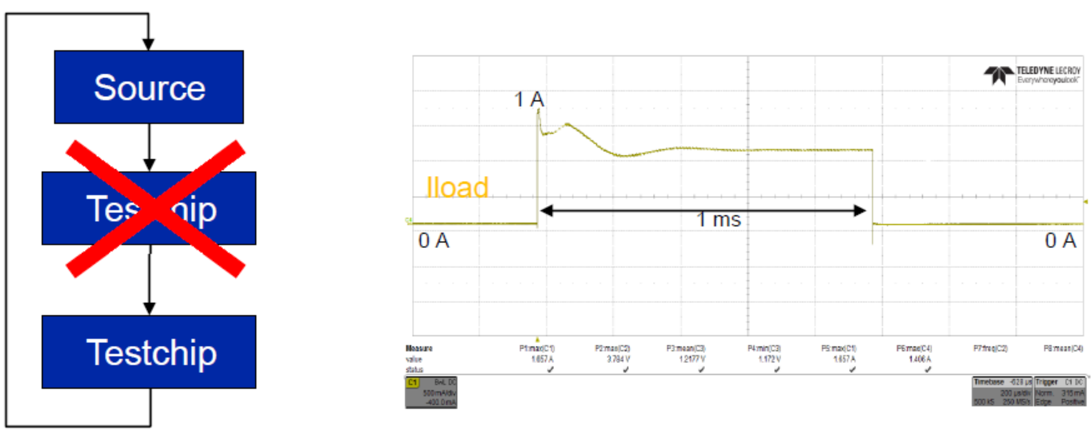

Figure 55: Schematic of the experimental setup (left) and oscilloscope image of the load pulse used to induce the failure of the upstream chip (right).

V_{in} can be limited to a safer value.

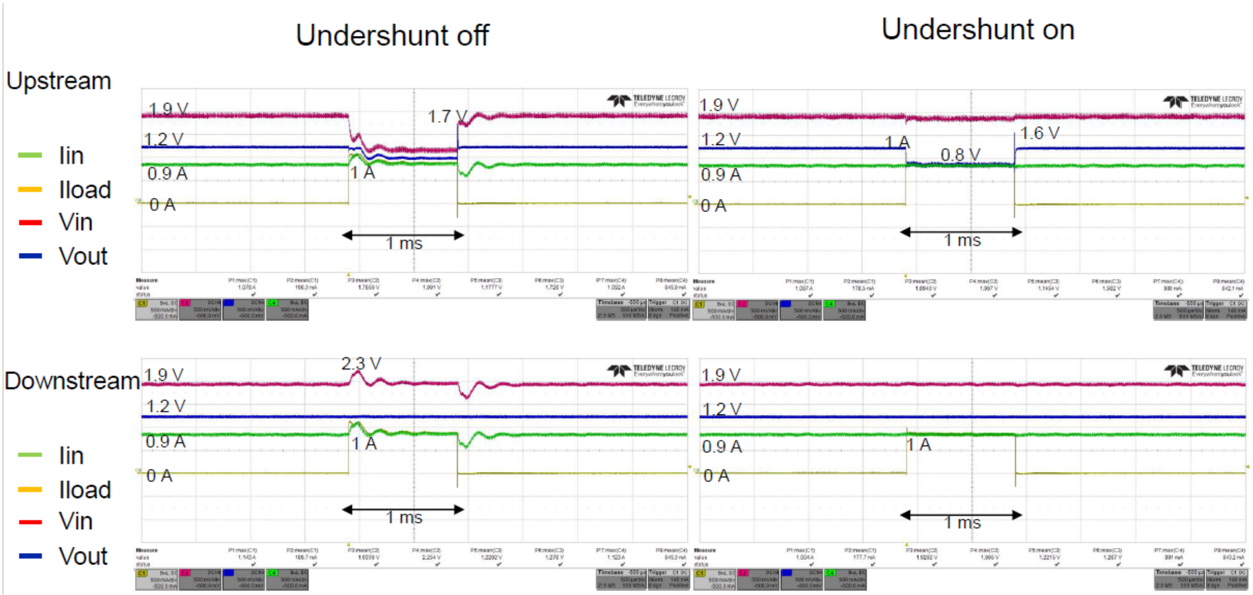

Figure 56: Oscilloscope images of the load pulse and its effects on the upstream (top) and downstream (bottom) chips in the case where the USP is inactive (left) or active (right). The action of the USP is particularly evident in the top-right image where the V_{out} decreases from 1.2 V to 0.8 V, allowing for a greater stability of the other measured values in the upstream and downstream modules (top-right and bottom-right respectively). Note that the load pulse is only injected into the upstream module, it is displayed in the downstream images simply for reference.

13.1.2 Parallel Test

Having determined the positive performance of the USP on a modules connected in series, it was decided to test its performance on chips connected in parallel. This is a circumstance that can present itself between chips in parallel within a module if one of these chips were to undergo a failure. In this case, the USP should reduce the voltage drop caused by one of the chains taking up more than its usual share of current due to an increased load.

This test was conducted by setting two chips in parallel and forcing one of the two (the "failing" chip) to fail by subjecting it to a 1.3 A load pulse of the length of 1 ms to simulate an unusually high current requirement taking current away from the remaining ("normal") chip. With 1.5 A being provided as overall current to the two modules, the load increase will channel 1.3 A towards the "failing" chip while only 0.2 A remain to the "normal" chip. A schematic of this experiment is shown in Figure 57.

As in the previous example, the experiment was conducted in two separate conditions, one where the USP was active and another where it was not. The monitored quantities were the same as in the previous section with the caveat that I_{in} here refers to the current passing through the module in question and not the total.

The results of these experiments are shown in Figure 58. These are dissimilar to the series case because the application of the USP manages to stabilize the voltages and current considered but in a much more limited fashion. In particular, it is worth noting that the V_{out} of the "normal" chip is always affected, regardless of USP application. This is not an especially significant effect but is concerning, especially in view of the possibility of multiple chains failing at the same time which could amplify the effect. However, the USP does not have a null effect as it is able to stabilize the required current pulse from 1300 mA in the off case to 1100 mA in the on case. This behavior shows that the USP, while being a useful tool for modules placed in series, is not as effective as desired when dealing with chips placed in parallel.

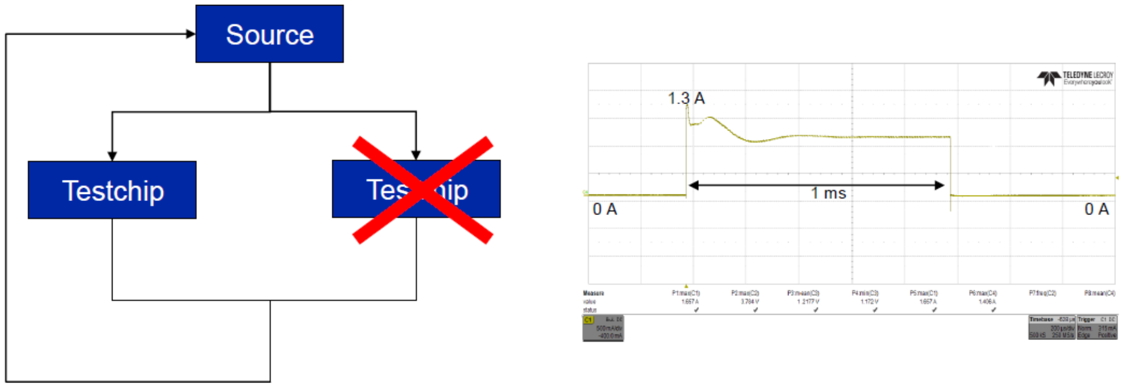

Figure 57: Schematic of the experimental setup (left) and oscilloscope image of the load pulse used to induce the failure of the upstream chip (right).

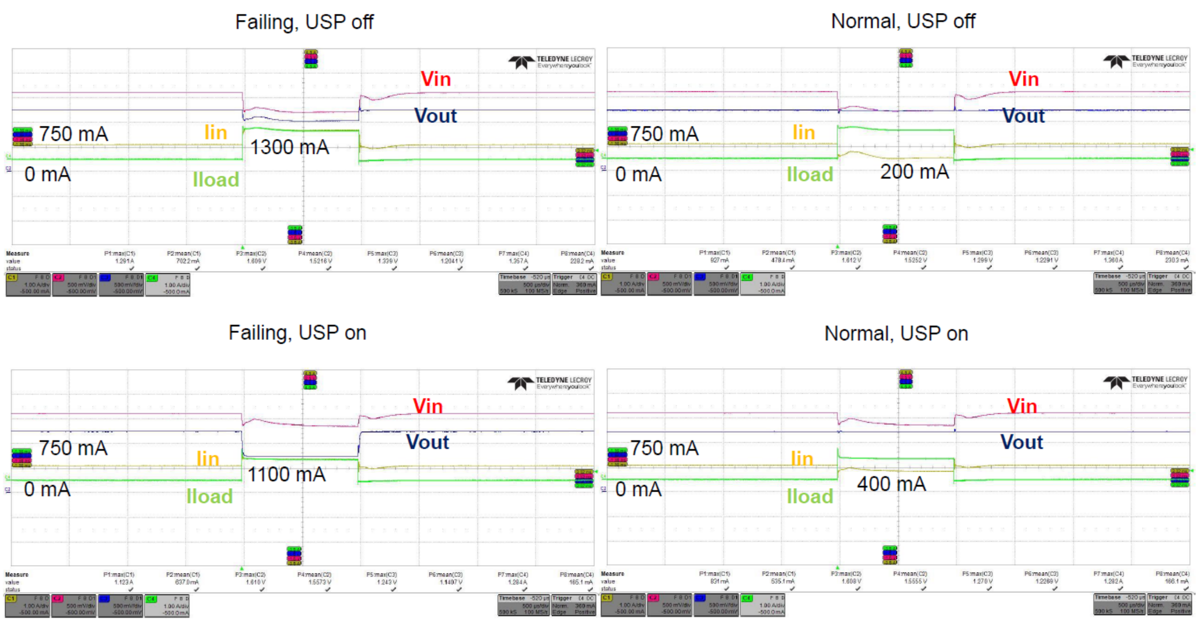

Figure 58: Oscilloscope images of the load pulse and its effects on the ”failing” (left) and ”normal” (right) chips in the case where the USP is inactive (top) or active (bottom). The USP allows for a greater stability of the measured values but less than in the series case. It is notable that V_{out} of the ”normal” chip is affected (though slightly) regardless of the presence or not of USP. Note that the load pulse is only injected into the ”failing” module, it is displayed in the ”normal” images just for reference.

13.2 Overvoltage Protection

Overvoltage protection has the primary role of limiting the maximum V_{in} provided by the Shunt so that it will always be ≤ 2 V and avoid damaging the readout chip. The voltage limit of the OVP is adjustable based on a given reference voltage though a fixed value will be chosen for the final chip model.

Similar tests to those for the USP were conducted to test the effectiveness of OVP in the parallel and serial configurations.

13.2.1 Parallel Test

The first test run was a variation of the previous parallel test. Here, rather than forcing one module to fail via a load pulse, a single chip was used and a square current wave was applied to simulate the current pulse due to the failure of a parallel chip. The current values were chosen specifically so that the V_{in} would exceed 2.0 V during the pulse but remain within operational values otherwise.

As previously, the test was conducted in the case where the OVP was active and in the case where it was not. The V_{in}, V_{out}, and I_{in} of the chip being tested were monitored with attention towards the stability of V_{out}.

The result of this test is shown in Figure 59. The first element of note is that the OVP successfully reduces the V_{in} from 2.2 V in the off case to 2.0 V in the on case with a brief transient of 2.1 V thus validating the basic function of the OVP. Furthermore, the V_{out} remains constant at the desired 1.2 V value in both cases considered. These two elements together indicate that a module provided with OVP will maintain function in the case of a parallel-chip failure and endure a dangerous V_{in} only for a fraction of a millisecond (something that can be avoided by setting a lower OVP limit).

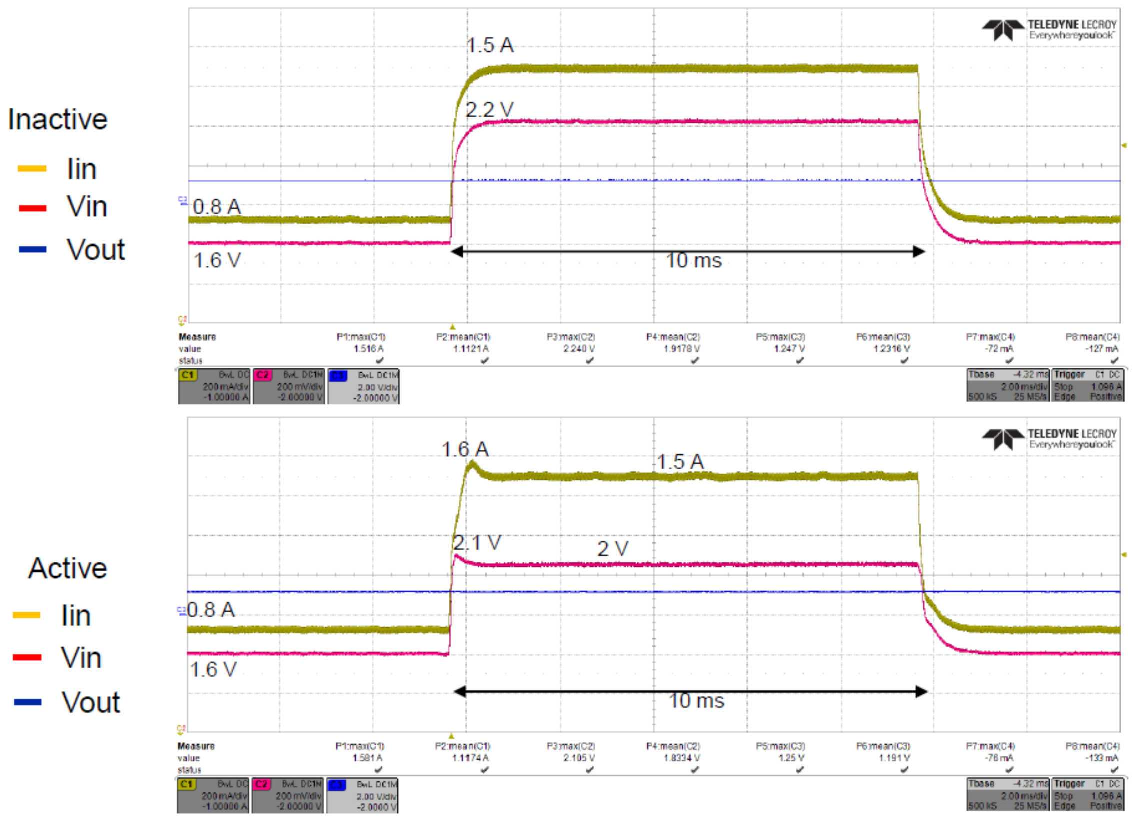

Figure 59: Oscilloscope images of the current pulse and its effects on the test module in the case where the OVP is inactive (top) or active (bottom). The effect of the OVP is evident in the lower image where V_{in} briefly exceeds the 2.0 V before returning to the recommended value as opposed to the inactive case in the upper image where the V_{in} climbs to 2.2 V unimpeded.

13.2.2 Series Test

Though the OVP was not designed to deal with the serial module chain, it was decided to test its behavior under this configuration, as was done for the USP.

The same setup as Section 13.1.1 was used with a 1 A load pulse causing an upstream chip to fail while the parameters of the downstream chip were measured.

The experiment was conducted in the case where the OVP was active and in the case where it was inactive. The V_{in}, V_{out}, I_{in}, and I_{load} of the chip were monitored with attention towards the stability of V_{out}.

The results of these tests are shown in Figure 60. In this case, it can be seen that the use of OVP stabilizes the V_{in} similarly to what was observed in Section 13.2.1. Unlike the USP case, there is still oscillation in the voltages and currents of the downstream chip, although the V_{in} does not exceed its safe value. However, it is important to notice that the V_{out} remains constant for the downstream chip, allowing it to operate normally despite the variation in V_{in}. The main gain from using the OVP is thus that the downstream chip does not suffer from a dangerous input voltage while remaining otherwise operational.

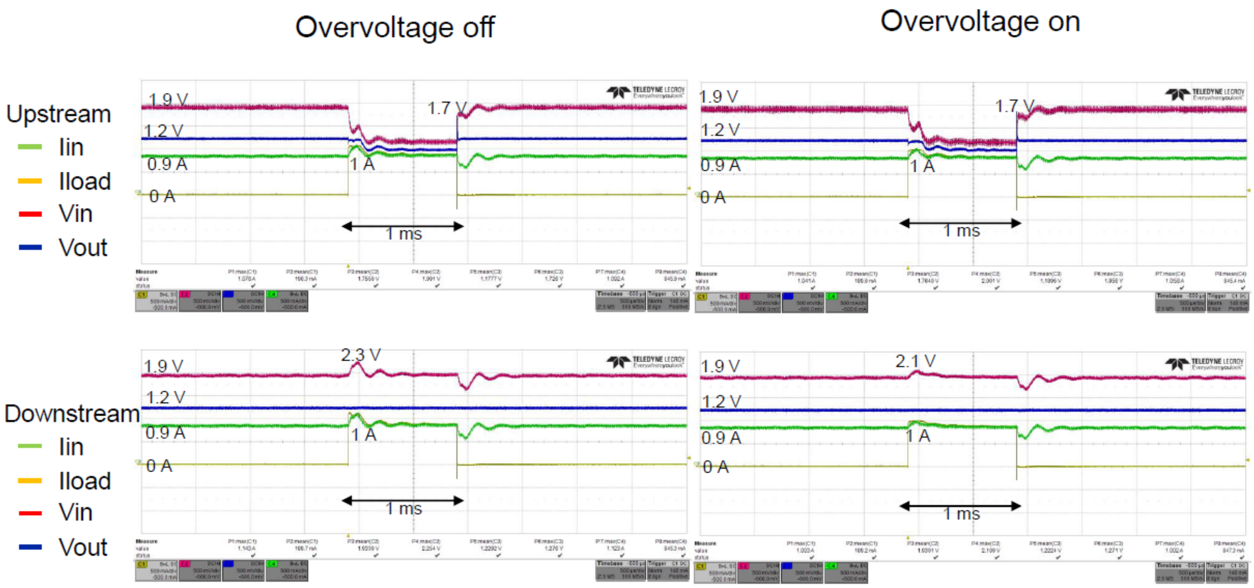

Figure 60: Oscilloscope images of the load pulse and its effects on the upstream (top) and downstream (bottom) chips in the case where the OVP is inactive (left) or active (right). The action of the OVP is visible in the bottom row where the V_{in} rises to a maximum of 2.3 V without OVP while it only reaches 2.1 V with OVP, stopping the module from being subjected to a dangerously high voltage. Note that the load pulse is only injected into the upstream module, it is displayed in the downstream images just for reference.

13.3 Comparison and Conclusions

The above studies on the undershunt and overvoltage protections have shown that each of them works properly within the context they were intended for but their performance outside that framework varies.

In particular, the USP was shown to effectively limit the fluctuations due to chip failure in a serial powering setup but this is no longer the case for parallel powering where the fluctuations remain sufficiently large as to affect the V_{out}, which could compromise the functioning of the module not directly affected by the failure.

The OVP instead performs its role in both configurations by limiting the maximum V_{in} to a pre-set value, thus limiting the possibility of damaging the module due to an excessive input voltage. In the serial powering case, the OVP does not stabilize the measured values to the extent that the USP does but the V_{out} remains constant at the operational value of 1.2 V if the V_{in} is maintained at a sufficiently high standard value (1.9 V in these tests).

Given these findings for the RD53A test-chip, it was decided to implement the OVP for the CMS Readout

Chip (CROC) while the USP was not selected. This is because the V_{out} has been shown to remain stable in the nominal chips under all the studied OVP failure conditions such that the main issue encountered was a dangerously high V_{in}. Given that the USP stabilizes the voltages in the serial powering case but does not do so for parallel powering it was deemed insufficient to deal with the different overload cases that can be encountered. On the other hand, the OVP successfully limits the V_{in} values to within expectations in all the cases studied and, with the V_{out} remaining constant, it allows for operation of the nominal modules in serial and parallel powering. For these reasons, the OVP was chosen to be included in the CROC.

14 Radiation Testing

Another significant issue that needs to be addressed by the new inner tracker is that it be sufficiently radiation-hard to survive the high-luminosity environment present in HL-LHC. This requirement was kept in consideration for the very first RD53 prototype and this chapter will describe the results of an irradiation campaign of the CMS Readout Chip (CROC), successor to the RD53A studied in Section 13.

The test performed involved the irradiation of the CROC with a nominal dose up to 1 Grad which is just under the expected dose for the first run of HL-LHC (1.2 Grad). Then a series of operational parameters were investigated throughout the duration of the experiment to monitor their behavior and whether or not the module could continue working after irradiation. While some variation is expected due to radiation damage, a suitably radiation-hard module will display a gradual change in behavior and still function.

Several different elements of the CROC were studied during the irradiation campaign. These are monitoring and trimming of key voltages (Section 14.2), study of the behavior of ring oscillators (Section 14.3), and behavior of the chip's Analog to Digital Converter (ADC) (Section 14.4).

The different chip voltages were monitored to study the overall effect that the irradiation can have on important internal values and how this can be addressed during the experiment. In particular the variation of V_{out} (the constant voltage which powers the pixel chip) should be considered and adjusted for.

The frequency of the ring oscillators is particularly sensitive to the radiation dose that has been received which makes them useful for the monitoring of the received dose during the experiment.

Finally, the ADC serves to convert the analog values to a digital value that can be read-out by a PC. However, the ADC must be properly calibrated to allow for a good correspondence between the digital output code and an analog voltage, but this calibration varies based on radiation dose.

14.1 Irradiation Campaign

The irradiation campaign of the CROC module was performed over the course of a month in an X-ray machine cooled to -30° C with a rate of 2.45 Mrad/h, managing to reach a total dose of 900 Mrad at the end of that period. An important caveat with regards to the irradiation dose is that the nominal value (which will be used in the following sections) does not correspond exactly to the equivalent dose that would be received in HL-LHC. This is because the material component of the module needs to be kept into account as it reduces the effective dose by 20%. Also, a relatively low hourly rate was chosen to better simulate the experimental conditions of a low sustained rate across several years.

The module was placed in the X-ray beam, ensuring that the chip bottom, where the elements being tested are found, would get a uniform dose. The irradiation map for the beam used can be seen in Figure 61 where the center of the chip bottom was placed in the (0,0) coordinates and extended along the Y axis with the rest of the chip extending in the negative X direction.

During the irradiation, the module was tested periodically with a series of specifically-developed scans relative to different elements of the chip. These tests were run with different frequencies based on the time required for each scan and the expected variation in each element.

Note that in the following sections there will be a clear discontinuity in data at approximately the 300 Mrad mark. This is due to a required re-calibration of the chip at that point, this did not affect the overall trends that were being observed but only introduce an offset.

14.2 Voltage Monitoring

One of the tests being run was the measurement of the key voltages of the module across the irradiation by means of an external multimeter. This was one of the more frequent tests with one measurement being performed approximately every 0.33 Mrad. Each of the voltages and currents (converted to a voltage via an internal resistor) of the chip were measured, but only a select few will be discussed since their behavior was comparable overall. Figure 62 shows the behavior of the $V_{ref,ADC}$ voltage throughout the irradiation period. An upward trend in voltage is evident and (if the 300 Mrad offset is taken into account) the overall increase is of approximately 100 mV. This behavior was also observed for the other voltages measured, with a roughly similar increase being encountered.

Mrad/h	-8.0	-6.0	-4.0	-2.0	0.0	2.0	4.0	X
10.0	0.59	0.65	0.71	0.75	0.79	0.80	0.52	
8.0	0.59	0.65	0.71	0.75	0.79	0.80	0.52	
6.0	0.60	0.66	0.71	0.76	0.79	0.84	0.49	
4.0	0.60	0.66	0.72	0.77	0.80	0.81	0.53	
2.0	0.61	0.66	0.72	0.77	0.81	0.82	0.53	
0.0	0.60	0.66	0.72	0.77	0.80	0.82	0.52	
-2.0	0.60	0.66	0.72	0.77	0.81	0.82	0.52	
-4.0	0.60	0.66	0.72	0.76	0.80	0.82	0.52	
-6.0	0.60	0.66	0.71	0.76	0.80	0.81	0.52	
-8.0	0.60	0.65	0.71	0.75	0.79	0.81	0.52	
-10.0	0.60	0.66	0.71	0.75	0.79	0.80	0.52	
Y								

Figure 61: Plot of the irradiation map used for the irradiation campaign. The center of the chip bottom was placed in the (0,0) coordinates with the rest of it extending along the $x = 0$ axis for 10 mm in both directions. This allows for a uniform irradiation along the area containing the elements being tested. All distances are given in mm. Note that the rate values reported in this matrix are the nominal case for a 10 mA current being used, in the experiment a 32 mA current was used to generate the X-rays, resulting in approximately three times the rate indicated.

This increase in voltage is an important element to consider in particular with regards to V_{out}, i.e. the voltage required to power the pixel chip. Since this voltage needs to remain at a constant 1.2 V, it becomes necessary to modify it as irradiation progresses to ensure it remains approximately at the desired level. This can be achieved remotely with the use of trimming-bits that can shift this voltage up or down in increments of approximately 20 mV per bit. Note that the CROC has two different voltages of this type (VDDD and VDDA) which respectively power the digital and analog pixel components of the CROC.

The correct trimming value for each of these voltages is obtained by briefly cycling through all the available trimming-bits and selecting the one that gives the closest value to the desired 1.2 V. The value so selected is the one that will be used until the next trimming. However, the values displayed in this section are not integers, because the voltage values for each trimming-bit are stored and a linear fit is performed from which the "ideal" trimming-bit is extracted, this corresponds to the bit for which exactly 1.2 V are expected.

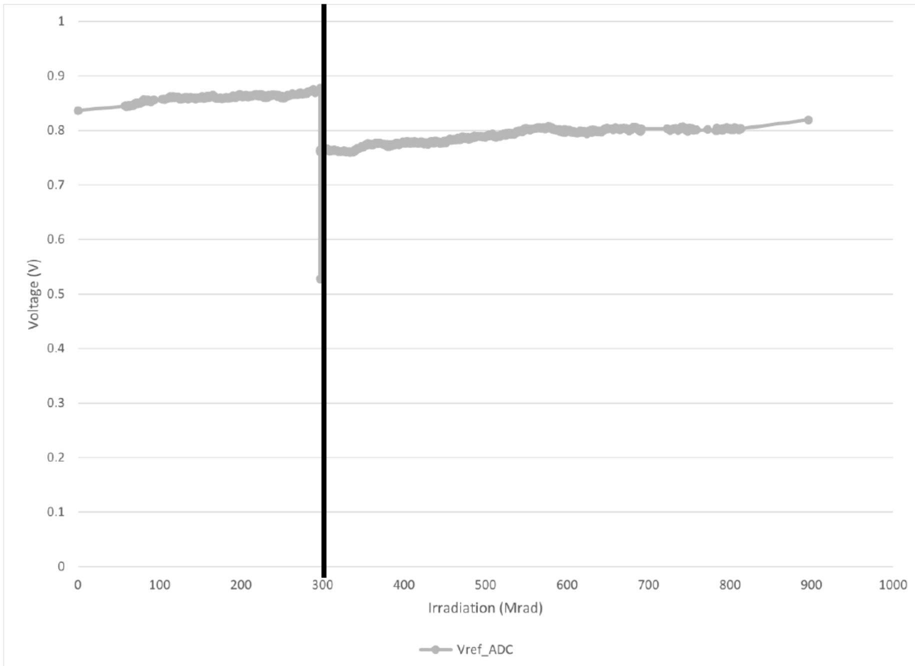

Figure 62: Plot of the $V_{ref,ADC}$ voltage during the irradiation period. The effect of irradiation can be seen in the overall increase in voltage amounting to approximately 100 mV. The other voltages measured resulted in a comparable result. The interruption at 300 Mrad is due to a re-calibration of the chip and introduces an offset in the voltage, this is indicated by the black line.

This allows for the study of smaller trends that would escape a simple observation of the discrete bit being selected. This trimming is one of the more infrequent operations and is performed only approximately every 50 Mrad.

The results of trimming during the irradiation campaign are summarized in Figure 63. These findings match what was discussed previously about the increase in voltage with irradiation: since the voltage increases, the trimming-bits need to be lowered to return to the desired 1.2 V. It is also notable that the VDDD and VDDA behave similarly but not the same way since the VDDA requires lower bits than the VDDD. This behavior was reported to the CROC designers and corresponded to previous observations.

14.3 Ring Oscillator Behavior

Another element monitored during irradiation is that of the ring oscillators. A ring oscillator is a device composed of an odd number of logic gates in a ring with an output that oscillates between two voltage levels at a given frequency. They are disconnected from the above-mentioned voltages and are used to independently determine the radiation dose received by the module. With the increase in radiation dose, it is expected that the frequency of oscillation will decrease in a predicable manner, which allows for a remote measurement of the radiation dose received by the chip. The CROC is provided with a 42 ring oscillators built using different logic cells that affect their performance, this is done as a cross-check between different ring oscillator structures and to evaluate the performance of these oscillators for the final version of the readout chip. Note that this frequency also depends on the VDDD discussed in the previous section, providing a further reason to keep VDDD constant.

During the irradiation campaign the ring oscillators were studied by measuring the number of cycles (counts) they managed to complete within a 1 ms period. This measurement was performed approximately every 0.33 Mrad, just after the voltage measurements The number of counts for each oscillator was recorded but only one of the four oscillator banks will be shown as it is representative of the general behavior observed. Furthermore, for display purposes, the counts were not reported directly but rather the ratio of the measured

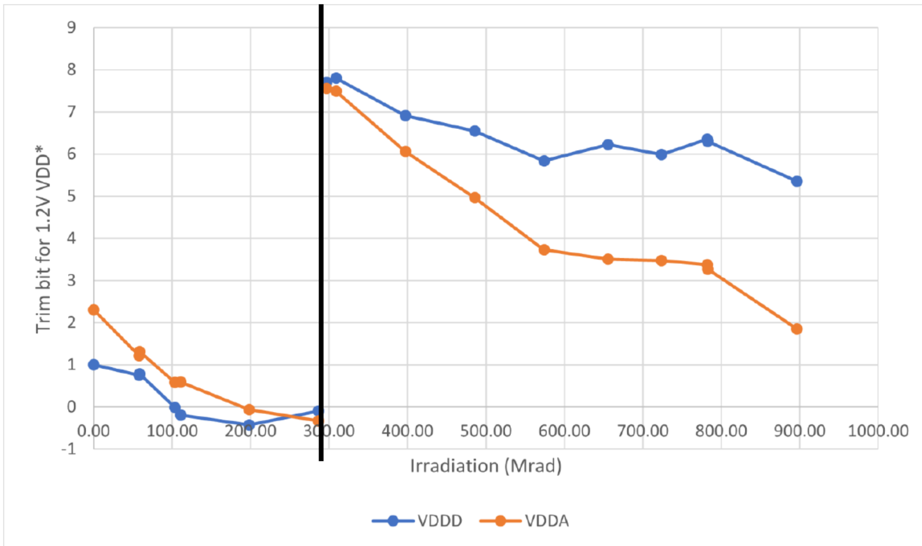

Figure 63: Plot of the VDDD and VDDA voltage trimming during the irradiation period. The effect of irradiation can be seen in the overall decrease in trimming-bits for both voltages. VDDA requires lower bits than VDDD, this is a known effect for the designers. The interruption at 300 Mrad is due to a re-calibration of the chip and introduces an offset in the voltage, this is indicated by the black line.

number of counts to the maximum number of counts registered.

Figure 64 shows the performance of eight different ring oscillators during the irradiation period. An overall decrease in the number of counts is visible for all the oscillators being studied. The different types of oscillator vary in their behavior with a $40-80\%$ decrease from the original value, if one considers the offset at 300 Mrad. If the effect of the offset is excluded, the last 600 Mrad of irradiation cause a $15-65\%$ drop. This effect matches the expectations for the ring oscillator performance and allows for an independent estimation of the radiation dose received by the module. Since the decreasing trend with irradiation was observed to be roughly linear, this permits a calculation of the dose received as a function of the number of counts measured.

14.4 ADC Calibration

The Analog to Digital Converter (ADC) of the CROC serves to digitize the analog voltages provided by the chip in order to render them legible by a PC. The ADC thus provides a series of numerical codes to the PC but their equivalence to a voltage needs to be calibrated beforehand to allow for a proper conversion back from code to a human-legible voltage. However, like with the other elements studied, this calibration changes with irradiation so a new one must be taken periodically to ensure a proper conversion can be made. Furthermore, it is important to check whether the equivalence between code and voltage remains linear throughout irradiation or if this relation breaks down after a certain dose.

The ADC calibration process is performed by taking two separate but contemporaneous measurements of a given voltage after it has been set to a certain value via an internal Digital to Analog Converter (DAC). On the one hand, the ADC code of the chosen voltage is measured and stored while, on the other, the chosen voltage is measured directly by an external multimeter which then relays its information to the computer. The two measured values are then associated and compared. This process is repeated for a range of different voltages in order to provide a good estimate of the linearity for all the possible codes. Once the data has been collected, a linear fit is performed and the slope and intercept of this fit are stored for future use. An example of this process performed on a stable un-irradiated chip can be seen in Figure 65.

Figure 66 shows the evolution of the calibration for a selection of different radiation doses. It is evident that the relation between ADC code and voltage remains linear regardless of the dose and remains roughly consistent in its inclination. This means that, throughout the chip's operation, it will be possible to properly

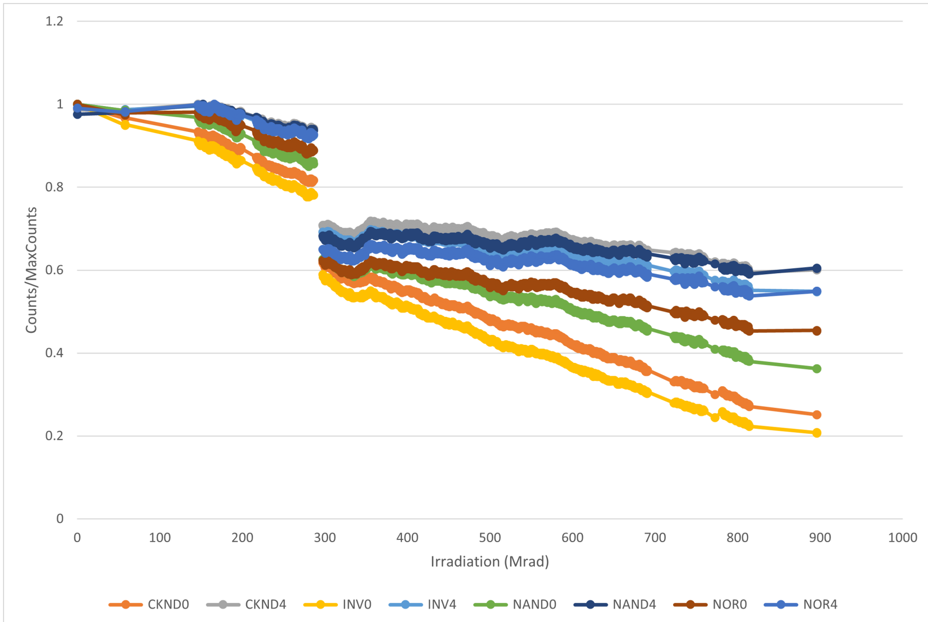

Figure 64: Plot of the change in the measured number of cycles (counts) within a 1 ms period with irradiation. Rather than showing the counts directly, the plot indicates the ratio of the measured number of counts to the maximum number of counts registered for each oscillator The effect of irradiation can be seen in the overall decrease in counts; different oscillators are affected more or less by the same dose. The other oscillators studied resulted in a comparable result. The interruption at 300 Mrad is due to a re-calibration of the chip and introduces an offset in the voltage, this is indicated by the black line.

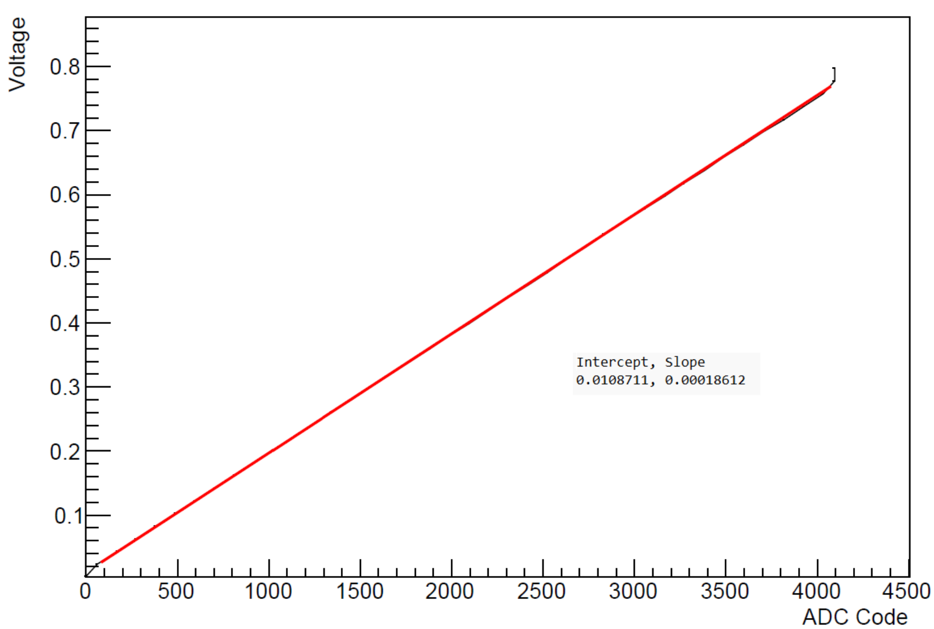

Figure 65: Plot of an example ADC calibration for an un-irradiated chip. The intercept and slope of the fit are displayed on the plot. Note that, in this case, the ADC code saturates at 4096.

calibrate the ADC conversion and read the internal values of the CROC directly through the PC.

Though the linearity remains as expected, it is interesting to study the slope and intercept values of

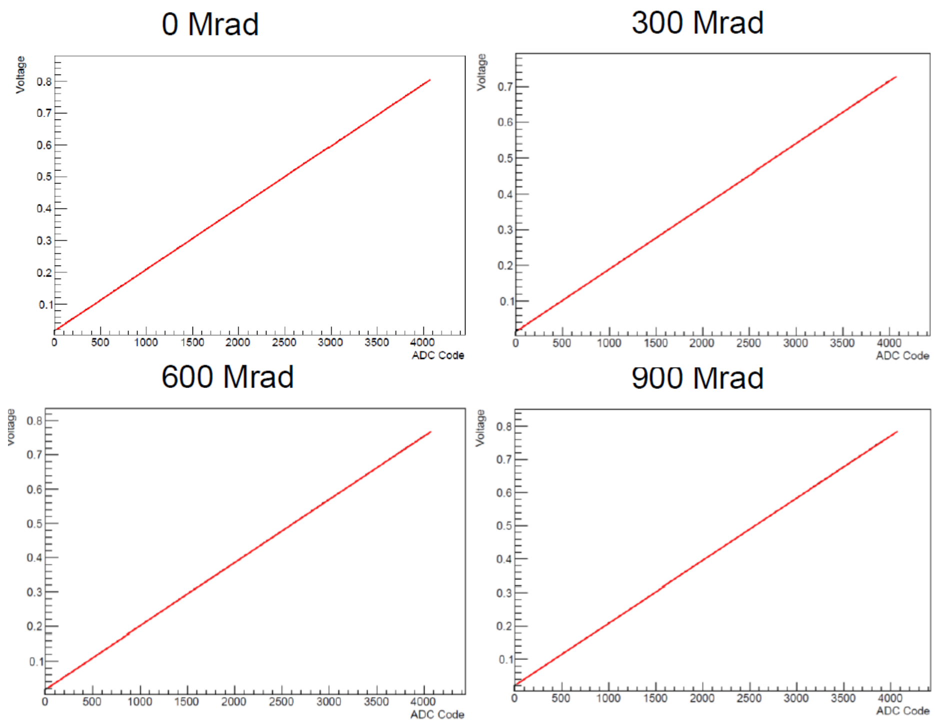

Figure 66: Plots of four different ADC calibrations at different radiation doses. The relationship between ADC code and voltage remains linear for every dose measured.

the ADC calibration to study how they evolve with irradiation. Figure 67 displays the values of slope and intercept throughout the irradiation campaign. An overall increase can be noted for both values with the slope in particular increasing by approximately 10%. This matches previous studies on the matter where the effect of the intercept was relatively negligible for most voltages while the slope provided most of the variation. This result also indicates that it would be possible to use the initial calibration for measurements during operation if one takes the uncertainty from this 10% variation into account.

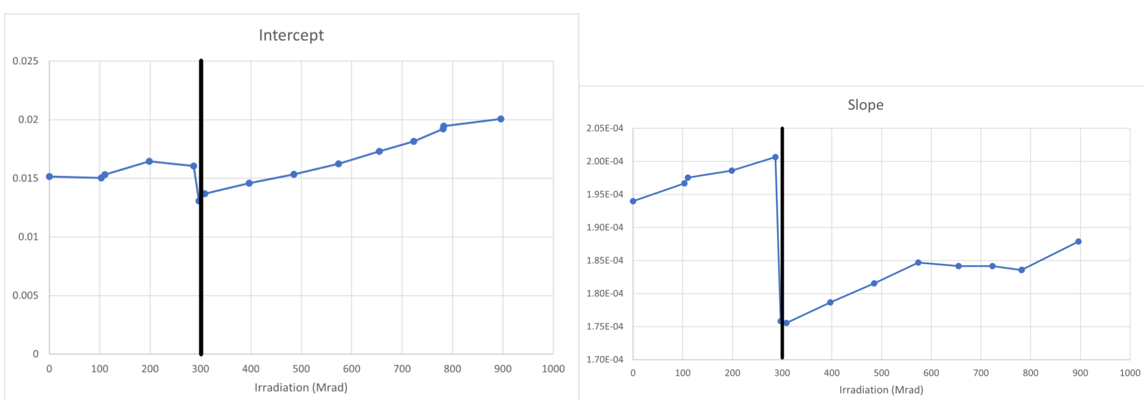

Figure 67: Plots displaying the evolution of the intercept (left) and slope (right) in the ADC calibration. Both slope and intercept increase with radiation dose in a manner compatible to what was observed in previous studies. The interruption at 300 Mrad is due to a re-calibration of the chip and introduces an offset in the voltage, this is indicated by the black line.

14.5 Summary

The radiation studies performed confirm the proper operation of the CMS Readout Chip even under radiation doses comparable to what will be present during HL-LHC operation. The main variation noticed was an overall increase in the measured internal voltages with dose. This was dealt with for the voltages powering the pixel chip via a periodic trimming to maintain a constant value of 1.2 V. Another variation observed was that of the ADC calibration whose slope varies by about 10% between beginning and end of the irradiation. This allows for a general rough estimate if a new calibration is unavailable, though that remains the preferred method for a precise conversion. Finally, the ring oscillators performed according to expectation with an overall decrease in frequency with irradiation with the magnitude varying between different oscillators

These results prove the feasibility of this type of chip for the high-radiation environment of HL-LHC. The conclusions were presented to the RD53 collaboration which then proceeded to make preparations for the final version of the CROC.

15 Conclusions and Outlook

This thesis presented a measurement of the cross-section of the $t\bar{t}b\bar{b}$ process in the semileptonic decay mode. The analysis was performed with 138fb^{-1} of proton-proton collision data from the CMS experiment at a center-of-mass-energy of 13TeV. Measurement of the differential and inclusive cross-section is key to improve our knowledge of the Standard Model due to its role as background for the $t\bar{t}H$ process with $H \to b\bar{b}$, potential as BSM background, and its importance towards the validation of theoretical calculations. This last point, in particular, is meaningful as it serves to validate the recent underprediction of $t\bar{t}b\bar{b}$ by current models and provide the information necessary to improve those same predictions within the SM frame.

The analysis managed to achieve measurements of both the inclusive and differential cross-sections of the $t\bar{t}b\bar{b}$ process in four different phase spaces that target different behaviors of $t\bar{t}b\bar{b}$. The inclusive measurements so obtained were the most precise ones yet for this process, which amounts to uncertainties between 5 and 11% where the uncertainties were primarily due to systematic sources such as the b-tagging calibration. The measurements of the differential cross-section were obtained as a function of several different observables which were chosen to target light-jet radiation and b jets, first among which were the "additional b-jets" not derived from top decay. By comparing the differential measurements to a series of different event generators, it was possible to evaluate their performance and determine that no one generator can properly describe all the observables studies in the respective phase spaces.

The measurements of $t\bar{t}b\bar{b}$ production performed in this study, with their improved precision, will serve as a useful tool for the improvement of SM predictions, allowing for a better understanding of the uncertainties and expectations of the process which, in turn, will aid future studies where $t\bar{t}b\bar{b}$ plays an important role.

Many future studies can be performed to improve the precision of this measurement. Within the same $t\bar{t}b\bar{b}$ process, a better understanding of the main systematic uncertainties would allow for a clearer picture of the process with a reduction in the uncertainty on the differential and inclusive cross-sections. An alternative but complementary study could also be the investigation of other decay modes, in particular the fully hadronic decay mode. By developing improvements to the jet identification and reconstruction, this mode produced at a higher branching ratio should be able to provide more information on the $t\bar{t}b\bar{b}$ process that can be combined with that of the semileptonic studies. Another means of improving the precision of these measurements is the use of larger future datasets whether it be those of Run3 currently ongoing or the future HL-LHC.

The technical requirements for the collection of data during HL-LHC imply the need for a new inner tracker with new pixel chips. This thesis covered studies on the behavior of these new CMS chips that account for the high rate of events expected.

The tests on undershunt and overvoltage protections showed that each of them is best suited to its design context but the overvoltage protection is the only one that fulfils its role in both serial and parallel powering, making it the one chosen for implementation in the CROC. The radiation studies then confirmed that the readout chip can continue operating as intended despite a high radiation dose which is comparable to that which will be encountered during the running of HL-LHC. Together, these results proved the effectiveness of the CMS readout chip in a high-radiation environment and allowed for the advancement of the chip prototypes to the final production stages.

To summarize, motivated by the $t\bar{t}b\bar{b}$ process' role as background to SM processes and validation of theoretical calculations, this thesis presents the most precise measurement of both the inclusive and differential cross-sections of the $t\bar{t}b\bar{b}$ process in the semileptonic decay mode with the use of four phase spaces that target different behaviors of $t\bar{t}b\bar{b}$. This measurement, together with others ongoing and planned for Run3 and HL-LHC will contribute to the refinement of theoretical predictions and help to limit the theoretical uncertainties for the available $t\bar{t}b\bar{b}$ generators.

References

[1] CMS Collaboration. "Observation of a New Boson at a Mass of 125 GeV with the CMS Experiment at the LHC". In: *Phys. Lett.* B716 (2012), pp. 30–61. DOI: 10.1016/j.physletb.2012.08.021. arXiv: 1207.7235 [hep-ex].

[2] "Observation of a new particle in the search for the Standard Model Higgs boson with the ATLAS detector at the LHC". In: *Phys. Lett.* B716 (2012), pp. 1–29. DOI: 10.1016/j.physletb.2012.08.020. arXiv: 1207.7214 [hep-ex].

[3] Chatrchyan et al. "The CMS experiment at the CERN LHC. The Compact Muon Solenoid experiment". In: *JINST* 3 (2008). Also published by CERN Geneva in 2010, S08004. 361 p. DOI: 10.1088/1748-0221/3/08/S08004. URL: https://cds.cern.ch/record/1129810.

[4] Ed. by Lyndon Evans and Philip Bryant. "LHC Machine". In: *JINST* 3 (2008). DOI: 10.1088/1748-0221/3/08/S08001.

[5] D.J. Warner (Ed.) "Project study for a new 50 MeV linear accelerator for the CPS". In: (1973). URL: http://cdsweb.cern.ch/record/414071.

[6] L Arnaudon et al. "Linac4 Technical Design Report". In: (Jan. 2006).

[7] K H Reich. "The CERN proton synchrotron booster". In: (1969). URL: https://cds.cern.ch/record/349912.

[8] Edouard Regenstreif. *The CERN Proton Synchrotron.* CERN Yellow Reports: Monographs. French version published as CERN 58-06. Geneva: CERN, 1959. DOI: 10.5170/CERN-1959-029. URL: http://cds.cern.ch/record/214352.

[9] Julie Coupard et al. *LHC Injectors Upgrade, Technical Design Report.* Tech. rep. Geneva: CERN, 2016. DOI: 10.17181/CERN.L6VM.UOMS. URL: https://cds.cern.ch/record/2153863.

[10] Carlo Wyss. *LEP design report, v.3: LEP2.* Vol. 1-2 publ. in 1983-84. Geneva: CERN, 1996. URL: https://cds.cern.ch/record/314187.

[11] Jorg Wenniger. "Observation of a New Boson at a Mass of 125 GeV with the CMS Experiment at the LHC". In: *Comptes Rendus Physique* 16 (2015), pp. 347–355. DOI: 10.1016/j.crhy.2015.03.005.

[12] "ATLAS: technical proposal for a general-purpose pp experiment at the Large Hadron Collider at CERN". In: (). URL: http://cdsweb.cern.ch/record/290968.

[13] "CMS technical proposal". In: (). URL: http://cdsweb.cern.ch/record/290969.

[14] "LHCb technical proposal". In: (). URL: http://cdsweb.cern.ch/record/622031.

[15] W. Kienzle et al. "TOTEM, Total cross section, elastic scattering and diffractive dissociation at the LHC: Technical Proposal". In: (). URL: http://cdsweb.cern.ch/record/385483.

[16] "ALICE: Technical proposal for a Large Ion collider Experiment at the CERN LHC". In: (). URL: http://cdsweb.cern.ch/record/293391.

[17] David Barney. "CMS Detector Slice". In: ().

[18] G. Apollinari et al. "High-Luminosity Large Hadron Collider (HL-LHC)". In: *CERN Yellow Rep. Monogr.* 4 (2017), p. 1. DOI: 10.23731/CYRM-2017-004.

[19] Izaak Neutelings. *CMS coordinate system.* https://tikz.net/axis3d_cms/. Accessed: 2022-09-02.

[20] Serguei Chatrchyan et al. "Description and performance of track and primary vertex reconstruction with the CMS tracker". In: *JINST* 9 (2014), P10009. DOI: 10.1088/1748-0221/9/10/P10009. arXiv: 1405.6569 [physics.ins-det].

[21] CMS Collaboration. "The CMS Phase-1 Pixel Detector Upgrade". In: *JINST* 16 (2021), P2027. DOI: 10.1088/1748-0221/16/02/P2027. arXiv: 2012.14304 [physics.ins-det].

[22] CMS Collaboration. "Precision measurement of the structure of the CMS inner tracking system using nuclear interactions". In: (July 2018).

[23] A. Benaglia. "The CMS ECAL performance with examples". In: *JINST* 9 (2014), p. C02008.

[24] CMS Collaboration. "Calibration of the CMS hadron calorimeters using proton-proton collision data at $\sqrt{s} = 13$TeV". In: *JINST* 14, 12 (Sept. 2019), p. C12010. arXiv: 1912.06178 [hep-ex].

[25] A. M. Sirunyan et al. "Performance of the CMS muon detector and muon reconstruction with proton-proton collisions at $\sqrt{s} = 13$TeV". In: *JINST* 13.06 (2018), P06015. DOI: 10.1088/1748-0221/13/06/P06015. arXiv: 1804.04528 [physics.ins-det].

[26] G. Abbiendi et al. "Study of the effects of radiation on the CMS Drift Tubes Muon Detector for the HL-LHC". In: (Dec. 2019). DOI: 10.1088/1748-0221/14/12/C12010. arXiv: 1910.00079v1 [hep-ex].

[27] S. L. Glashow. "Partial Symmetries of Weak Interactions". In: *Nucl. Phys.* 22 (1961). DOI: 10.1016/0029-5582(61)90469-2..

[28] Gerard 't Hooft and M. J. G. Veltman. "Regularization and Renormalization of Gauge Fields". In: *Nucl. Phys.* B44 (1972), pp. 189–213. DOI: 10.1016/0550-3213(72)90279-9..

[29] Abdus Salam. "Weak and Electromagnetic Interactions". In: *Conf. Proc.* C680519 (1968), pp. 367–377. DOI: 10.1142/9789812795915_0034..

[30] Steven Weinberg. "A Model of Leptons". In: *Phys. Rev. Lett.* 19 (1967), pp. 1264–1266. DOI: 10.1103/PhysRevLett.19.1264.. URL: https://link.aps.org/doi/10.1103/PhysRevLett.19.1264..

[31] R. P. Feynman. "Mathematical Formulation of the Quantum Theory of Electromagnetic Interaction". In: *Physical Review* 80.3 (Nov. 1950), pp. 440–457. DOI: 10.1103/PhysRev.80.440.

[32] L. Maiani S. L. Glashow J. Iliopoulos. "Weak Interactions with Lepton- Hadron Symmetry". In: *Phys. Rev. D* 2 (1970), pp. 1285–1292. DOI: 10.1103/PhysRevD.2.1285.. URL: https://link.aps.org/doi/10.1103/PhysRevD.2.1285..

[33] C. N. Yang and R. L. Mills. "Conservation of Isotopic Spin and Isotopic Gauge Invariance". In: *Physical Review* 96.1 (Oct. 1954), pp. 191–195. DOI: 10.1103/PhysRev.96.191.

[34] H. Fritzsch, M. Gell-Mann, and H. Leutwyler. "Advantages of the color octet gluon picture". In: *Physics Letters B* 47.4 (Nov. 1973), pp. 365–368. DOI: 10.1016/0370-2693(73)90625-4.

[35] L Lönnblad et al. "Monte Carlo generators". In: 36 (Jan. 2004).

[36] Patrignani et al. "Review of Particle Physics, 2016-2017". In: *Chin. Phys. C* 40 (2016), 100001. 1808 p. DOI: 10.1088/1674-1137/40/10/100001. URL: https://cds.cern.ch/record/2241948.

[37] *SM Higgs Branching Ratios and Total Decay Widths.* https://twiki.cern.ch/twiki/bin/view/LHCPhysics/CERNYellowReportPageBR. Accessed: 2022-10-27.

[38] A. M. Sirunyan et al. "Combined measurements of Higgs boson couplings in proton–proton collisions at $\sqrt{s} = 13TeV$". In: *The European Physical Journal C* 79.5 (May 2019). DOI: 10.1140/epjc/s10052-019-6909-y. URL: https://doi.org/10.1140%5C%2Fepjc%5C%2Fs10052-019-6909-y.

[39] F. Abe et al. "Observation of top quark production in $\bar{p}p$ collisions". In: *Phys.Rev. Lett.* 74 (1995), pp. 2626–2631. DOI: 10.1103/PhysRevLett.74.2626..

[40] S. Abachi et al. "Observation of the top quark". In: *Phys.Rev. Lett.* 74 (1995), pp. 2632–2637. DOI: 10.1103/PhysRevLett.74.2632..

[41] *Top-pair production cross-section at 7 TeV.* https://twiki.cern.ch/twiki/bin/view/LHCPhysics/TopPairCrossection7TeVHistory. Accessed: 2022-06-23.

[42] A.A. Petrukhin. "NEVOD–DECOR experiment and evidences for quark–gluon plasma in cosmic rays". In: *Nuclear Instruments and Methods in Physics Research Section A: Accelerators, Spectrometers, Detectors and Associated Equipment* 692 (2012). 3rd Roma International Conference on Astroparticle Physics, pp. 228–232. ISSN: 0168-9002. DOI: https://doi.org/10.1016/j.nima.2011.12.074. URL: https://www.sciencedirect.com/science/article/pii/S0168900211023084.

[43] *Useful Diagrams of Top Signals and Backgrounds.* https://www-d0.fnal.gov/Run2Physics/top/top_public_web_pages/top_feynman_diagrams.html. Accessed: 2022-06-23.

[44] S. W. Herb et al. "Observation of a Dimuon Resonance at 9.5 GeV in 400-GeV Proton-Nucleus Collisions". In: *Phys. Rev. Lett.* 39 (5 Aug. 1977), pp. 252–255. DOI: 10.1103/PhysRevLett.39.252. URL: https://link.aps.org/doi/10.1103/PhysRevLett.39.252.

[45] *B tagging jets*. https://tikz.net/jet_btag/. Accessed: 2022-06-23.

[46] M. Aaboud et al. "Search for the standard model Higgs boson produced in association with top quarks and decaying into a $b\bar{b}$ pair in pp collisions at $\sqrt{s} = 13$TeV with the ATLAS detector". In: *Physical Review D* 97.7 (Apr. 2018). DOI: 10.1103/physrevd.97.072016. URL: https://doi.org/10.1103%5C%2Fphysrevd.97.072016.

[47] *Search for ttH production in the H-to-bb decay channel with leptonic tt decays in proton-proton collisions at sqrt(s) = 13 TeV with the CMS detector*. Tech. rep. Geneva: CERN, 2018. URL: https://cds.cern.ch/record/2308267.

[48] Federico Buccioni et al. "NLO QCD predictions for $t\bar{t}b\bar{b}$ production in association with a light jet at the LHC". In: *Journal of High Energy Physics* 2019.12 (Dec. 2019). DOI: 10.1007/jhep12(2019)015. URL: https://doi.org/10.1007%5C%2Fjhep12%5C%282019%5C%29015.

[49] A.M. Sirunyan et al. "Measurements of $t\bar{t}$ cross sections in association with b jets and inclusive jets and their ratio using dilepton final states in pp collisions at $sqrt(s) = 13$TeV". In: *Physics Letters B* 776 (Jan. 2018), pp. 355–378. DOI: 10.1016/j.physletb.2017.11.043. URL: https://doi.org/10.1016%5C%2Fj.physletb.2017.11.043.

[50] M. Aaboud et al. "Measurements of inclusive and differential fiducial cross-sections of $t\bar{t}$ production with additional heavy-flavour jets in proton-proton collisions at s $\sqrt{s} = 13TeV$ with the ATLAS detector". In: *Journal of High Energy Physics* 2019 (Apr. 2019). DOI: 10.1007/JHEP04(2019)046.

[51] Stefan Höche et al. "Next-to-leading order QCD predictions for top-quark pair production with up to two jets merged with a parton shower". In: *Phys. Lett. B* 748 (2015), p. 74. DOI: 10.1016/j.physletb.2015.06.060. arXiv: 1402.6293 [hep-ph].

[52] M. V. Garzelli, A. Kardos, and Z. Trócsányi. "Hadroproduction of $ttbb$ final states at LHC: predictions at NLO accuracy matched with Parton Shower". In: *JHEP* 03 (2015), p. 083. DOI: 10.1007/JHEP03(2015)083. arXiv: 1408.0266 [hep-ph].

[53] Stefan Höche et al. "Next-to-leading order QCD predictions for top-quark pair production with up to three jets". In: *Eur. Phys. J. C* 77 (2017), p. 145. DOI: 10.1140/epjc/s10052-017-4715-y. arXiv: 1607.06934 [hep-ph].

[54] J. Alwall et al. "The automated computation of tree-level and next-to-leading order differential cross sections, and their matching to parton shower simulations". In: *JHEP* 07 (2014), p. 079. DOI: 10.1007/JHEP07(2014)079. arXiv: 1405.0301 [hep-ph].

[55] Rikkert Frederix and Stefano Frixione. "Merging meets matching in MC@NLO". In: *JHEP* 12 (2012), p. 061. DOI: 10.1007/JHEP12(2012)061. arXiv: 1209.6215 [hep-ph].

[56] Stefano Frixione, Paolo Nason, and Giovanni Ridolfi. "A Positive-weight next-to-leading-order Monte Carlo for heavy flavour hadroproduction". In: *JHEP* 09 (2007), p. 126. DOI: 10.1088/1126-6708/2007/09/126. arXiv: 0707.3088 [hep-ph].

[57] Fabio Cascioli et al. "NLO matching for $ttbb$ production with massive b-quarks". In: *Phys. Lett. B* 734 (2014), p. 210. DOI: 10.1016/j.physletb.2014.05.040. arXiv: 1309.5912 [hep-ph].

[58] G. Bevilacqua, M. V. Garzelli, and A. Kardos. "$ttbb$ hadroproduction with massive bottom quarks with PowHel". 2017. arXiv: 1709.06915 [hep-ph].

[59] Tomáš Sežo et al. "New NLOPS predictions for $tt + b$-jet production at the LHC". In: *Eur. Phys. J. C* 78 (2018), p. 502. DOI: 10.1140/epjc/s10052-018-5956-0. arXiv: 1802.00426 [hep-ph].

[60] Albert M Sirunyan et al. "Measurement of the cross section for $t\bar{t}b\bar{b}$ production with additional jets and b jets in pp collisions at $\sqrt{s} = 13$TeV". In: *JHEP* 07 (2020), p. 125. DOI: 10.1007/JHEP07(2020)125. arXiv: 2003.06467 [hep-ex].

[61] Vardan Khachatryan et al. “Measurement of the cross section ratio $\sigma_{ttbb}/\sigma_{\mathrm{ttjj}}$ in pp collisions at $\sqrt{s} = 8\mathrm{TeV}$”. In: *Phys. Lett. B* 746 (2015), p. 132. DOI: 10.1016/j.physletb.2015.04.060. arXiv: 1411.5621 [hep-ex].

[62] Paolo Nason. “A new method for combining NLO QCD with shower Monte Carlo algorithms”. In: *JHEP* 11 (2004), p. 040. DOI: 10.1088/1126-6708/2004/11/040. arXiv: hep-ph/0409146 [hep-ph].

[63] Stefano Frixione, Paolo Nason, and Carlo Oleari. “Matching NLO QCD computations with parton shower simulations: the POWHEG method”. In: *JHEP* 11 (2007), p. 070. DOI: 10.1088/1126-6708/2007/11/070. arXiv: 0709.2092 [hep-ph].

[64] Simone Alioli et al. “A general framework for implementing NLO calculations in shower Monte Carlo programs: the POWHEG BOX”. In: *JHEP* 06 (2010), p. 043. DOI: 10.1007/JHEP06(2010)043. arXiv: 1002.2581 [hep-ph].

[65] Simone Alioli et al. “NLO single-top production matched with shower in POWHEG: s- and t-channel contributions”. In: *JHEP* 09 (2009). [Erratum], p. 111. DOI: 10.1088/1126-6708/2009/09/111. arXiv: 0907.4076 [hep-ph].

[66] Emanuele Re. “Single-top W t-channel production matched with parton showers using the POWHEG method”. In: *Eur. Phys. J. C* 71 (2011), p. 1547. DOI: 10.1140/epjc/s10052-011-1547-z. arXiv: 1009.2450 [hep-ph].

[67] Heribertus B. Hartanto et al. “Higgs boson production in association with top quarks in the POWHEG BOX”. In: *Phys. Rev. D* 91 (2015), p. 094003. DOI: 10.1103/PhysRevD.91.094003. arXiv: 1501.04498 [hep-ph].

[68] Young Kwon Jo et al. “Study of the top-quark pair production in association with a bottom-quark pair from fast simulations at the LHC”. In: *Journal of the Korean Physical Society* 67.5 (Sept. 2015), pp. 807–812. DOI: 10.3938/jkps.67.807. URL: https://doi.org/10.3938%5C%2Fjkps.67.807.

[69] Georges Aad et al. “Study of heavy-flavor quarks produced in association with top-quark pairs at $\sqrt{s} = 7\mathrm{TeV}$ using the ATLAS detector”. In: *Phys. Rev. D* 89 (2014), p. 072012. DOI: 10.1103/PhysRevD.89.072012. arXiv: 1304.6386 [hep-ex].

[70] Georges Aad et al. “Measurements of fiducial cross-sections for tt production with one or two additional b-jets in pp collisions at $\sqrt{s} = 8\mathrm{TeV}$ using the ATLAS detector”. In: *Eur. Phys. J. C* 76 (2016), p. 11. DOI: 10.1140/epjc/s10052-015-3852-4. arXiv: 1508.06868 [hep-ex].

[71] Morad Aaboud et al. “Measurements of inclusive and differential fiducial cross-sections of tt production with additional heavy-flavour jets in proton-proton collisions at $\sqrt{s} = 13\mathrm{TeV}$ with the ATLAS detector”. In: *JHEP* 04 (2019), p. 046. DOI: 10.1007/JHEP04(2019)046. arXiv: 1811.12113 [hep-ex].

[72] Vardan Khachatryan et al. “Measurement of tt production with additional jet activity, including b quark jets, in the dilepton decay channel using pp collisions at $\sqrt{s} = 8\mathrm{TeV}$”. In: *Eur. Phys. J. C* 76 (2016), p. 379. DOI: 10.1140/epjc/s10052-016-4105-x. arXiv: 1510.03072 [hep-ex].

[73] Albert M Sirunyan et al. “Measurements of tt cross sections in association with b jets and inclusive jets and their ratio using dilepton final states in pp collisions at $\sqrt{s} = 13\mathrm{TeV}$”. In: *Phys. Lett. B* 776 (2018), p. 355. DOI: 10.1016/j.physletb.2017.11.043. arXiv: 1705.10141 [hep-ex].

[74] Albert M Sirunyan et al. “Measurement of the $\mathrm{t\bar{t}b\bar{b}}$ production cross section in the all-jet final state in pp collisions at $\sqrt{s} = 13\mathrm{TeV}$”. In: *Phys. Lett. B* 803 (2020), p. 135285. DOI: 10.1016/j.physletb.2020.135285. arXiv: 1909.05306 [hep-ex].

[75] Albert M Sirunyan et al. “First measurement of the cross section for top quark pair production with additional charm jets using dileptonic final states in pp collisions at $\sqrt{s} = 13\mathrm{TeV}$”. In: *Phys. Lett. B* 820 (2021), p. 136565. DOI: 10.1016/j.physletb.2021.136565. arXiv: 2012.09225 [hep-ex].

[76] Matteo Cacciari, Gavin P. Salam, and Gregory Soyez. “The anti-k_T jet clustering algorithm”. In: *JHEP* 04 (2008), p. 063. DOI: 10.1088/1126-6708/2008/04/063. arXiv: 0802.1189 [hep-ex].

[77] Matteo Cacciari, Gavin P. Salam, and Gregory Soyez. “FastJet user manual”. In: *Eur. Phys. J. C* 72 (2012), p. 1896. DOI: 10.1140/epjc/s10052-012-1896-2. arXiv: 1111.6097 [hep-ph].

[78] Matteo Cacciari and Gavin P. Salam. "Pileup subtraction using jet areas". In: *Phys. Lett. B* 659 (2008), p. 119. DOI: 10.1016/j.physletb.2007.09.077. arXiv: 0707.1378 [hep-ph].

[79] Federico Buccioni et al. "NLO QCD predictions for $ttbb$ production in association with a light jet at the LHC". In: *JHEP* 12 (2019), p. 015. DOI: 10.1007/JHEP12(2019)015. arXiv: 1907.13624 [hep-ph].

[80] CMS Internal Presentation: Stefano Pozzorini. *Heavy flavour backgrounds in $ttH(bb)$*. https://indico.cern.ch/event/827858/contributions/3481144/attachments/1870565/3155726/v2-shower-hxswg2019.pdf. Accessed: 2022-02-15.

[81] *CMS Internal TWiki: Hadron based origin identification of heavy flavour jets at generator level.* https://twiki.cern.ch/twiki/bin/view/CMSPublic/GenHFHadronMatcher. Accessed: 2021-11-25.

[82] Nazar Bartosik, Johannes Hauk, and Achim Geiser. *Identification of the origin of heavy flavour jets at generator level in Monte Carlo simulations at CMS.* https://cms.cern.ch/iCMS/jsp/db_notes/noteInfo.jsp?cmsnoteid=CMS%20AN-2014/093. Accessed: 2021-11-25.

[83] *CMS Internal TWiki: MET Filter Recommendations for Run II.* https://twiki.cern.ch/twiki/bin/viewauth/CMS/MissingETOptionalFiltersRun2. Accessed: 2021-10-21.

[84] CMS Internal Twiki: L1 Prefiring. *Reweighting recipe to emulate Level 1 ECAL and Muon prefiring.* https://twiki.cern.ch/twiki/bin/viewauth/CMS/L1PrefiringWeightRecipe. Accessed: 2021-11-18.

[85] Dmytro Kovalskyi and Jan-Frederik Schulte. *Measurement of prefiring in the L1 muon triggerin Run 2.* https://cms.cern.ch/iCMS/user/noteinfo?cmsnoteid=CMS%20AN-2021/086. Accessed: 2021-11-18.

[86] *CMS Internal TWiki: EGamma ID Recipes Run II.* https://twiki.cern.ch/twiki/bin/view/CMS/EgammaIDRecipesRun2. Accessed: 2021-11-17.

[87] A. M. Sirunyan et al. "Performance of the CMS muon detector and muon reconstruction with proton-proton collisions at $\sqrt{s} = 13$ TeV". In: *JINST* 13 (2018), P06015. DOI: 10.1088/1748-0221/13/06/P06015. arXiv: 1804.04528 [physics.ins-det].

[88] *CMS Internal TWiki: Baseline Muon Selections for Run II.* https://twiki.cern.ch/twiki/bin/view/CMS/SWGuideMuonIdRun2. Accessed: 2021-11-17.

[89] Albert M Sirunyan et al. "Particle-flow reconstruction and global event description with the CMS detector". In: *JINST* 12 (2017), P10003. DOI: 10.1088/1748-0221/12/10/P10003. arXiv: 1706.04965 [physics.ins-det].

[90] E. Bols et al. "Jet flavour classification using DeepJet". In: *JINST* 15.12 (Dec. 2020), P12012–P12012. ISSN: 1748-0221. DOI: 10.1088/1748-0221/15/12/p12012.

[91] *Identification of b quark jets at the CMS Experiment in the LHC Run 2.* Tech. rep. Geneva: CERN, 2016. URL: https://cds.cern.ch/record/2138504.

[92] CMS Internal Presentation: Caroline Collard. *b tagging at CMS.* https://indico.in2p3.fr/event/12859/contributions/11766/attachments/9892/12317/GDRNantes_btag.pdf. Accessed: 2022-10-27.

[93] *CMS Internal TWiki: Heavy flavour tagging for 13 TeV data in 2016preVFP Ultra-Legacy reprocessing and 10_6_X MC.* https://twiki.cern.ch/twiki/bin/viewauth/CMS/BtagRecommendation106XUL16preVFP. Accessed: 2021-11-17.

[94] *CMS Internal TWiki: Heavy flavour tagging for 13 TeV data in 2016postVFP Ultra-Legacy reprocessing and 10_6_X MC.* https://twiki.cern.ch/twiki/bin/viewauth/CMS/BtagRecommendation106XUL16postVFP. Accessed: 2021-11-17.

[95] *CMS Internal TWiki: Heavy flavour tagging for 13 TeV data in 2017 Ultra-Legacy reprocessing and 10_6_X MC.* https://twiki.cern.ch/twiki/bin/viewauth/CMS/BtagRecommendation106XUL17. Accessed: 2021-11-17.

[96] *CMS Internal TWiki: Heavy flavour tagging for 13 TeV data in 2018 Ultra-Legacy reprocessing and 10_6_X MC*. https://twiki.cern.ch/twiki/bin/viewauth/CMS/BtagRecommendation106XUL18. Accessed: 2021-11-17.

[97] *CMS Internal TWiki: Recommendation for Using b-tag Objects in Physics Analyses*. https://twiki.cern.ch/twiki/bin/viewauth/CMS/BtagRecommendation. Accessed: 2021-10-20.

[98] Torbjörn Sjöstrand et al. "An Introduction to PYTHIA 8.2". In: *Comput. Phys. Commun.* 191 (2015), p. 159. DOI: 10.1016/j.cpc.2015.01.024. arXiv: 1410.3012 [hep-ph].

[99] Federico Buccioni et al. "OpenLoops 2". In: *Eur. Phys. J. C* 79.10 (2019), p. 866. DOI: 10.1140/epjc/s10052-019-7306-2. arXiv: 1907.13071 [hep-ph].

[100] Enrico Bothmann et al. "Event generation with Sherpa 2.2". In: *SciPost Physics* 7.3 (Sept. 2019). DOI: 10.21468/scipostphys.7.3.034. URL: https://doi.org/10.21468%5C%2Fscipostphys.7.3.034.

[101] Daniel Reichelt, Peter Richardson, and Andrzej Siodmok. "Improving the simulation of quark and gluon jets with Herwig 7". In: *The European Physical Journal C* 77.12 (Dec. 2017). DOI: 10.1140/epjc/s10052-017-5374-8. URL: https://doi.org/10.1140%5C%2Fepjc%5C%2Fs10052-017-5374-8.

[102] Marketa Jansova. "Search for the supersymmetric partner of the top quark and measurements of cluster properties in the silicon strip tracker of the CMS experiment at Run 2. Recherche du partenaire supersymétrique du quark top et mesure des propriétés des dépôts dans le trajectographe à pistes de silicium de l'expérience CMS au Run 2". Presented 27 Sep 2018. 2018. URL: http://cds.cern.ch/record/2647308.

[103] S. Kullback and R. A. Leibler. "On Information and Sufficiency". In: *The Annals of Mathematical Statistics* 22.1 (1951), pp. 79–86. DOI: 10.1214/aoms/1177729694. URL: https://doi.org/10.1214/aoms/1177729694.

[104] Albert M Sirunyan et al. "Extraction and validation of a new set of CMS PYTHIA8 tunes from underlying-event measurements". In: *Eur. Phys. J. C* 80.1 (2020), p. 4. DOI: 10.1140/epjc/s10052-019-7499-4. arXiv: 1903.12179 [hep-ex].

[105] Sercan et. al. CMS Internal CADI: Sen. *Extraction and validation of a new set of CMS tunes with new color reconnection models in PYTHIA8 from underlying-event measurements*. https://cms.cern.ch/iCMS/user/noteinfo?cmsnoteid=CMS%20AN-2021/086. Paper draft 13, Accessed: 2021-11-19.

[106] Abhisek Datta et al. *Trigger Efficiencies and Scale Factors for the ttH(bb) Measurement in Single Lepton and Dilepton Channels with the Full Run-2 Data Sample*. https://cms.cern.ch/iCMS/jsp/db_notes/noteInfo.jsp?cmsnoteid=CMS%20AN-2019/008. Accessed: 2021-10-20.

[107] Roger J. Barlow and Christine Beeston. "Fitting using finite Monte Carlo samples". In: *Comput. Phys. Commun.* 77 (1993), pp. 219–228. DOI: 10.1016/0010-4655(93)90005-W.

[108] J. S. Conway. *Incorporating Nuisance Parameters in Likelihoods for Multisource Spectra*. 2011. arXiv: 1103.0354 [physics.data-an].

[109] Simone Paoletti. *The CMS Tracker Upgrade for the High Luminosity LHC*. Tech. rep. Geneva: CERN, 2020. DOI: 10.22323/1.364.0138. URL: https://cds.cern.ch/record/2723307.

[110] CMS Collaboration. *The Phase-2 Upgrade of the CMS Data Acquisition and High Level Trigger*. Tech. rep. This is the final version of the document, approved by the LHCC. Geneva: CERN, 2021. URL: http://cds.cern.ch/record/2759072.

[111] Sudhir Malik. *CMS Phase-2 Inner Tracker Upgrade*. Tech. rep. Geneva: CERN, 2021. URL: http://cds.cern.ch/record/2816244.

[112] *Schedule and luminosity forecasts*. https://lhc-commissioning.web.cern.ch/schedule/HL-LHC-plots.htm. Accessed: 2022-10-07.

[113] J (CERN) Chistiansen and M (LBNL) Garcia-Sciveres. *RD Collaboration Proposal: Development of pixel readout integrated circuits for extreme rate and radiation*. Tech. rep. The authors are editors on behalf of the participating institutes. the participating institutes are listed in the proposal. Geneva: CERN, 2013. URL: https://cds.cern.ch/record/1553467.

[114] J Christiansen and M Garcia-Sciveres. *Extension of RD53 for 3 years to finalize pixel chips for the ATLAS and CMS pixel detector upgrades*. Tech. rep. Geneva: CERN, 2021. URL: https://cds.cern.ch/record/2771713.

[115] Conti et al. "Development of a Large Pixel Chip Demonstrator in RD53 for ATLAS and CMS Upgrades". In: *Topical Workshop on Electronics for Particle Physics*. Vol. TWEPP-17. Santa Cruz, United States, Sept. 2017, p. 005. DOI: 10.22323/1.313.0005. URL: https://hal.archives-ouvertes.fr/hal-02410855.

[116] CMS Internal Presentation: Stella Orfanelli. *The Phase 2 upgrade of CMS Inner Tracker*. https://indico.cern.ch/event/863071/contributions/3738839/attachments/2045658/3427296/IT_ACES2020.pdf. Accessed: 2022-10-07.